




Università degli Studi di Padova

Centro Ricerche Fusione

Universidade de Lisboa

Instituto Superior Técnico **(IST)**

Università degli Studi di Napoli Federico II

Ghent University

JOINT RESEARCH DOCTORATE IN FUSION SCIENCE AND ENGINEERING

Cycle XXX

ERASMUS MUNDUS International Doctoral College in Fusion Science and Engineering

Studies and experimental activities to qualify the behaviour of RF power circuits for Negative Ion Sources of Neutral Beam Injectors for ITER and fusion experiments

Coordinator: Prof. Paolo Bettini

Supervisors at Università degli Studi di Padova (Home Institution): Prof. Paolo Bettini

Co-Supervisor at Università degli Studi di Padova (Home Institution): Dr. Elena Gaio

Supervisor at Universiteit Gent: Prof. Kristel Crombé

Co-Supervisor at IPP (Host Institution): Prof. Ursel Fantz

Ph.D. student: Palak Jain

This research has been funded by Erasmus Mundus Fusion Dc.

CONTENTS

List of Figures

List of Tables

Abbreviations

ITER	International Thermonuclear Experimental Reactor
NBI	Neutral Beam Injector
NBTF	Neutral Beam Test Facility
PRIMA	Padova Research on ITER Megavolt Accelerator
MITICA	Megavolt ITER Injector and Concept Advancement
SPIDER	Source for the Production of Ions of Deuterium Extracted from RF plasma
IC	Inductively Coupled
RF	Radio Frequency
ELISE	Extraction from a Large Ion Source Experiment
NIO1	Negative Ion Optimization 1
HVRFTF	High Voltage Radio-Frequency Test Facility
IPP	Max-Planck-Institut für Plasmaphysik
GDP	Gross Domestic Product
ICF	Inertial Confinement
NIF	National Ignition Facility
LMJ	Laser Megajoule
RFP	Reverse Field Pinch
DEMO	DEMOnstration Power Plant
PFC	Plasma Facing Component
ECRH	Electron Cyclotron Resonance Heating
ICRH	Ion Cyclotron Resonance Heating
LH	Lower Hybrid Heating
HNB	Heating Neutral Beam Injector
DNB	Diagnostic Neutral Beam
RID	Residual Ion Dump
PG	Plasma Grid
BS	Beam Source
EMS	Electromagnetic Shield
DC	Driver Case
FS	Faraday Screen
ISEPS	Ion Source and Extraction Power Supply
STRIKE	Short-Time Retractable Instrumented Kalorimeter Experiment
HVD	High Voltage Deck

LHS	Left Hand Side
RHS	Right Hand Side
TE	Transverse Electric
ICP	Inductively Coupled Plasmas
PER	Plasma Equivalent Resistance
PTE	Power Transfer Efficiency
DUT	Device Under Test
EM	Electro-Magnetic
SE	Shielding Effectiveness

ABSTRACT

The International Thermonuclear Experimental reactor (ITER), the world's largest experimental facility in the realm of nuclear fusion for energy production, requires two Neutral Beam Injectors (NBI) rated for the total power of 33 MW for plasma heating and current drive. The ITER NBI includes an ion source which can produce 40 A of D^- ions beams for 3600 s, accelerated at the energy of 1 MeV. The requirements for the ITER NBI are quite demanding and have never been achieved before all together in a single device. This specifically called for a development of the ITER Neutral Beam Test Facility (NBTF) called PRIMA (Padova Research on ITER Megavolt Accelerator) to carry out an international R&D program for the achievement of the ITER NBI requirements and the optimization of the operation in advance of the future use in ITER. The facility will host two experiments, SPIDER (Source for the Production of Ions of Deuterium Extracted from RF plasma), the full-size prototype of ITER RF ion source, and MITICA (Megavolt ITER Injector and Concept Advancement), the full-scale prototype of the ITER heating NBI. The NBTF in Padova, Italy, is ready, MITICA is currently under construction and SPIDER has been in operation since beginning of June 2018.

The NBI ion source was initially based on filament type arc source, while for ITER the inductively coupled (IC) radio frequency (RF) ion source have been finally chosen in 2007. This is because RF sources present several advantages with respect to arc solutions; they have fewer parts and require less maintenance. In these ion sources, radio frequency plasma is generated at the frequency of 1 MHz and is characterized by high RF power density and low operational pressure (around 0.3 Pa).

In the last decades, IC ion sources have been developed, studied and experimented at the Max-Planck-Institut für Plasmaphysik (IPP) in Garching, Germany. The most recent one is ELISE (Extraction from a Large Ion Source Experiment), which is able to operate with both Hydrogen and Deuterium gas species and has half the size of ITER NBI source.

Other accompanying activities have been recently launched at Consorzio RFX, Padova, Italy within the ITER NBI work program; one of them is a relatively small ion source called NIO1 (Negative Ion Optimization 1) working at 2 MHz, developed in order to gain experience on ion source operation and to study specific physics and engineering topics on a more flexible and accessible device than the SPIDER and MITICA. In addition, a small experimental test facility called HVRFTF (High Voltage Radio Frequency Test Facility) based on a high voltage resonance circuit that feeds a couple of electrodes in vacuum has been started at Consorzio

RFX in 2014 to address and study the voltage holding capability of the RF components in the ion source at 1 MHz.

The research endeavor during the three years of my PhD was carried out in the frame of the RF R&D task of the NBTF work-program at Consorzio RFX and during the mobility periods at the IPP.

I have had the opportunity to work on two main lines: the first was dedicated towards the study of the RF power transfer efficiency of IC RF ion sources and the development of suitable models that will permit to explore possible improvements (in the future). In fact, the higher the efficiency, the lower can be the feeding power to the ion source and this may lead to a lower requirement both for cooling and for electrical insulation of the RF circuit components installed on the source. I have studied and analyzed several plasma heating mechanisms (like ohmic and stochastic heating in particular) and I have developed an electrical model which is responsible for describing the power transfer to the plasma. The first approach was based on a transformer model, and then a multi current filament model has been developed. This model is capable to account for the currents in the passive metallic structure within the driver region of the ion source and with this; it is able to overcome the main limitation of the transformer model. Furthermore, I have integrated all the models to develop a novel methodology to evaluate the efficiency of the RF power transfer to the hydrogen plasma in a cylindrical source. Then, I have implemented the methodology in a MATLAB® code and applied it to the driver of ELISE and NIO1 ion sources showing the results in terms of plasma equivalent resistance and power transfer efficiency obtained as a function of applied frequency and plasma parameters (electron density and gas pressure).

The second part of my work was directed towards the design, construction and set-up of the HVRFTF. I gave an important contribution in terms of the electrical characterization of the RF resonance circuit components (mainly the two solenoid coupled inductor), thermal analysis of the electrodes placed inside the vacuum vessel, analyses and design of an efficient shielding from the electro-magnetic radiations foreseen during the operation of the test facility. All this contributed towards the success in the set-up of the test facility which is now in operation.

The thesis is structured as follows:

Chapter 1 and 2 are introductory chapters on the present energy scenario in the world, the role of the thermo-nuclear fusion and the main fusion experimental device called ITER. The requirement of additional heating systems in ITER along with the description of Neutral beam injection (NBI) system and relevant ion sources (SPIDER, ELISE and NIO1) are presented in these chapters.

Then, the thesis is divided into two main parts:

Part 1 – From Chapter 3 to Chapter 6 - describes my work on the power transfer efficiency to the plasma of the inductively coupled radio frequency ion sources.

Part 2 – From Chapter 7 to chapter 10 - summarizes first the aim of the HVRFTF then reports my contribution to its design and set-up.

Lastly, the overall conclusion highlighting the most significant results obtained from the research described in both the parts of the thesis is discussed and a further possible research activity is highlighted for the future work.

Throughout the journey of the PhD, I have had the opportunity to grow and acquire different research competences ranging from conceptual studies, modeling activities, practice on several numerical codes and also experimental work, in an international context.

SOMMARIO

Abstract in Italian

Il reattore sperimentale ITER, il più grande esperimento nel settore della produzione di energia da fusione nucleare, richiede di essere equipaggiato con due sistemi d'iniezione di fasci di particelle neutre (chiamato ITER NBI nel seguito), caratterizzati da una potenza complessiva di 33 MW, per contribuire al riscaldamento del plasma e controllo della relativa corrente. ITER NBI comprende una sorgente di ioni negativi che può produrre un fascio di ioni di deuterio accelerati all'energia di 1 MeV, per una durata di 3600 s. L'insieme dei requisiti richiesti ad ITER NBI non sono mai stati raggiunti contemporaneamente nello stesso esperimento. Ciò ha motivato lo sviluppo di un'infrastruttura sperimentale: "the ITER Neutral Beam Test Facility (NBTF)", chiamata anche PRIMA (Padova Research on ITER Megavolt Accelerator), che ha lo scopo di portare avanti un progetto di ricerca internazionale finalizzato alla dimostrazione della possibilità di raggiungere i requisiti specificati per ITER NBI e alla crescita di conoscenza e competenza nella sperimentazione, prima dell'uso futuro in ITER NBTF ospiterà due esperimenti: SPIDER (Source for the Production of Ions of Deuterium Extracted from an RF plasma), il prototipo a piena scala della sorgente a ioni negativi di ITER NBI, e MITICA (Megavolt ITER Injector and Concept Advancement), il prototipo a piena scala dell'intero ITER NBI. NBTF è stata completata ed ha sede a Padova, in Italia; MITICA è attualmente in costruzione e SPIDER è in operazione dall'inizio di giugno 2018.

La sorgente di ioni scelta inizialmente per ITER NBI era del tipo ad arco, ma dal 2007 il progetto dell'NBI è stato sviluppato considerando sorgenti di ioni prodotti in un plasma generato secondo il principio dell'accoppiamento induttivo a radiofrequenza (RF). Queste sorgenti presentano diversi vantaggi rispetto alle sorgenti ad arco: hanno un numero minore di componenti e richiedono minor manutenzione. Le sorgenti RF di ITER NBI operano alla frequenza di 1 MHz, sono caratterizzate da una densità di potenza piuttosto elevata e basso valore di pressione del gas all'interno della camera (0,3 Pa circa).

Queste tipologie di sorgenti ioniche sono state studiate e sviluppate negli ultimi decenni presso il Max-Planck-Institut für Plasmaphysik (IPP), dove sono stati realizzati e testati diversi dispositivi sperimentali. Il più recente di essi, chiamato ELISE (Extraction from a Large Ion Source Experiment), è caratterizzato da dimensioni pari a metà di quelle previste per la sorgente ionica di ITER NBI.

Altre attività sperimentali di supporto alla ricerca e sviluppo in questo settore sono state avviate presso il Consorzio RFX; una di queste consiste nella realizzazione di una sorgente a

ioni negativi relativamente piccola, chiamata NIO1 (Negative Ion Optimization 1), che lavora alla frequenza di 2 MHz, sviluppata per fare esperienza sul funzionamento di sorgenti di ioni negativi e studiare problematiche specifiche di interesse per ITER NBI in un apparato sperimentale molto più flessibile ed accessibile rispetto a SPIDER e MITICA. Inoltre, la realizzazione di un ulteriore dispositivo sperimentale, chiamato HVRFTF (High Voltage Radio Frequency Test Facility), basato su un circuito risonante in alta tensione che polarizza una coppia di elettrodi in vuoto, è stata avviata presso il Consorzio RFX nel 2014 per studiare specifiche problematiche relative alla tenuta della tensione in vuoto di componenti del circuito a radiofrequenza della sorgente di ioni a 1MHz.

Il lavoro di ricerca durante i tre anni del mio PhD è stato portato avanti nell'ambito del programma di ricerca e sviluppo sulle sorgenti ioniche a radiofrequenza presso il Consorzio RFX, e durante i periodi di "mobility" presso il laboratorio IPP.

Ho avuto l'opportunità di approfondire due tematiche principali: la prima era indirizzata allo studio dell'efficienza del trasferimento di potenza al plasma delle sorgenti di ioni tipo IC RF e allo sviluppo di modelli allo scopo di esplorare in futuro possibili miglioramenti. Infatti, maggiore è l'efficienza, minore è la potenza richiesta al generatore e ciò comporta requisiti meno severi per il sistema di raffreddamento e sollecitazioni inferiori in termini di tensione elettrica applicata. Ho studiato i diversi meccanismi di riscaldamento del plasma (come il riscaldamento ohmico ed in particolare il riscaldamento stocastico) ed ho studiato come descrivere il trasferimento di potenza ad un plasma di idrogeno. Il primo modello sviluppato si basa sullo schema del trasformatore; successivamente ho contribuito significativamente a sviluppare un modello "a multi filamenti" di corrente. Questo modello riproduce le correnti indotte nelle strutture passive presenti nella regione del driver della sorgente di ioni ed è in grado di superare le limitazioni del modello del trasformatore. Ho integrato tutti i modelli per sviluppare una nuova metodologia per la stima dell'efficienza del trasferimento di potenza nei plasmi di idrogeno generati in sorgenti cilindriche. Ho poi implementato la metodologia in MATLAB®, applicandola ai casi delle sorgenti ioniche di ELISE e NIO1, presentando i risultati ottenuti in termini di stima della resistenza equivalente di plasma e di efficienza del trasferimento di potenza come funzione della frequenza applicata e dei parametri di plasma (densità elettronica e pressione del gas).

La seconda parte del mio lavoro si è svolta nell'ambito dello sviluppo della HVRFTF. Ho dato importanti contributi che sono consistiti nella caratterizzazione dei componenti del circuito risonante a radiofrequenza (in particolare dell'induttore composto da due solenoidi accoppiati magneticamente), nelle analisi termiche degli elettrodi posti nella camera da vuoto, nelle analisi e progetto di un sistema di schermatura efficace delle radiazioni

elettromagnetiche generate dall'operazione dell'esperimento. Tutto ciò ha contribuito al positivo completamento dell'apparato sperimentale, attualmente in funzione.

La tesi è strutturata come segue:

I capitoli 1 e 2 sono di tipo introduttivo sull'attuale scenario energetico, sul ruolo della fusione termonucleare controllata e del principale esperimento internazionale ITER. In questi capitoli inoltre sono presentati i requisiti del sistema di riscaldamento del plasma di ITER, la descrizione del sistema di iniezione di neutri (NBI) e delle sorgenti ioniche di interesse (SPIDER, ELISE e NIO1).

Poi, la tesi è suddivisa in due parti:

Parte 1- dal capitolo 3 al capitolo 6- che tratta del lavoro che ho svolto sul problema dell'efficienza del trasferimento induttivo di potenza al plasma nelle sorgenti ioniche.

Parte 2 - dal capitolo 7 al capitolo 10- che riassume lo scopo della "HVRFTF" e descrive il mio contributo al suo progetto e realizzazione.

Infine, nelle conclusioni ho discusso i più significativi risultati ottenuti dal lavoro di ricerca presentato nelle Parti 1 e 2 di questa tesi evidenziando i possibili sviluppi futuri.

Durante il percorso del dottorato di ricerca, ho avuto l'opportunità di crescere e acquisire diverse competenze di ricerca che vanno dagli studi concettuali, alle attività di modellizzazione, alla pratica su diversi codici numerici e anche al lavoro sperimentale, in un contesto internazionale.

SAMENVATTING

Abstract in Dutch

De Internationale Thermonucleaire Experimentele Reactor (ITER), de grootste experimentele machine ter wereld voor de productie van energie door kernfusie, zal twee Neutral Beam Injectors (NBI) nodig hebben met een totaal vermogen van 33 MW voor de verhitting van het plasma en het genereren van een plasmastroom. Het ITER NBI systeem moet een ionenbron bevatten die D^- ionen kan produceren aan 40 A gedurende 3600 s en die de geladen deeltjes kan versnellen tot een energie van 1 MeV. Deze vereisten zijn erg ambitieus en werden nooit eerder bereikt op een bestaande machine. Daarom is het nodig om een specifieke testopstelling te bouwen. Deze Neutral Beam Test Facility (NBTF) is onder constructie in Padua, Italië. De installatie kreeg de naam PRIMA en staat voor Padova Research on ITER Megavolt Accelerator. De volledige opstelling zal uit twee experimenten bestaan, SPIDER (Source for the Production of Ions of Deuterium Extracted from an RF plasma), een prototype voor de ITER RF ionenbron, en MITICA (Megavolt ITER Injector and Concept Advancement), een prototype voor het ITER NBI verhittingssysteem. Beide worden gebouwd op ware grootte. Het onderzoeksinstituut in Padua wil mede dankzij NBTF een internationaal R&D programma uitbouwen. Het voornaamste doel is om de hoge eisen die aan het ITER NBI systeem zijn gesteld, te kunnen bereiken en de operatie ervan te optimaliseren, vooraleer het verhittingssysteem in ITER zal worden ingebouwd. NBTF is al bijna volledig klaar, SPIDER is zeer recent afgewerkt, het is operationeel sinds begin juni 2018 en MITICA is nog in aanbouw.

De NBI ionenbron was oorspronkelijk gebaseerd op een filament type boogontlading, maar voor de ITER NBI werd in 2007 toch geopteerd voor een inductief gekoppelde (Inductively Coupled, IC) radio frequente (RF) aangedreven ionenbron. Er zijn immers vele voordelen aan dit IC type verbonden in vergelijking met de meer traditionele boogontladingen; er zijn aanzienlijk minder onderdelen en ze vragen minder onderhoud. In deze IC RF ionenbronnen worden radio frequente plasma's gegenereerd aan een frequentie van 1 MHz. De plasma's zijn gekarakteriseerd door hoge dichtheden in het RF vermogen en dat bij een lage druk (rond 0.3 Pa).

Gedurende de voorbije tientallen jaren werden de IC RF ionenbronnen reeds ontwikkeld, bestudeerd en getest aan het Max-Planck-Institut für Plasmaphysik (IPP) in Garching, Duitsland. De meest recente opstelling daar is ELISE (Extraction from a Large Ion Source Experiment), die half zo groot is als de NBI bron voor ITER.

Andere nevenactiviteiten in deze context werden recent gestart aan het Consorzio RFX als deel van het ITER NBI werkprogramma; één ervan is de relatief kleine ionenbron NIO1 genaamd (Negative Ion Optimization 1) die werkt bij 2 MHz, en werd ontwikkeld om ervaring te krijgen met de operatie van een dergelijke bron. Bovendien laat deze machine zeer specifieke studies toe, zowel van meer fysisch georiënteerde onderwerpen als van ingenieurstoepassingen. Dit is het voordeel van een kleinere en meer flexibele opstelling dan SPIDER en MITICA. Daarnaast werd in 2014 eveneens een kleine experimentele testopstelling, HVRFTF (High Voltage Radio Frequency Test Facility) gebouwd. HVRFTF is gebaseerd op een resonant circuit dat een aantal elektrodes in vacuüm voedt. De bedoeling hiervan is om de hoge voltages te testen in de RF componenten van de ionenbron.

Mijn drie jaar durende doctoraatsonderzoek werd uitgevoerd in het kader van de R&D taak van het NBTF werkprogramma van het Consorzio RFX en werd gecombineerd met verblijven aan het IPP in Garching.

Ik had de kans om te werken op twee belangrijke onderzoekslijnen. De eerste was de studie van de efficiëntie van de overdracht van het RF vermogen bij IC RF ionenbronnen en het ontwikkelen van geschikte modellen die zullen toelaten om (in de toekomst) verbeteringen aan te brengen. Immers, hoe hoger de efficiëntie, hoe lager het beginvermogen mag zijn van de ionenbron. Dit vermindert de vereisten voor de koeling en de elektrische isolatie van de RF componenten in het circuit. Ik heb verschillende effectieve plasma verhittingsmechanismes (zoals de Ohmse verhitting en de stochastische verhitting) bestudeerd in de IC RF bron. Ik heb op die manier aanzienlijk kunnen bijgedragen tot de ontwikkeling van een nieuwe methode om de efficiëntie van de RF vermogensoverdracht te evalueren in waterstof plasma's. Daarnaast, heb ik de methode in MATLAB® geïmplementeerd en toegepast op andere bestaande ionenbronnen, ELISE en de NIO1. Op die manier konden resultaten worden getoond met betrekking tot equivalente plasma weerstand en vermogensoverdracht, die werden verkregen in plasma's met uiteenlopende parameters.

Het tweede deel van mijn werk was geconcentreerd op het design, de constructie en de installatie van HVRFTF. Ik heb een belangrijke bijdrage geleverd tot het elektrisch karakteriseren van de componenten in het RF resonant circuit (in het bijzonder van de twee solenoïdaal gekoppelde inductoren). Daarnaast heb ik ook gezorgd voor de thermische analyse van de elektrodes die in het vacuüm vat zullen worden geïnstalleerd en voor de analyse en het design van een effectieve afscherming voor de elektromagnetische straling, zoals die wordt verwacht tijdens de operatie van de testopstelling. Dit alles heeft bijgedragen tot een succesvolle installatie van HVRFTF, die ondertussen volledig operationeel is.

De structuur van de thesis is als volgt:

De hoofdstukken 1 en 2 zijn inleidende hoofdstukken over het huidige energie scenario in de wereld, en de rol van thermonucleaire fusie. De belangrijkste experimentele fusiemachine, ITER, en zijn NBI systeem en relevante ionenbronnen (SPIDER, ELISE en NIO1) worden toegelicht.

Daarna is de thesis in twee grote delen verdeeld:

Het eerste deel - Van hoofdstuk 3 tot 6, beschrijft mijn werk op het gebied van een efficiënte overdracht van het vermogen naar het plasma bij inductief gekoppelde radio frequente ionenbronnen.

Het tweede deel - Van hoofdstuk 7 tot 10, vat eerst de doelstellingen van de HVRFTF opstelling samen. Vervolgens worden mijn bijdragen beschreven tot het design en de installatie ervan.

Tot slot worden de belangrijkste resultaten uit de twee delen samengevat en worden mogelijke pistes voor verder onderzoek gesuggereerd.

Doorheen mijn doctoraatstraject, heb ik de kans gehad om te groeien en verschillende onderzoek competenties aan te leren, gaande van conceptuele studies, modellering en ervaring met verschillende numerieke codes, tot experimentele activiteiten, dit alles in een internationale context.

ACKNOWLEDGEMENTS

Firstly, I would like to thank God without whom it would have been impossible to achieve this milestone. It is my pleasure to acknowledge the roles of several individuals who were instrumental for completion of my PhD research.

I wish to express my sincere gratitude to my supervisor ***Dr. Elena Gaio*** *for her encouragement and enormous support to pursue this project. I appreciate all her contributions of time and ideas to make my Ph.D. experience productive and stimulating.*

I would like to especially acknowledge the inputs from ***Dr. Mauro Recchia*** *who contributed towards many insightful discussions that helped to shape this project. He was always willing to help resolve the most difficult modelling issues and his helpful comments and careful advice has greatly assisted me in writing the thesis.*

I would like to thank ***Dr. Alberto Maistrello, Dr. Pierluigi Veltri*** *and* ***Dr. Marco Cavenago*** *for their useful ideas and support during my work at Consorzio RFX.*

I would also like to thank ***Prof. Paolo Bettini*** *for providing necessary facilities and taking care of the issues related with Erasmus Mundus Fusion Dc program.*

I am grateful to ***Dr. Ursel Fantz*** *and* ***Dr. Werner Kraus*** *for their valuable contribution towards this research and my general experience during mobility period at IPP.*

I thank ***Prof Kristel Crombé*** *for providing her support at University of Ghent.*

A special acknowledgement goes to my office/lab mates of all these years for teaching me Italian and for all their support.

I pay my heartiest thanks to my family and friends for their fruitful guidance, tremendous support and timely help at every stage of my work. Their patience, encouragement, and enthusiasm have made this endeavour possible. This work would not have been successful without the moral and emotional support from ***Dr. Mubashir Saleem****, I am extremely grateful for his immense encouragement. Lastly, I would like to acknowledge the financial support received from Erasmus Mundus Fusion Dc.*

Palak Jain
Padova, Italy
April 2018

Chapter 1.

Overview on energy scenario and thermonuclear fusion

1.1 Present energy scenario in the world

The life of the modern human depends on the energy. As the quality of the life goes higher the need for energy increases. For the world's economic development and stability it is necessary to have secure, reliable and affordable energy resources. The major challenges faced by the energy decision makers of the today's world consists of the growing energy need of the developing world, the erosion of the energy security and a continuous risk of disruptive climate changes. To meet these challenges, it is required to make better use of the existing technologies and to adopt new and innovative energy technologies.

According to the report of *BP energy Outlook 2013* [1], the two main factors influencing the growing energy demands are the population and the income growth, see Figure 1 . It is projected that the world population will reach 8.3 billion by 2030 while the world income (represented in terms of gross domestic product (GDP)) in 2030 is expected to roughly double the 2011 level. From 2011 to 2030 the primary energy demand is predicted to grow by 1.6 % per annum.

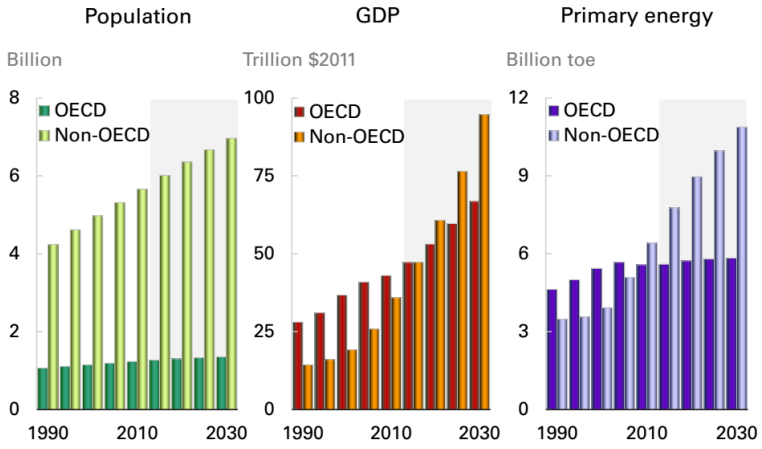

Figure 1: World's population, income and primary energy estimation [1][1].

[1] OECD - On 14 December 1960, 20 countries originally signed the Convention on the Organization for Economic Co-operation and Development. Since then, 15 countries have become members of the Organization. The list of countries can be found on http://www.oecd.org

The overall demand for energy looks to expand continuously. However, the present scenario of the world is not on the intended path for a sustainable energy. In the past few centuries fossil fuels (such as coal, oil, natural gas, petroleum, etc.) have been the main resource of energy for the world. The present available fossil fuel wealth was created millions of years ago on earth by various geological evolutions (i.e., due to the changes in the earth over the period of time). The fossil fuel may also be needed by our grandchildren for sundry reasons (other than burning). It is predicted that in about 300 years of modern civilization these fossil fuels will be depleted completely from earth. There are continuous concerns about the fossil fuel prices (in particular oil) based on the balance of its supply and demand. The continuous use of the fossil fuels in past centuries has led to the serious global warming of the planet earth. CO_2 emissions have increased by more than 20% over the last decade. The oil demand and CO_2 emission will continue to increase rapidly over the next 25 years. Despite its needs the mentioned issues clearly indicate the restricted use of the fossil fuel for energy production in the future. This suggests the use of the fuel mix solution for the energy production. As suggested in the report [2] provided by the *BP energy Outlook 2017*, the gradual transition in the fuel mix continues, see Figure 2. Even though, oil, gas and coal remain the dominant sources of energy powering the world economy, the renewables, together with nuclear and hydroelectric power is expected to account for half of the growth in energy supplies over the next 20 years.

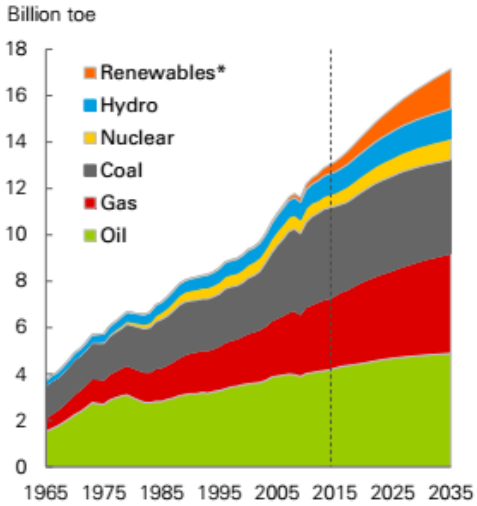

Figure 2: Primary energy consumption by fuel in billion toe (tonne of oil equivalent), taken from [2].

We may be able to somehow satisfy the energy needs in the short term based on the available fossil fuels, but will definitely need a remedy for the long term energy needs and for the limitation of global warming of the planet. For this purposes, the nuclear energy is a very promising candidate at present.

1.2 Nuclear energy

The present day source of nuclear energy is based on the concept of fission reaction. It plays an important supportive role (or even dominant role in countries such as France) in supplying the present demands of electric energy required by the world. In few hundred years, the naturally fissile materials such as ^{235}U will get exhausted and then one has to master the use of the other fissile materials like ^{239}Pu and ^{233}U, which can be bred from fissile materials like ^{238}U and ^{232}Th. With this, there is a possibility that fission can supply the world with the energy for several thousand years, however; this source of energy has its own issues regarding the safety, radioactive waste disposal and proliferation. This has prevented free access and public acceptance to nuclear technologies. Nonetheless, we must look at all the advanced nuclear technologies. Fusion is one of such option.

There are energy models which suggest that fusion power is likely to provide a viable solution to the long term sustainable energy needs of the world. In the entire life cycle of the fusion reactor, the amount of CO_2 emission can be up to a factor of 45 times less than that of coal based reactor of the same capacity, see Figure 3.

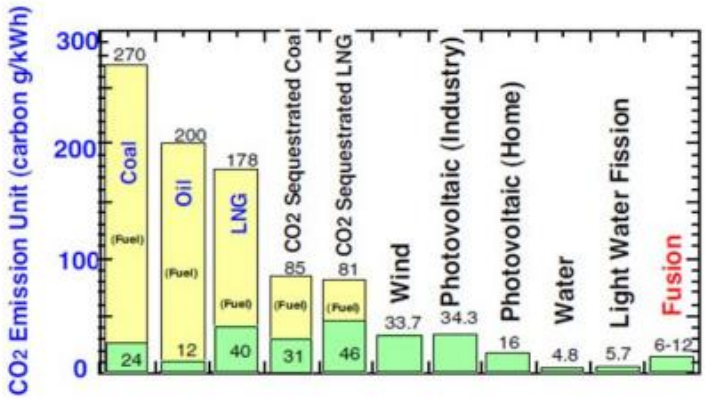

Figure 3: Emission level of CO_2 for different fuel power reactors in their entire life cycle [3]. Here CO_2 emission units for fossil power plants are divided into fuel-oriented emission (represented in yellow) and emission due to other materials (represented in green).

As compared to the renewable source of the energy the fusion reactors are energy dense and can therefore be used for satisfying the needs of urban industrial complexes. In contrast to the fission based nuclear power plants, the fusion power plant have the advantage of inherent operational safety and reduced long lived radioactive emission. The biological hazard potential of fission plants is several orders of magnitude higher than that predicted for fusion reactors, see Figure 4.

The common radioactive waste materials produced in the fission reactors are ^{131}I, ^{90}Sr or ^{137}Cs. These are highly toxic and hazardous and are long lived radioactive isotopes. On the

other hand, tritium which is the main radioactive fuel used in fusion reactor, can be easily discharged (with respect to other elements) from our bodies through metabolism [4]. Tritium is generally only considered to be potentially hazardous when it is inside the body [5]. Tritium can enter the body by inhalation, skin absorption and, mostly commonly, ingestion of tritiated water. For the most part, tritium does not accumulate in any one part of the body, nor does it tend to reside within the body for long periods. Instead, tritium predominantly behaves just like ordinary water in the body, becoming distributed uniformly throughout the body's water and excreted through the same pathways as water, primarily in the form of urine [5].

A small amount of all tritium that enters the body can become bound to organic compounds. Organically bound tritium atoms do not behave like water, can remain in the body for longer periods, and can accumulate in certain parts of the body; however, the effects of organically bound tritium are generally not significant compared to the predominant form of tritium occurring as water in the body. It is also important to note that tritium is hazardous due to its radioactivity [5]. The beta radiation emitted from tritium is weak and can be easily absorbed by a thin sheet of paper.

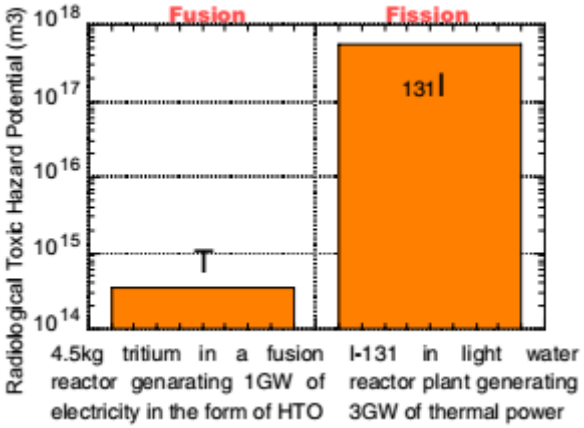

Figure 4: Comparison of radiological toxic hazard potential between tritium and iodine-131 which are typical radioactive nuclides contained in a fusion and a light water fission reactor [3].

The main potential concern of radioactivity in fusion reactor will be from neutron activated reactor components. Care has to be taken to carefully design the fusion reactors with low activity materials so as to require the containment of less than one hundred years after decommissioning of the reactors. Thus this will likely lead to much more social acceptance of the fusion power when it becomes commercial. Furthermore, the resources used to generate the fusion power are virtually inexhaustible and easily accessible to the entire world population.

1.2.1 What is Fusion?

The most common and visible example of fusion energy around us is provided by stars such as the Sun, which have been producing energy for billions of years. In a fusion reaction, light elements fuse together to form heavier elements. The resulting heavier elements have slightly less mass as compared to the fusing elements and this mass difference leads to the release of energy, according to Einstein relationship $E = mc^2$. Energy in the form of the kinetic energies of the product nuclei may be trapped and used for electricity production.

There is no doubt that thermonuclear fusion works and produces lots of energy because uncontrolled thermonuclear explosions using unconfined deuterium and tritium plasma has already been achieved on Earth. Since it is impossible to produce astronomical masses like sun on the surface of Earth, the principle issue faced by the scientist of today's world is to achieve fusion in a controlled manner in a confined plasma, which can then be used for several useful applications like electricity production.

In order to achieve fusion processes on earth, the most feasible reaction involves two hydrogen isotopes, namely deuterium and tritium (see, equation (1)). There are other possible reactions as well but reaction given in equation (1) is chosen because of its larger fusion cross section σ, at lower temperatures, as compared to other reactions (see Figure 5).

$$D + T \rightarrow He\ (3.5\ MeV) + n\ (14.1\ MeV) \quad (1)$$

$$D + D \rightarrow He\ (0.82\ MeV) + n\ (2.45\ MeV) \quad (2)$$

$$D + D \rightarrow T\ (1.01\ MeV) + H\ (3.02\ MeV) \quad (3)$$

$$D + He \rightarrow He\ (3.6\ MeV) + H\ (14.7\ MeV) \quad (4)$$

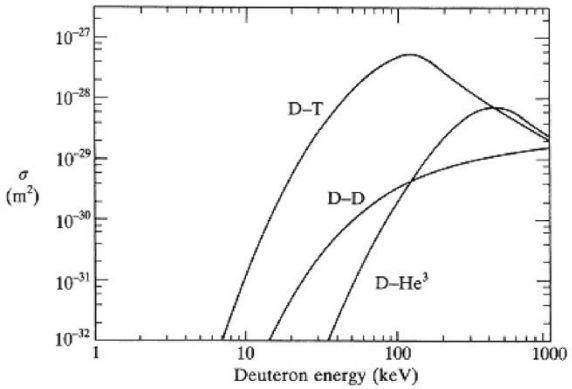

Figure 5: Fusion cross-sections for the D-T, D-D and D-^{3}He (taken from [6]). The D-D curve is the sum of the cross sections of the two D-D reaction listed in equation (2) and (3).

From Figure 5, we see that the D-T curve has a maximum around the particle energy of $\sim 100\ keV$, nevertheless the mean temperature needed to have a sufficient number of reactions in a fusion reactor is greater than $10\ keV$ [4]. Above this temperature there are

sufficient amount of energetic ions populating the high energy tail of the particle velocity distribution which can reach fusion reaction. At this temperature the atoms are ionized. The state of this hot ionized gas is called "plasma". Based on the temperature (T), density (n) and energy confinement time (τ_E), Lawson gave a condition which is needed to achieve ignition, i.e. self-sustaining burning plasma heated without any external system. The confinement time τ_E measures the rate at which the system loses its energy to the environment. The Lawson criteria is given as

$$nT\tau_E > 3 \times 10^{21} \frac{keVs}{m^3} \tag{5}$$

Figure 6, shows the ignition curve, as a function of the triple product parameters. Deuterium is easily available in nature and is a stable isotope of hydrogen whereas tritium is a radioactive isotope of hydrogen with a half-life of about 12 years. Therefore, it does not occur in nature and it has to be produced, the challenge is to produce tritium directly inside the reactor. One way to breed tritium is to use the neutrons produced in the fusion reaction together with lithium, see the following equations

$$^{6}Li + {}^{1}n \rightarrow T + {}^{4}He + 4.8MeV \tag{6}$$

$$^{7}Li + {}^{1}n \rightarrow T + {}^{4}He + n - 2.5MeV \tag{7}$$

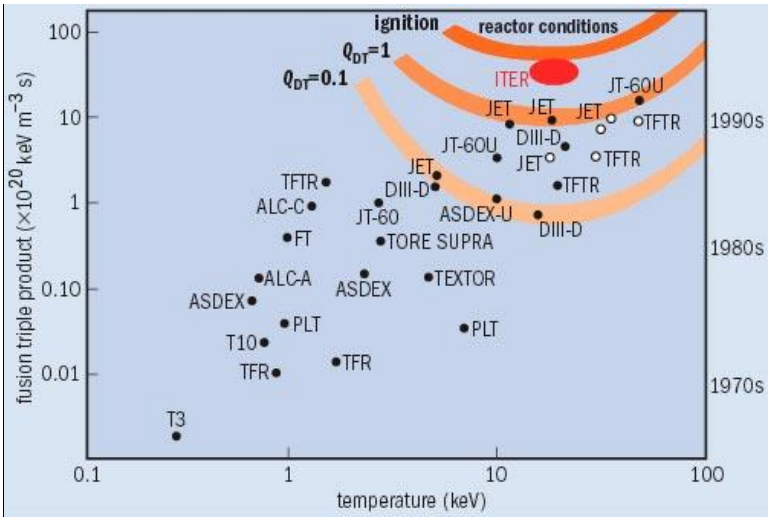

Figure 6: The triple product for a range of experiments for D-T fuel [7].

1.2.2 Road to fusion

In order to achieve sustainable fusion reaction, plasma of the fusion reactants of sufficiently high temperature and density has to be created. This plasma should then be confined for a sufficiently long time away from the surrounding walls, in order to minimize the plasma losses. There are two main approaches for achieving this:

1. Inertial confinement
2. Magnetic confinement

In the inertial confinement (ICF) approach, the thermonuclear fusion is achieved through the micro-explosion of the reactant targets induced by high power laser or particle beams at high repetition rate [8]. The two largest ICF experiments present in the world are the National Ignition Facility (NIF) at Lawrence Livermore National Laboratory in the USA, and the Laser Megajoule (LMJ) facility in France.

The most developed of the two approaches is the magnetic confinement and it is presently the most promising path in achieving the future fusion reactors. The ITER device presently under construction at Cadarache in France will be the first fusion reactor producing 500 MW of fusion power for an input power of 50 MW.

1.3 Thermonuclear fusion by magnetic confinement

In this approach, the charged particles in the plasma are trapped away from its container walls because of the specifically designed magnetic field configuration called a magnetic bottle. This configuration relies on the fact that the motion of a charged particle is strictly restrained along the magnetic lines of force. There are various magnetic configuration concepts developed so far: such as tokamak, Reverse Field Pinch (RFP) and stellarator. The three configurations are shown in Figure 7 and Figure 8. Both RFP [9] and stellarator [10] are not considered in this thesis and only the tokamak configuration is mentioned.

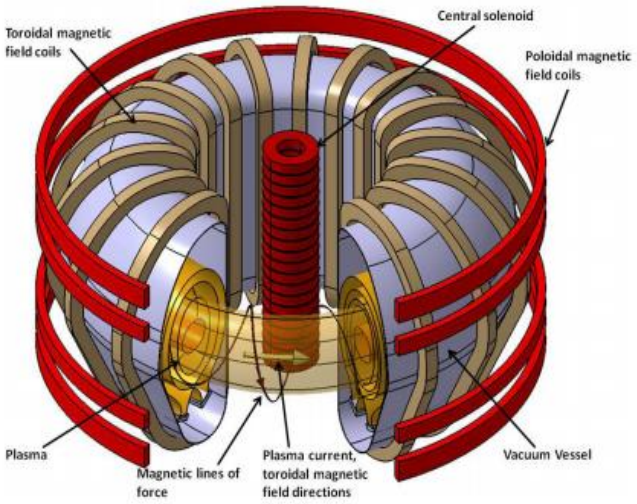

Figure 7: Schematic of a tokamak.

The most developed concept for trapping the plasma particles along the magnetic field lines is based on the tokamak concept. The tokamak is a torus or a doughnut shaped device where the plasma is formed inside a vacuum vessel and confined by the magnetic field. There

are two types of magnetic field acting on the plasma in a tokamak – toroidal and poloidal magnetic field. Toroidal magnetic field is formed by turning a solenoidal set of ring-like coils, around the torus. The poloidal magnetic field is formed by passing a toroidal current in the plasma itself and also with help of poloidal magnetic field coils. The resultants of the toroidal and poloidal magnetic field lines spiral infinitely around the torus (see, Figure 9) in nested toroidal surfaces characterised by constant magnetic flux and pressure ("flux surfaces").

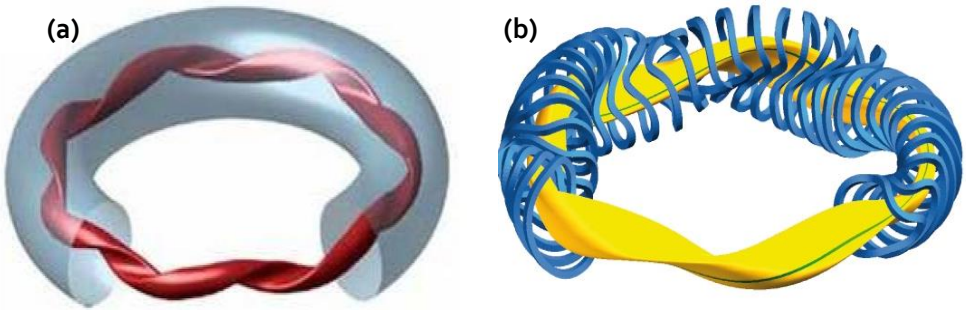

Figure 8: (a) Reverse field pinch and (b) Stellarator.

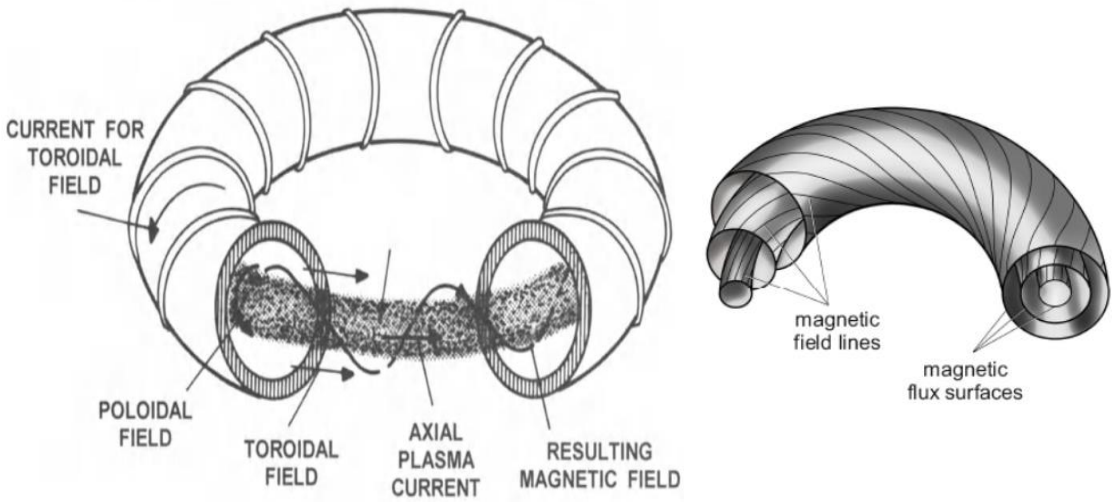

Figure 9: Schematic illustration showing magnetic field configuration of a tokamak [11].

The pressure increases perpendicularly to the flux surfaces confining the hot plasma in the centre of the torus. Therefore, within the core region of a reactor, it is thus possible to achieve the conditions necessary to heat the plasma greater than 10 keV and with a density of the order of $\frac{10^{20} particles}{m^3}$, as required by the Lawson criteria. In a tokamak, the plasma current is induced by applying a current ramp in a central solenoid, which leads to a change in magnetic flux in the central gap of the torus. The solenoid acts as the primary winding of a transformer with the plasma itself acting as the secondary and a current is hence induced in the plasma.

The plasma is then heated by Ohmic power and additional external heating systems as described in section 1.5.

1.4 ITER

ITER is currently the most important step towards the fusion research and is under construction in Cadarache, France [12]. ITER means "The Way" in Latin and in the past it stood for International Thermonuclear Experimental Reactor. This will be the largest tokamak in the world. ITER is the most ambitious energy project signed in 2006 by the European Union, USA, China, Japan, Russia, South Korea and India. The main goals which are expected to be fulfilled from the ITER experiment are: to produce ten times more thermal energy (up to $500\ MW$) from fusion heating than supplied by auxiliary power ($50\ MW$), to produce a steady state plasma with a non-inductive plasma current, to maintain the fusion pulse for up to $400 - 600\ s$, to verify tritium breeding concepts, to refine neutron shield/heat conversion technologies and to develop several technologies and processes needed for a fusion power plant (like advanced materials, superconducting magnets, remote handling, etc.). The experience and results of ITER will be used to prepare another fusion power plant called DEMO (DEMOnstration Power Plant). Beyond ITER, it is envisaged that DEMO fusion reactors could be constructed with the aim to demonstrate electrical power production. The first ITER experimental activity is scheduled for 2025.

ITER will be the first experimental reactor to operate for most of its lifetime with deuterium and tritium mixtures, the reactor will therefore contain a non-negligible quantity of the radioactive material. The magnetic confinement scheme of ITER comprises of a strong toroidal magnetic field of about $5.3\ T$ in the center of the torus plus a poloidal field generated by the maximum plasma current of $15\ MA$ and by the six poloidal field coils, made with the superconducting material $NbTi$. The toroidal field will be produced by 18 coils, made from Nb_3Sn , which is another superconducting material. This material will also be adopted for the central solenoid which is needed to induce the plasma current. All the coils will be kept at 4 K to reach superconductivity. The 3D representation of the ITER tokamak with all the components is shown in Figure 10.

The plasma facing component (PFC) will undergo high heat fluxes and neutron irradiation. Therefore, in order to prevent plasma contamination, the first wall of the ITER tokamak will be covered with suitable materials. ITER will be a machine with a height of $26\ m$ and diameter of $29\ m$. The ITER plasma volume is about $\sim 10^3\ m^3$ (with major radius of $6.2\ m$ and the minor radius of $2\ m$) much higher than in the previous fusion experiments; therefore, large thermal and magnetic energy could be released during the plasma instabilities and could cause severe

damages. Due to the presence of plasma instabilities, the structure will have to resist intense mechanical and thermal stresses. The system of real time survey and control of plasma instabilities will have a fundamental role in the reliability and availability of the reactor.

To test tritium breeding and to shield the coils from the heat and incoming radiation fluxes coming from the plasma, the blanket will be present between the first wall and the coils. A divertor will also be present to remove the plasma impurities and helium (produced by the fusion) from the plasma. It will be subjected to the most intense heat fluxes of the order of several MW/m^2.

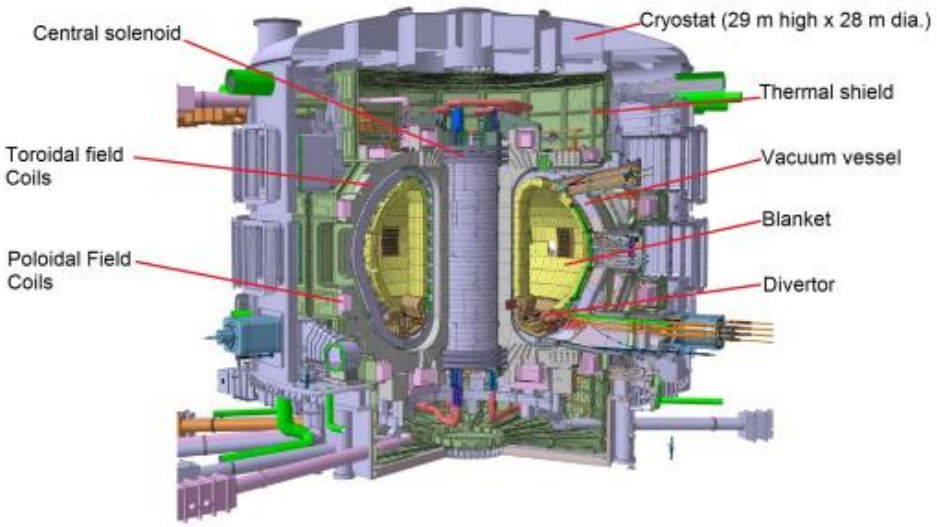

Figure 10: Design of the entire ITER tokamak device.

1.5 Auxiliary Heating and Current Drive

As mentioned in section 1.2.1, the minimum plasma temperature of $\sim 10\ keV$ [13] is required to reach the plasma ignition condition with the required plasma density ($\sim \frac{10^{20} particles}{m^3}$) and confinement time. These calculations neglect the losses due to the bremsstrahlung radiation. In addition, the fusion heating through alpha particles become dominant above the temperature of $5 - 7\ keV$; below this temperature the alpha heating is almost negligible [13]. Therefore, in order to reach the plasma ignition temperature, it is essential to have other heating sources. One of the simplest heating mechanisms for tokamak is ohmic heating. The plasma inside the tokamak behaves like a conductor and the plasma current leads to the heating using the following relation $P = \eta j^2$, where η is the resistivity and j is the current density. It is well known that the plasma resistivity decreases with the increase in temperature i.e $\propto T^{-\frac{3}{2}}$ [13]. The maximum plasma temperature achieved from ohmic

heating for typical reactors parameters is $\sim 3\ keV$ [13]. Therefore, ohmic heating alone is not sufficient to reach the ignition conditions or to reach fusion heating. Thus, one requires auxiliary heating systems to reach ignition conditions. There are two families of the auxiliary heating mechanisms that will complement ohmic heating to bring the ITER plasma to the ignition condition:

1. Electromagnetic waves
2. Injection of high energy particles in the plasma – Neutral beam injection

These two auxiliary heating methods along with ohmic heating in a tokamak are represented in the Figure 11. These systems not only lead to the plasma heating but are also able to drive plasma current if designed properly.

The heating due to electromagnetic waves comprises of electron and ion cyclotron resonance heating (ECRH and ICRH respectively), and the lower hybrid (LH) heating. ECRH, ICRH and LH systems are based on launching electromagnetic waves into the plasma, in order to maximize the energy absorption by matching with specific plasma resonant frequencies.

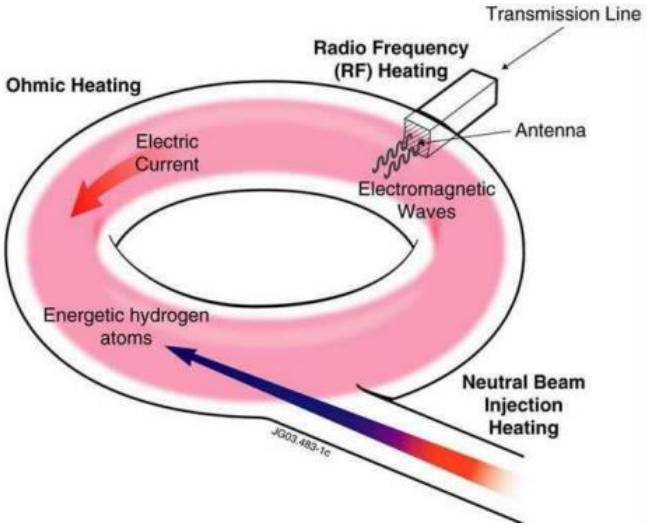

Figure 11: Plasma heating systems.

In ITER, each of these systems is designed to deliver a power of up to $20\ MW$ to the plasma. The typical range of frequency for ICRH is $30 - 55\ MHz$, for LH is $3 - 5\ GHz$ and for ECRH is $110 - 170\ GHz$ respectively. This maximization of the energy absorption at a particular fixed frequency depends on several factors like plasma density and magnetic field. ICRH is normally used for plasma ion heating, but can also be used for central current drive (although with poor efficiency [14]) and plasma stabilization (as it also useful for saw-tooth stabilisation). ECRH is a system which is used to heat the plasma electrons, and EC systems provide the central heating but can also be used to drive localized currents. It also has some

functions related to controlling of plasma stability [15]. Lower hybrid energy transfer is a method to accelerate the plasma electrons using waves at specific frequencies. It is based on the concept of Landau damping [16]. If lower hybrid heating is chosen to be used at ITER then it will have the primary objective of providing off – axis current drive.

The second family of the auxiliary heating comprises of the neutral beam injection (NBI) which is based on the strategy to inject an energetic beam of neutral particles which transfer their energy and momentum to the plasma. In ITER two heating NBIs (HNB) are foreseen with a total power of $33\ MW$ delivered to the plasma [17]. A third heating beam may be added later, bringing the total power that may be injected into ITER up to $50\ MW$. There is another neutral beam for diagnostic purpose (DNB) [17]. The top view of the neutral beam cell in the ITER tokamak is shown in Figure 12. This thesis has been prepared in the frame of the studies for the heating Neutral Beam Injection (NBI) systems and its principles are summarized in the next chapter.

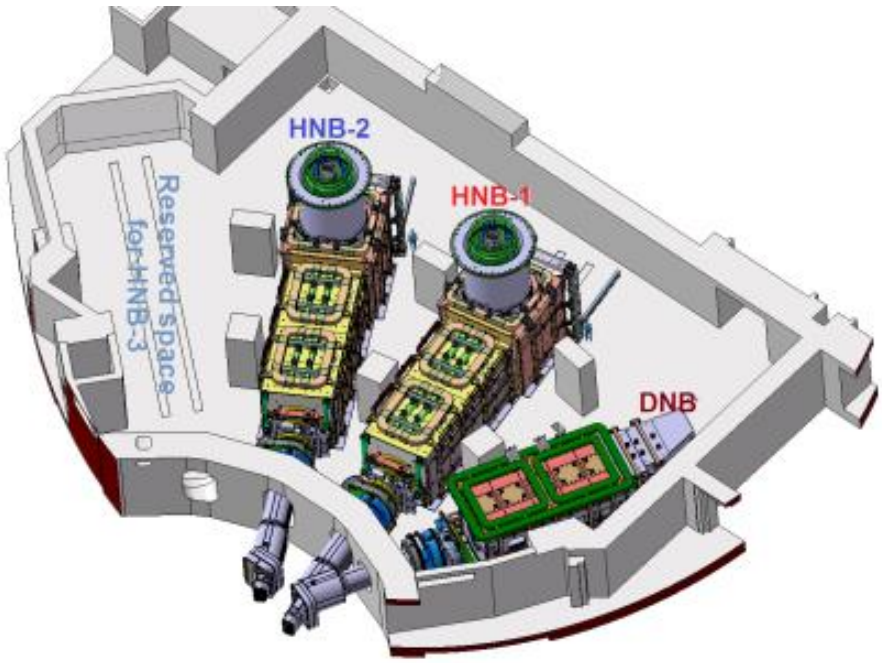

Figure 12: ITER NB cell top view [18].

Chapter 2.

Neutral beam injector

The purpose of plasma heating in fusion devices is to raise the plasma temperature high enough to produce a deuterium and tritium fusion reaction, see equation 1. The required plasma temperature is about $10\ keV$. Since high temperature plasma is confined by a strong magnetic field, the injection of energetic ions from outside to heat the plasma is difficult due to the Lorentz force. The most efficient way to heat the plasma by energetic particles is to inject high energy "neutrals" which get ionized in the plasma. This concept of using energetic neutral beams for heating the plasma was proposed in 1950s [19].

Neutral atoms that are not affected by the strong magnetic confinement field are able to penetrate into the plasma torus, where collisions of the neutral particles with the plasma electrons and ions cause an ionization of the neutral beam. The penetration depth of the neutral beam must not be too long; otherwise the beam would cross the plasma and will damage the opposite side of the first wall. It should not be too short either: otherwise only the plasma edge will be heated. A neutral beam injection (NBI) with beam energy much above the average kinetic energy of the plasma electrons or ions is used ($1\ MeV$ for the ITER NBI [20]). In order to avoid a perturbation of the fusion process, low Z elements similar to the fusion species (H, D or T), are preferred as injected neutral particles.

2.1 Neutral Beam Injection Systems

2.1.1 Reason for negative ion beam

For the creation of the beam there is a choice between the positive or negative ions. It is easier to produce positive ions but their neutralisation efficiency becomes very low for beam energies higher than $100\ keV$ for Deuterium and $40\ keV$ for Hydrogen. The measured neutralization efficiency in negative ion based NBI (Neutral Beam Injector) for a Japanese Tokamak JT-60U is shown as a function of the beam energy in Figure 13. Therefore, a negative ion source was chosen for ITER NBI instead of a positive ion source because of their higher neutralization efficiency at the high-energy [21]. However, electrons are extracted together with the negative hydrogen ions and it is a drawback of negative ion source with respect to positive-ion source.

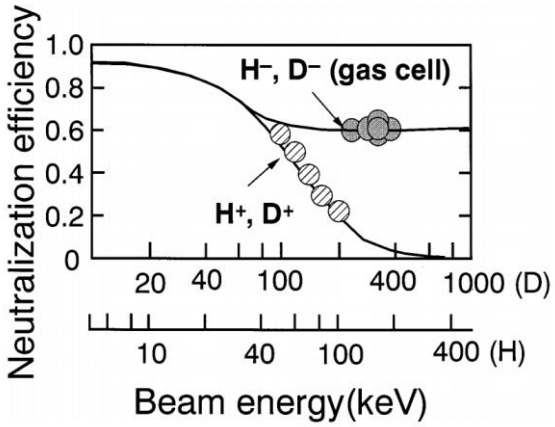

Figure 13: Measured neutralization efficiency as a function of the beam energy in JT-60U[22].

2.1.2 Basic components of ITER NBI systems

The main components and the schematic of the neutral beam injector (NBI) are shown in Figure 14. The heart of the NBI is the ion source (plasma source with an extraction system), where hydrogen or deuterium ions are generated by a plasma source and are then extracted and accelerated to a desired energy by an accelerator. The ion source together with the accelerator is known as the beam source. During the acceleration stage the negative ion beam produced in the source has to be accelerated to the nominal energy of the injector limiting to the maximum extent the losses resulting from unavoidable parasitic processes which mostly involve the destruction of the negative ions. The main phenomena which are responsible for the losses in the accelerating region are: stripping losses; secondary electron produced, disposed and transmitted; and the back-streaming of positive ion accelerated toward the plasma source. The ion beam then enters a neutralizer cell in which the accelerated ions is converted to energetic neutrals typically by the charge exchange process with collisions of the background gas. Consider, for example, energetic negative deuterium ions, during their travel through the neutralizer, several collisions takes place between the D^- and the D_2 gas, which leads to the formation of D^0, by simple stripping of the outer electron from D^- and Double stripping leads to the formation of D^+; D^+ is also created by re-ionization of the D^0 produced from D^-. At the exit of the neutralizer, the beam will pass through a residual ion dump (RID), which creates an electrostatic field that is used to deflect the charged particles of the beam onto a set of plates, leaving the neutral beam to impinge onto the calorimeter located just downstream of the residual ion dump. The energetic neutral beam is then injected to the tokamak plasma through a drift duct which connects the injection port of the plasma device. The residual neutral gas is removed with the help of high speed vacuum pumps. It is worth

noting that it is possible to have a beam of either hydrogen or deuterium neutral atoms from ITER NBI.

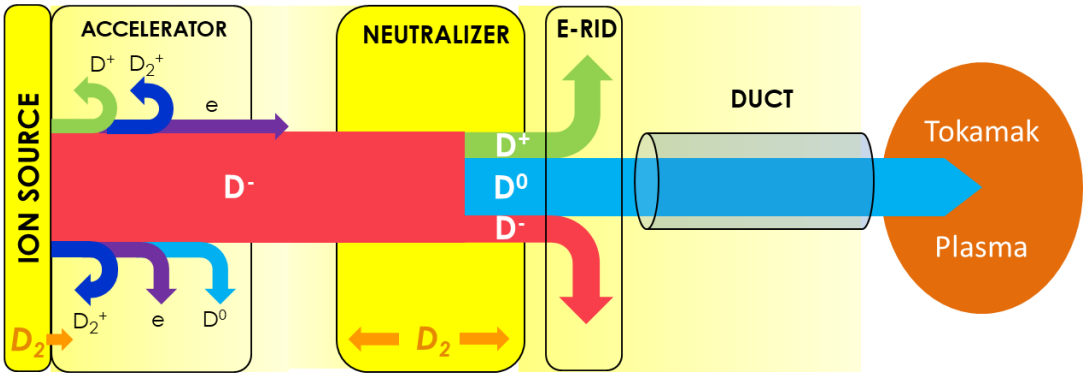

Figure 14: Schematic of a neutral beam injector.

2.2 Overall ITER NBI requirements

Neutral beam energy of 1 MeV for deuterium was chosen in order to satisfy the central heating and current drive requirement for ITER [23]. The beam power has to be maintained for pulse duration of 3600 sec. Ion current of 40 A D^- is required in order to achieve a final heating power of 16.5 MW. The installed power has to be higher in order to account for the neutralization losses (40%) [24] and transmission losses in the beam transport.

A negative-ion source and an extraction area delivering a current density of 286 Am^{-2} D^- [25] is necessary to provide this current. The large-scale extraction area must have plasma homogeneity better than $\pm$ 10 % for the local current density over the area to prevent damage to the system by unfocused parts of the ion beam. In order to avoid damage on the grid structure of the accelerator by high-energy electrons, it is necessary to remove these co-extracted electrons at a low energy immediately after their extraction. This process causes a heat load on an electron sink, which is subject to the technical limitations of the cooling. Thus, it is necessary to maintain an electron-to-ion current density ratio < 1. Furthermore, the operational pressure of the ion source has to be limited to 0.3 Pa in order to reduce destructive losses by collisions with residual gas particles in the extraction and acceleration systems.

The parameters requested for ITER Heating Neutral Beam Injectors are reported in the Table 1.

Table 1: Main parameters require for ITER HNBI [25]

Ion species	H^-	D^-
Beam Energy [MeV]	0.8	1
Beam current [A]	40	40
Pulse length [s]	1000	3600
Extracted current density [Am^{-2}]	329	286
Extracted current [A]	66	56
Accelerated current [A]	46	40
Electron-ion-ratio	<1	<1
Extraction Voltage [kV]	10	10
Source pressure [Pa]	0.3	0.3

For this thesis the most interesting component of the NBI system is the ion source and therefore only its description is provided in detail in the following section.

2.3 Ion Sources

The ITER NBI is composed of an ion source (composition of plasma source and extraction system) capable of producing 40 A of D^- ions which are accelerated at the energy of 1 MeV [26]. There are two different concepts which can be employed in the NBI system for the generation of energetic ions in a source facing an expansion region where the hot plasma is confined. These are arc sources and inductively coupled (IC) radio frequency (RF) ion sources, both are described in the following sections:

2.3.1 Arc sources

The arc-source is based on applying a dc-voltage of about 100 V between heated cathode filaments and the source walls. The electrons emitted by the filaments are accelerated into the source, where ionization of gas molecules creates plasma. Heated tungsten filaments are used as cathodes with typical total arc currents in the order of 1000 A, producing filament temperatures between $1700 - 2700$ ℃. Arc-sources are reliable and have been used since the development of the first NBI systems. For example, the large KAMABOKO source developed for JT-60 NBI has successfully demonstrated the production of powerful beam of 6.7 MW, 360 keV H^- [27]. Nevertheless, these sources have severe disadvantages. The tungsten evaporates continuously into the source during operation [27], which limits the life time of the filament and it thus requires frequent replacement [28]. In the ITER neutral beam injector design it was assumed that the filament's lifetime would allow 200 h of operation before they needed to be

replaced [27]. Tungsten deposition also contaminates the inner walls of the source changing its surface characteristics, which is especially relevant for negative-ion production.

2.3.2 Inductively coupled (IC) Radio Frequency (RF) ion sources

In 2007, the radio frequency driven negative ion source [29] working at 1 MHz was chosen by the ITER council as the reference source for ITER NBI [30]. The principle concept of the inductively driven RF negative ion sources was developed by the Max-Planck-Institut fur Plasmaphysik (IPP), Garching, Germany [29]. The principle setup of the IPP prototype ion source is shown in Figure 15. The source consists of three parts: the driver, where the RF is coupled to the plasma by a coil; the expansion region, where the plasma expands into the actual source body; and the extraction region.

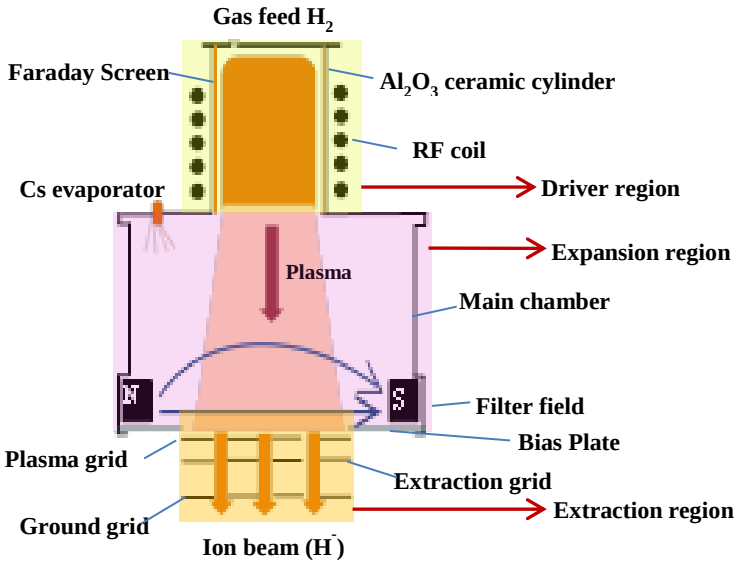

Figure 15: A typical scheme of the inductively coupled radiofrequency IPP type ion source.

2.3.2.1 *Plasma formation*

The partially ionized plasma is created within the driver. A driver is composed of a ceramic cylinder, made of alumina, around which coils are wound. The coupling between the water cooled coil and the plasma is purely inductive because of the presence of an edge-cooled Faraday shield within the cylinder which protects the alumina from the interaction with the plasma. The Faraday screen is made of copper material and in some experiments can be coated with molybdenum.

The high power RF source operates typically in the pressure region $\sim 0.3\ Pa$, in hydrogen and deuterium. The electron density and temperature in the driver axis is typically in the order

of $5 \times 10^{18} m^{-3}$ and $8\,eV$ [31]. However, the precise values depend on the RF generator power, the pressure and the gas type.

2.3.2.2 *Negative ion production*

After the formation of the plasma, its diffusion takes place in the expansion region. A stable source body temperature is favourable for stable plasma conditions, in particular for caesium seeded discharges. During the process of expansion, the temperature of the electron decreases from about $8\,eV$ in the driver to about $4\,eV$. This condition is favourable for the "volume process" to occur for negative ion production. In this process, the production of negative ions takes place by the dissociation of H_2/D_2 molecules, which were excited vibrationally by a collision with an electron [31].

$$\begin{matrix} H_2 + e \rightarrow H_2(v) + e & (v) \geq 5 for\ H, v \geq for\ D \\ H_2(v) + e \rightarrow H + H^- \end{matrix} \quad (8)$$

The just produced negative ions are prone to the reactions of mutual neutralization and electron detachment by impact with electrons, atoms or molecules. To produce the flux of ions in order to achieve the requirements of the ITER NBI, the volume process alone is not sufficient, much more negative ions are instead produced with a "surface process", in which the atoms in the plasma impinges on the Plasma Grid (PG) and pick up the extra electron. The expansion region is separated from the acceleration region by the PG. A material with a lower work function (1.6 eV), caesium is used as layer over the PG to facilitate the production of the negative ions. The deposition of Cs is performed with an oven which releases Cs vapours inside the source. Since Cs liquefies at $28\,℃$, the temperature of the main chamber is controlled; allowing adjusting temperatures between 20 to $60\,℃$ to avoid the uncontrolled deposition of this substance; the optimal deposition of Cs on the PG has been obtained by heating the plasma grid at $150 \pm 50\,℃$ [32] to optimize the H^- production rate.

2.3.2.3 *Extraction of ions*

Magnetic field near the PG is necessary to prevent electrons reaching the PG and enter the extraction region. The field can be strengthened or weakened by mounting additional permanent magnets in the corresponding polarity outside of the source body which helps in reaching the desired electron-ion ratio. For example, with an increased filter field the electron/ion ratio for deuterium can be suppressed near or just below unity [33].

As shown in Figure 15, the extraction regions comprises of the plasma grid, the extraction grid and the grounded grid. The plasma grid and the source body are at high voltage ($-20\,kV$). The extraction voltage (typically $5 - 10\,kV$) is applied between the plasma grid and the extraction grid. The negative ions created by the surface process are backscattered

towards the expansion region; however near the PG holes they are attracted by the electric field on the other side of the PG. In order to reduce the number of co-extracted electrons, the strength of the magnetic filter field has to be adjusted to the gas species; for deuterium higher field strengths are needed than for hydrogen. In addition, the plasma grid is positively biased against the source body.

2.3.3 Advantages of IC RF sources over arc sources

The RF sources have several advantages [29] in comparison to the previously foreseen arc driven ion source [34] :

- In RF sources, only the maintenance of Cs supply system is required. In principle the RF source by itself is maintenance free. This feature in particular is very advantageous in ITER because of its high radioactive environment; ITER requires remote handling and maintenance.
- In arc driven sources, the tungsten evaporated from the filament dominate the impurity content and the wall surfaces. Whereas, in RF sources, the source wall material can be chosen freely. This is advantageous with respect to the Cs dynamics and chemistry.
- RF sources have no electrode like a filament, usually used in an arc driven sources, which limits the source lifetime by its erosion and fragility [35].

2.4 PRIMA - The ITER Neutral Beam Test Facility

The parameters required for ITER have never been achieved before all together in a single device. Therefore, it was necessary to create a new experimental facility addressing all the current issues and to fill up all the residual technical and scientific gaps. For the success of the future operation of ITER NBI heating, a supporting program at the Consorzio RFX in Padova, Italy is being pursued. This program aims at the development of the ITER neutral beam test facility (NBTF) called PRIMA. It is an ITER test stand with the purpose of realizing the full scale prototype of ITER NBI [36]. PRIMA stands for Padua Research on ITER Megavolt Accelerator and it will host two experimental devices currently under construction and installation: MITICA and SPIDER [36]. 3D CAD view of the PRIMA facility is shown in Figure 16.

MITICA (Megavolt ITER Injector and Concept Advancement) is the full scale prototype of the NBI for the ITER experiment and SPIDER (Source for Production of Ion of Deuterium Extracted from RF plasma) will focus on the development of the NBI ion source.

The beam source for SPIDER will be characterized by a lower acceleration voltage (100 kV) than the MITICA (1 MV). This is due to the fact that SPIDER will focus on the optimization of

the negative ion beam creation process. The full acceleration and neutralization processes will be the scope of MITICA injector.

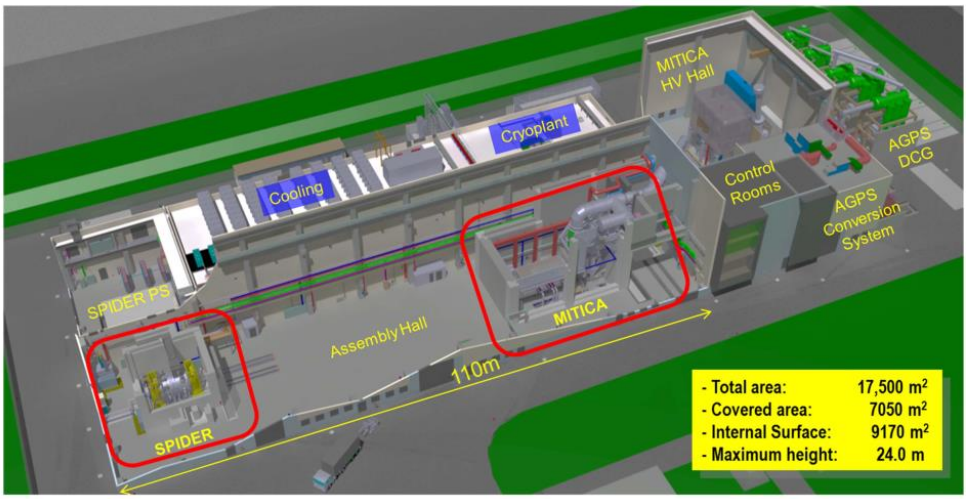

Figure 16: 3D CAD view of the PRIMA facility [37].

The PRIMA facility is now completed (see Figure 17), the SPIDER device is currently under commissioning with the scheduled experiments in 2018 and the design of the MITICA has now been completed.

Figure 17: Aerial view of the PRIMA buildings[37].

2.4.1 SPIDER

SPIDER experiment will enter into operation before MITICA and, after the installation of MITICA, it will run in parallel with it. It has the same size as the ITER HNB ion sources and the same extractor design. It provides the extraction and acceleration of $H^-$and D^- up to 100 keV

for pulse duration of 3600 s. It also features ITER like filter field configuration. Moreover, a wide set of diagnostics supports the beam characterisation and design validation of the components. This is necessary for adjustments and optimizations during operation, aiming to fulfil SPIDER mission to optimize the negative ion source performance [37] for the ITER HNBs. The main parameters for SPIDER are listed in Table 2. A view of the SPIDER in-vessel components is shown in Figure 18.

Table 2: The main parameters for SPIDER [37]

Ion species	D^-	H^-
Beam energy [keV]	100	100
Pulse length [s]	3600	3600
Extracted current density [A/m^2]	> 285	>355
Extracted electron to ion ratio	< 1	< 0.5
Source pressure [Pa]	0.3	0.3

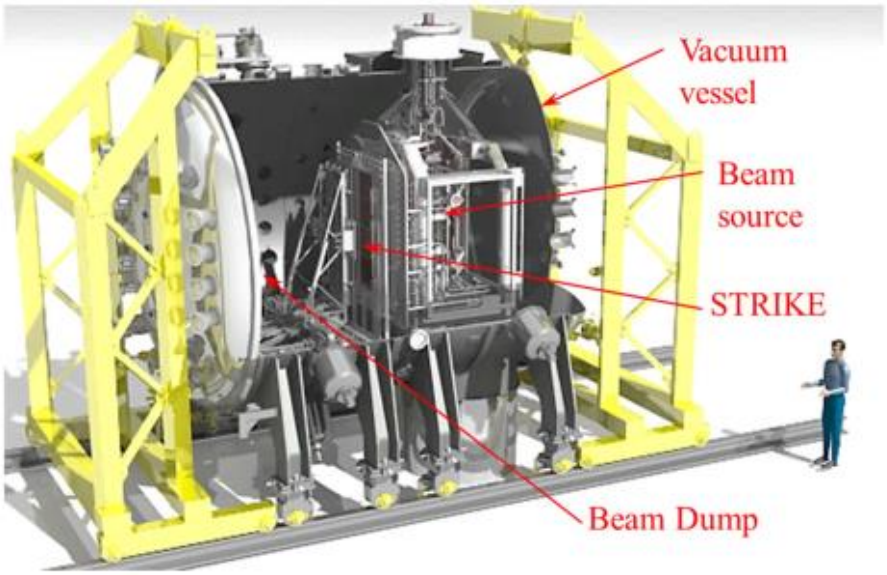

Figure 18: SPIDER view with in-vessel components [37].

2.4.1.1 *Beam source (BS)*

An exploded view of the SPIDER beam source (BS) is shown in Figure 19. The SPIDER Beam Source (BS) is designed to accelerate the required negative ion beam up to 100 keV. The RF driven negative ion source, consists of a plasma source and an extractor.

The process for the production of deuterium neutral particles originates from deuterium (D) plasma produced by means of 8 inductively coupled radiofrequency generators (operating at 1 MHz) in a chamber. Such volume faces a surface (Plasma Grid) previously covered with a

caesium layer, whose interaction with Deuterium can generate a deuterium ion having one additional electron (D^-). The SPIDER grid system consists of a Bias Plate (for controlling the potential close to the PG), a Plasma Grid (for negative ion production) and a filter field is present to suppress every electron near the PG, an Extraction Grid (is for negative ion extraction and dumping of co-extracted electrons and is polarized with respect to PG) and a Grounded Grid (polarized with respect to extraction grid is for negative ion acceleration). As the last accelerating grid (grounded grid) is placed at zero potential, the accelerating voltage is 100 kV and another 12 kV is needed for the ion extraction between the extraction grid and the plasma grid, the SPIDER source is at -112 kV potential with respect to the zero potential reference. This potential distribution leads to a specific isolating system design and to a specific design of the source electric and hydraulic service feedthroughs [37].

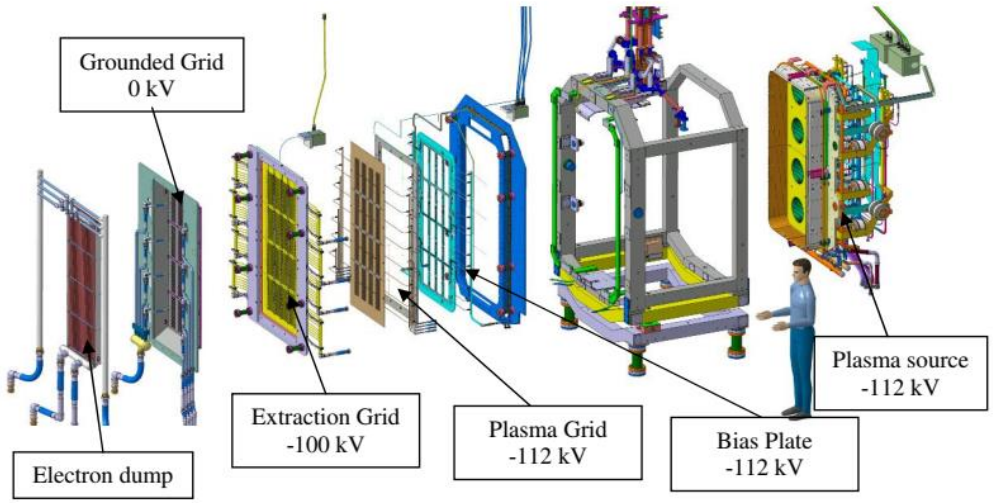

Figure 19: An exploded view of SPIDER beam source [38].

2.4.1.1.1 Plasma source

The SPIDER plasma source is shown in Figure 20. The plasma source is a chamber of following dimensions: 1.8 m height, 0.6 m width and 0.2 m long. Eight drivers are placed on the rear side of the chamber. On the rear of the source three caesium ovens and the load adaptation capacitors for the RF circuit are mounted; all the hydraulic connections for the source component cooling water, coming from the hydraulic bushing are also routed here. The source lateral walls, which house permanent magnet systems for magnetic confinement in the main chamber and the bottom of the plasma chamber (the plasma driver plate), are actively cooled as well. Finally, the plasma source chamber is open in front of the plasma grid Figure 19.

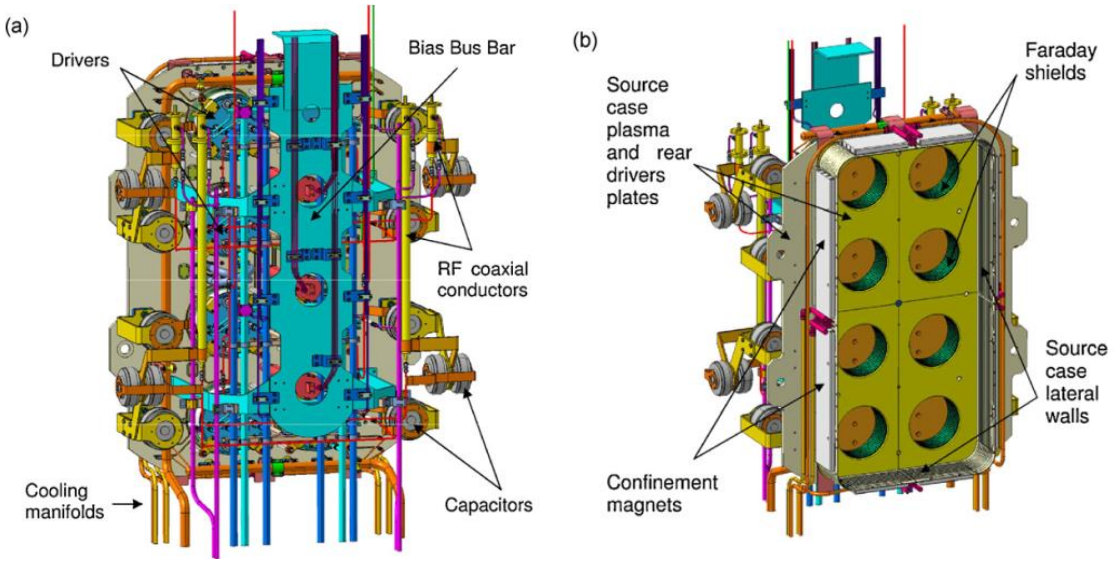

Figure 20: Isometric views of the SPIDER RF plasma source: (a) rear and (b) front side [39].

2.4.1.1.1.1 RF Driver

A driver is composed of a ceramic cylinder, made of alumina, around which coil is wounded. The radiofrequency (RF) current at 1 MHz flows through this coil. The RF driver is a component where the plasma is produced by radiofrequency electromagnetic fields. Thus, in order to protect the ceramic part from the plasma, the driver inner part is composed of an actively cooled copper protection shield and a permanent magnet system for plasma confinement. A 3D CAD view of one driver is shown Figure 21 while its cross section is shown in Figure 22.

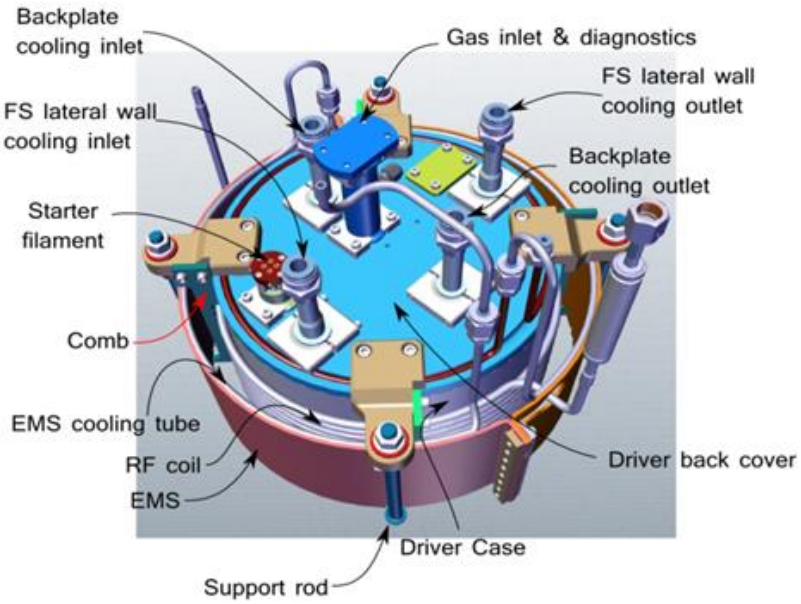

Figure 21: 3D CAD view of the driver with the main components.

Starting from the external region, the main components found in a driver are: four support rods relatively displaced at 90° to mechanically hold the components; the electromagnetic shield (EMS), at the ion source potential, surrounding the coil and actively cooled; four so called "combs" made of Vespel SP-1 to support the coil; the actively cooled copper coil; the insulating driver case (DC) made of Aluminium Oxide; the copper Faraday Screen (FS) at ion source potential coated with a Molybdenum layer. At the top there are the back plate and the back cover.

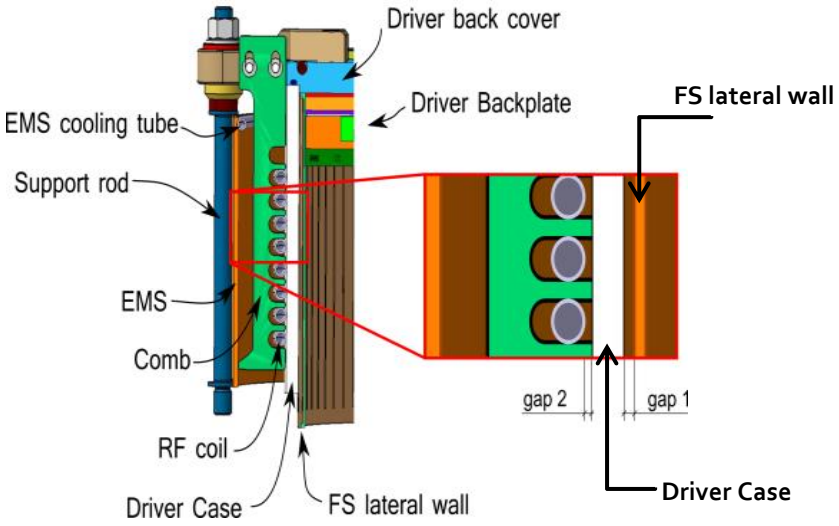

Figure 22: cross section of the driver with the main components.

In Figure 22 it is important to focus on two mentioned gaps. Gap1 is the distance between the Faraday Shield lateral wall and the Driver Case (DC) and it is nominally equal to 2 mm and gap2 is the distance between the coil and the driver Case and is nominally equal to 0 mm, since the coil is tightly wound around the DC. However, the coil can be mechanically close to the Driver Case only locally but not along all its development. Gap1 is within the Driver Case at the nominal pressure of 0.3 Pa, while gap2 is outside the driver, where the pressure is estimated to be 65 mPa [40]. High electric fields are foreseen within the small gaps in the driver which could lead to possible electrical break downs. At full power, the voltage across each RF coil changes in dependence of operational parameters and plasma impedance; it is estimated to be 12.2 kV rms in nominal conditions (considering the perfect matching operational frequency) [41].

2.4.1.1.1.2 RF circuit

In order to have plasma with desired conditions, the RF coil must be properly matched with the RF generator (at a frequency of 1 MHz) using a matching circuit. The 8 drivers of the

ion Source are arranged in four couples, fed by 4 separated RF circuits. In each circuit, the series of two RF coils is connected to a matching network [42], composed of series and parallel capacitors installed in the rear side of the beam source, see Figure 23. Each RF circuit is supplied by a 200 kW RF generator, part of the Ion Source and Extraction Power Supply (ISEPS) system [43]. Matching can be done either by a variable capacitor in the external matching circuit in series to the RF coil or by changing the generator frequency [44] [45] .

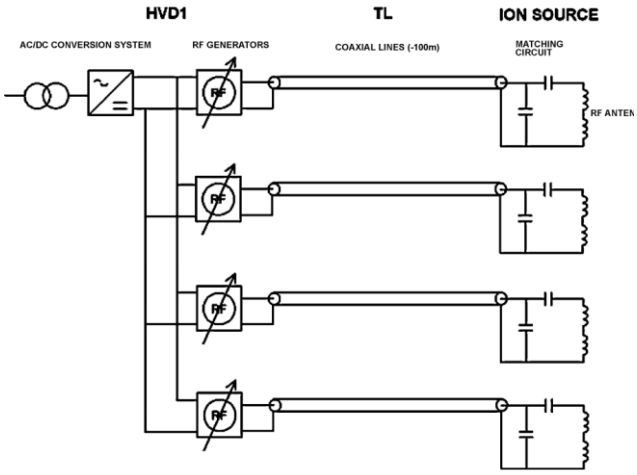

Figure 23: Schematic drawing of the RF power supply circuit [42] (HVD stands for high voltage deck).

2.4.1.1.1.3 Electrostatic screen

The whole Ion Source with the drivers and matching circuits are enclosed within an electrostatic screen to prevent breakdown to the grounded vacuum vessel (see Figure 24). The electrostatic screen is composed of drilled plates to allow the evacuation of the gas towards the vacuum vessel which is pumped to the nominal pressure of 10 mPa for SPIDER. Because of outgassing, the driver coil is expected to work at higher pressure than the pressure at the electrostatic screen outer surface.

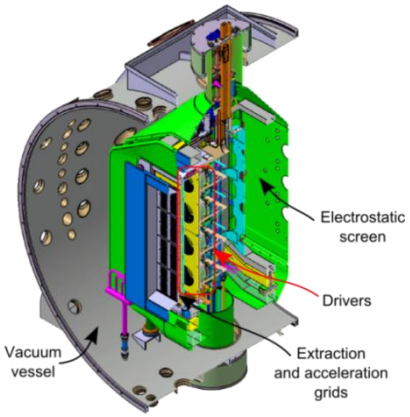

Figure 24: Cut view of the SPIDER vacuum vessel and internal components.

2.4.1.2 *Diagnostics*

The wide set of SPIDER diagnostics, together with the numerical codes to analyse the experimental results, are expected to provide design validation and help in operation optimization. Some of the source diagnostics [37] includes: electrostatic probes (for measuring plasma uniformity, electron density and temperature), source optical emission spectroscopy, calorimetry and surface thermocouples, electrical current measurements and laser absorption.

Besides the Beam source (BS) the SPIDER experiment will also host a special diagnostic calorimeter inside the vacuum vessel called STRIKE (Short-Time Retractable Instrumented Kalorimeter Experiment). The measurements of the beam uniformity and divergence will be possible from the data collected with STRIKE. Many other optical diagnostics are also present on the outside of the vacuum vessel. They will diagnose the beam through dedicated aperture rows (portholes) around the vessel.

2.4.2 MITICA

A cutaway view of the MITICA components is shown in Figure 25. The beam generated from the MITICA device shall be able to transfer a power of 16.5 MW to the plasma for 1 hour continuously. The beam of neutral particles will be accelerated up to the energy of 1 MeV. The beam source concept for both MITICA and SPIDER is the same [46] , i.e., they share the same Plasma Source and also the Bias Plate, the Plasma Grid and the Extraction grid are coincident. The difference between the two sources is essentially the presence of demountable hydraulic connections in SPIDER, which are not used in MITICA. The ion source is held at a negative potential of 1 MV and D^- ions are accelerated up to ground potential by an accelerator which comprises of a system of 5 grids, held at different growing potentials by steps of 200 kV, applied to each couple of grids. At the end of the accelerator, a beam of deuterium negative ions accelerated to energy of 1 MeV will be obtained and a current of 40 A will be extracted.

Once the acceleration stage is performed, the beam will then pass through the Neutralizer where a cloud of deuterium gas neutralized the ion beam through a charge exchange process. At the exit of the neutralization process, the beam will pass through an electrostatic field (Residual Ion Dump, RID). The electric field deflects the charged particles of the beam onto a set of plates, leaving the neutral beam to impinge onto the calorimeter located just downstream of the residual ion dump.

In this configuration the injector can be commissioned and the neutral power dumped onto the calorimeter can be measured. In the ITER NBI, the calorimeter will be opened and

the neutralized deuterium beam of 16.5 MW power will flow along the duct until the ITER plasma is reached.

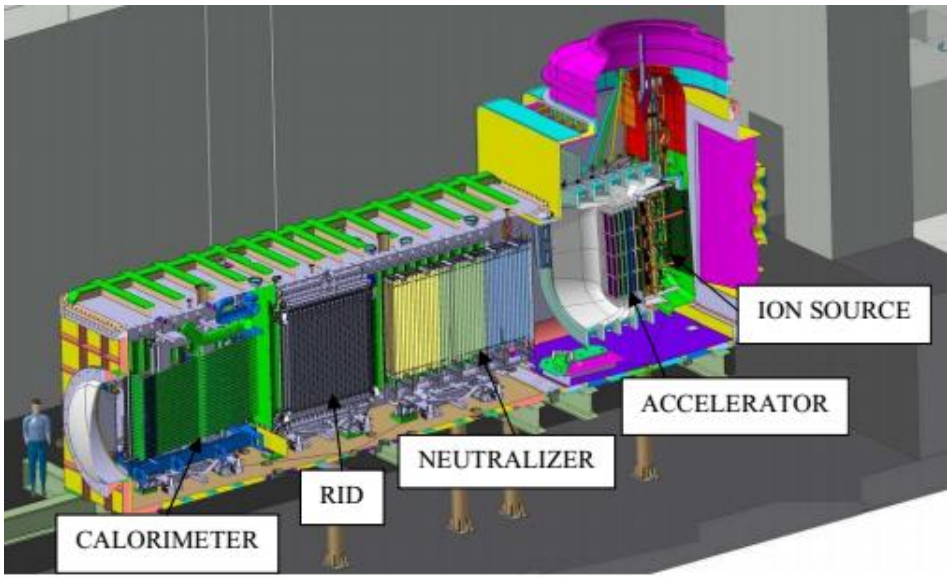

Figure 25: A cutaway view of MITICA components.

The main parameters of MITICA are summarized in the Table 3.

Table 3: The main parameters of MITICA [37]

Ion species	D^-	H^-
Beam energy [MeV]	1	0.87
Beam power [MW]	16.5	16.5
Pulse length [s]	3600	3600
Acceleration current [A]	40	46
Extracted current density [A/m^2]	285	355
Extracted electron to ion ratio	< 1	< 0.5
Source pressure [Pa]	0.3	0.3

2.4.2.1 *Diagnostics*

MITICA will allow much less access than SPIDER, and will be subject to a neutron rate intermediate between SPIDER and ITER HNBs [37]. In the MITICA experiment it is possible to have several diagnostic systems which will be able to provide measurements on various generated beam parameters, in different phases and thus providing the validation of the accuracy of design.

The design and development of MITICA diagnostics is in progress [37]. The main system is the large set of thermocouples and optical thermal sensors [47], electrostatic sensors to be installed in the neutralizer and in the ERID have been designed and integrated in the CAD model [48]. There will be some diagnostics to derive the beam intensity profile at the beam

dump [49]. These will likely be the only diagnostics available in the ITER HNB, because they can survive the high neutron flux. In MITICA they will be complemented by other diagnostic techniques like beam emission spectroscopy [50], beam tomography [51] and neutron imaging.

2.5 Ion sources of interest for this thesis

Apart from IPP and Consorzio RFX, RF plasmas are employed in negative hydrogen sources also in other laboratories like Tohoku University in Japan [35] and the SNIF experiment in UK [52]. The ion sources of interest for the work of this thesis are ELISE and NIO1 and they are described in the following sections.

2.5.1 ELISE

ELISE is the most recent test facility in operation at IPP. It stands for Extraction from a Large Ion Source Experiment [32] [53]. ELISE is an important step towards the full ITER NBI source: it supports the ITER design and helps to gain early experimental experience with beam extraction from a large RF source. It is half the size of the ITER NBI ion source and 4 times the size of the IPP prototype ion source. The comparison between the size of the IPP prototype ion source, ELISE and the ITER HNBI ion source is shown in Figure 26.

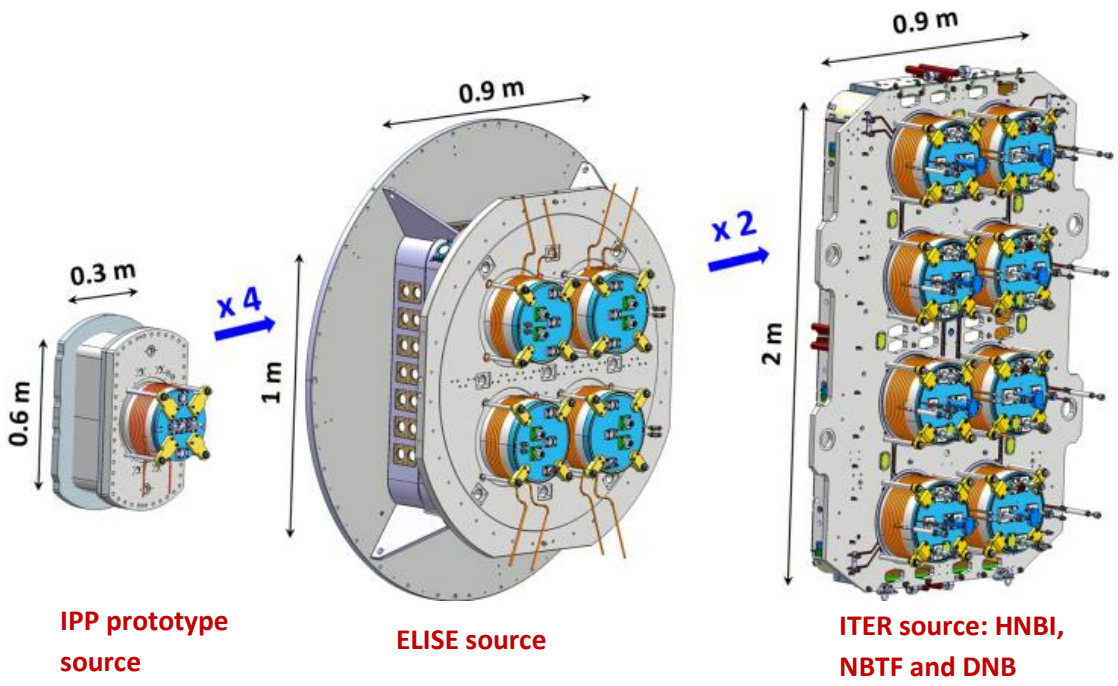

Figure 26: Modular concept of the RF-driven beam sources: from the prototype source via the ½ size ITER source at ELISE to the ITER source [25] (the diagram shows the rear view of the driver arrangement).

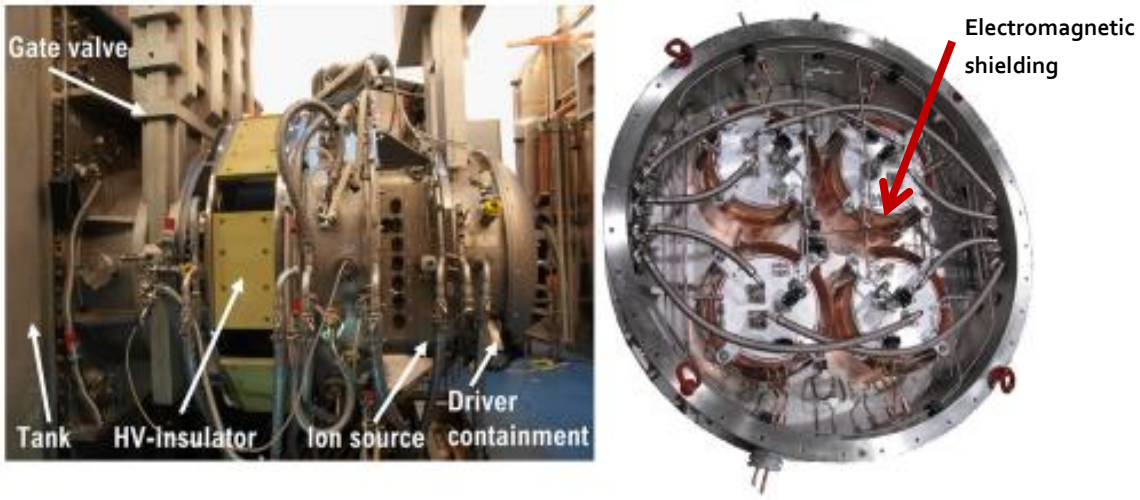

Figure 27: ELISE test facility, left: side view showing main components, right: view into open driver containment with four drivers, RF shielding and all supplies connected [53].

The view of the ELISE test facility is shown in the Figure 27 (left view). It is composed of 4 drivers, open to a common expansion region; the view into the open driver containment can be seen in Figure 27 (right view). The extraction area is half the one foreseen for the ITER NBI; having the same current density, the total current rated for $20\ A$ for deuterium. The three grids (plasma, extraction and grounded grids) have 640 apertures each, which have a diameter of $14\ mm$ and $20\ mm$ apart from each other both in vertical and horizontal direction. Because of the limitation of the high voltage power supply the extraction of the ions can be performed in intervals of 10 s separated by $3\ min$, while the plasma in the source can be sustained up to 3600 s.

The parameters achieved so far in ELISE ion source against the ITER requirements is given in Table 4 [25].

Table 4: ITER requirements and the achievements at the ELISE source (at 0.3 Pa) [25]

	ELISE (half- size ITER source)		**ITER NBI requirements**	
	H^-	**D^-**	**H^-**	**D^-**
RF pulse length [s]	1000	3600	1000	3600
Extracted current density [Am^{-2}]	217.2	58.5	329	286
Extracted current [A]	21.4	5.8	66	56
Accelerated current [A]	17.9	5.2	46	40
Electron-ion-ratio	0.97	0.92	<1	<1
RF power/driver [kW]	53	21	100	100
Extraction Voltage [kV]	10	4.5	10	10

2.5.2 NIO1

To support the activities for the development of the ITER NBI sources and to provide both a benchmark for codes and a facility for quick and simple manufacturing tests, a reduced size system of these ion sources called NIO1 [54][55] is built and constructed at Consorzio RFX. The aim of the experimentation on NIO1 is to optimize the functioning of negative ion sources; the facility will be used to test materials and the instrumentation foreseen for SPIDER and MITICA.

NIO1 stands for (Negative Ion Optimization 1) and it operates with a nominal H^- beam current of 130 mA accelerated at 60 keV and a working frequency of 2 MHz at a maximum RF power of 2.5 kW. The NIO1 test facility is shown in Figure 28 . It consists of an ion source head, the acceleration column, a pump cross, and the diagnostic chamber, all placed in vacuum. The major electrodes in the acceleration column are the plasma grid (PG, nominal voltage −60 kV), the extraction grid (EG, −52 kV) and the post-acceleration grid (PA, at ground). The source head is cantilevered on the PG outer flange and on the accelerator column, which are supported by the pumping cross and an additional support. The source head is enclosed by a High Voltage Deck (HVD), which supplies cooling and electric power connection to the ion source. Among others, HVD contains the RF generator, the RF matching box, the gas dosing valve, the low voltage power supplies for a filter field circuit, the bias plate and the source bias, and the HV supply for the EG. The power supply and the cooling of the system were dimensioned in order to allow the continuous (> 1000 s) operation of the source.

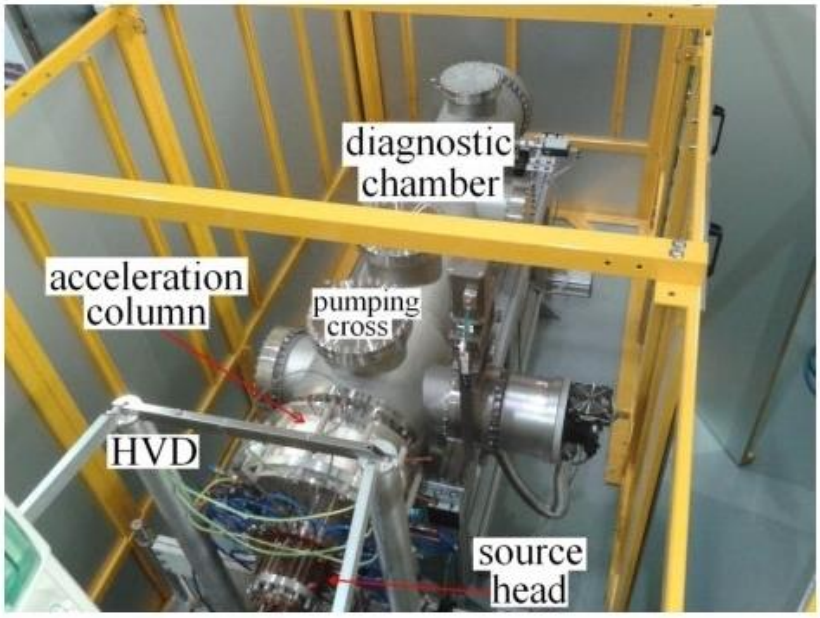

Figure 28: NIO1 experimental facility (here HVD stands for high voltage deck) [55].

The parameters for NIO1 ion source against the ITER requirements is given in Table 5 [25].

Table 5: ITER requirements and the NIO1 source parameters

	NIO1	**ITER NBI requirements**	
	H^-	**H^-**	**D^-**
RF pulse length [s]	1000	1000	3600
Extracted current [A]	0.13	66	56
Accelerated current [A]	0.13	46	40
RF power/driver [kW]	2.5	100	100
Extraction Voltage [kV]	10	10	10

Part 1: Studies on the power transfer efficiency of the inductively coupled radio-frequency ion sources

This research started with an aim to evaluate the power transfer efficiency of the driver of an ion source and to develop suitable models that can permit in the future to also explore possible improvements. The success in the increment in the RF power transfer efficiency to the plasma could permit a decrement in the feeding power to the ion source which may lead to a lower requirement for cooling and on the electrical insulation of the RF circuit components installed on the source.

Overview and prior work

Several theoretical and experimental studies (see [56][57][58][59][60][61][62]), are available in the literature from the 90's, which focus on the inductive discharges for several different applications. Out of these we will direct our attention towards two main aspects - the plasma heating process and the electrical coupling of the plasma in the driver region of the IC RF ion sources. The results found in previous studies on these two aspects are summarized in the following paragraphs.

In the driver region, the power is transferred from coil to the plasma electrons by collisional (ohmic) and collision-less (stochastic) heating processes [56]. Initially, the acceleration of the electrons by RF fields followed by randomization of their velocities in collisions with heavy particles was considered as the main heating mechanism [56]. Other particle heating mechanism is possible in low–pressure regime where a spatially non uniform electric field by itself might lead to electron heating, provided that the electrons have thermal velocities sufficient to sample the field inhomogeneity. This was first shown analytically by Landau [63]. The collision-less damping of the electrostatic wave exists in warm plasma and is referred to in literature by various names like collision-less, non-collisional, stochastic, or anomalous heating. Based on the direct measurements of the electrical characteristics of the inductive discharge, Godyak et al. [58] suggested the existence of stochastic heating in low pressure inductively coupled plasma (ICP). The work of Turner [64] indicated that the various characteristics of the plasma source can define the region of the onset of collision-less heating. Both collisional and collision-less heating processes are considered in this thesis and their effectiveness for the evaluation of power transfer in IC RF ion sources are discussed.

In one of the recent works by Kralkina et al [65], it has been shown for the noble gas discharges like Argon, that the plasma equivalent resistance depends upon the geometry of the source, electron density, gas pressure, power and the applied frequency. It exhibits a non - monotonic behaviour with respect to electron density. He also suggested that the optimal operating RF frequency for small diameter (5 cm) ion sources lies in the range 13-41 MHz whereas in case of large diameter (50 cm) plasma sources, it is close to 13.6 MHz (which is also the common working frequency for IC RF discharges). However, in 1999, Godyak et al [60] showed experimentally that the power transfer efficiency for Argon plasma does not depend on operational frequency for the planar coil. Hence, it is thought provoking to see the behaviour of power transfer efficiency and plasma equivalent electrical parameters as a function of frequency as it is one of the main electrical parameters which can be externally controlled.

Outline for the next few Chapters

This part of the thesis presents an overview of the studies (see Chapter 3) addressed to set up a methodology (see Chapter 4) focusing on the evaluation of the plasma electrical parameters and the power transfer efficiency (PTE) to the plasma. In particular, the methodology is applied to two ion sources:

- To the simplified driver of the ELISE source; characterized by a maximum power per driver of about 90 kW [53], see Chapter 5.
- To the driver of the NIO1 source; characterised by a maximum power of about 2.5 kW [55], see Chapter 6.

Chapter 3.

Different models and formalism involved in the estimation of the power transfer efficiency

In the first part of this section, the analytical model of different mechanisms affecting the power deposition in plasma in an inductively coupled plasma sources is described. Then the development of two electrical models describing the coupling of the RF power from the coil to the plasma is detailed. One is based on a transformer model and the second one is an improved model based on multi-filaments (mutually coupled currents filaments) that has been developed to accounts for the power losses on the RF coil, the plasma and the passive metallic structure.

3.1 Analytical model of power deposition in the inductively coupled plasma sources

3.1.1 Identification of the plasma parameters - the electro-dynamic approach

The plasma inside the inductively coupled RF ion source is mainly composed of charged particles (electrons and ions) and uncharged particles (neutral atoms). To determine the plasma dynamics, fluid equation can be used. The momentum balance force equation considering the fluid motion for one species (either electrons or ions) with the particle density n, is given by the following equation [56]:

$$mn\left[\frac{\partial \boldsymbol{u}}{\partial t} + (\boldsymbol{u}\cdot\nabla)\boldsymbol{u}\right] = mn\frac{d\boldsymbol{u}}{dt} = qn(\boldsymbol{E} + \boldsymbol{u}\times\boldsymbol{B}) - \nabla p - mnv_c\boldsymbol{u} \qquad (9)$$

The first term in the left hand side (LHS) is the acceleration term while the second term is the inertial term. Here $\boldsymbol{u}$ is the mean velocity of the particles. The first term in the RHS is the Lorentz force with $\boldsymbol{E}$ and $\boldsymbol{B}$ representing macroscopic electric and magnetic fields. The second term in the RHS is the pressure gradient; the third term represents the momentum exchange between the particles with the collision frequency v_c. The generation of charge particles is not taken into account in equation (9). Two species, electrons and hydrogen ions are considered with q = e for ions (Z = 1) and q = -e for electrons.

In this chapter, uniform non-magnetized plasma will be considered, such that the effect of $\boldsymbol{u}\times\boldsymbol{B}$ term is negligible with respect to $\boldsymbol{E}$ in equation (9). Based on this, the description of the

phenomena such as plasma oscillations, the plasma dielectric constant, the plasma conductivity and skin depth will be provided. The conductivity determines the power dissipation, which is an important parameter for electron heating in discharges.

3.1.1.1 *Dynamics of the non-magnetized plasma*

3.1.1.1.1 Plasma frequency

Consider a plasma slab of a finite width l and having a density $n_e = n_i = n_0$. Here, n_e is the density of cold electron($T_e = 0$), n_i is the ion density and n_0 is the particle density (either electrons or ions). Ions are considered to be stationary due to their infinite mass with respect to electrons. Since $n_e = n_i$ and no other electric field source are present therefore the electric field in the slab will be $\boldsymbol{E} = 0$. Now let the electron slab be displaced by a small distance $x_e(t) \ll l$ at time t , to the right with respect to the slab of ions (see Figure 29 (a)).

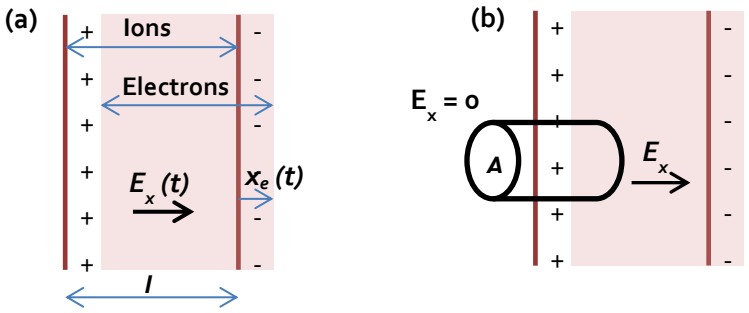

Figure 29: Plasma oscillations in the slab (a) electron cloud displacement with respect to ion cloud; (b) electric field calculation.

Due to the stationary ions, a surface charge density $\rho_s = en_0x_e$ develops at the left edge and similarly $\rho_s = -en_0x_e$ develops at the right edge because of the electrons. Using the integral form of the Gauss' law (equation (10)) applied to the small box shown in Figure 29 (b),

$$\epsilon_0 \oint \boldsymbol{E}.d\boldsymbol{A} = q \tag{10}$$

An electric field can be obtained within the slab:

$$E_x = \frac{en_0x_e}{\epsilon_0} \tag{11}$$

The force equation for the electron in the slab is

$$m\frac{d^2x_e}{dt^2} = -eE_x \tag{12}$$

Here, m is the electron mass. Substituting equation (11) into equation (12), we get

$$\frac{d^2x_e}{dt^2} = -\omega_{pe}^2x_e \tag{13}$$

where,

$$\boldsymbol{\omega_{pe}} = \sqrt{\frac{\boldsymbol{e^2 n_0}}{\boldsymbol{\epsilon_0 m_e}}} \tag{14}$$

is the **electron plasma frequency** [56], that is the fundamental characteristic frequency of a plasma. If the ions also move slightly and the assumption of the infinite mass of the ions is not made then the natural plasma frequency can be expressed as follows:

$$\omega_p^2 = \omega_{pe}^2 + \omega_{pi}^2 \tag{15}$$

where,

$$\boldsymbol{\omega_{pi}} = \sqrt{\frac{\boldsymbol{e^2 n_0}}{\boldsymbol{\epsilon_0 m_{ion}}}} \tag{16}$$

is the **ion plasma frequency** [56] with m_{ion} as the mass of the ion. For $m_{ion} \gg m_e$, $\omega_p \approx \omega_{pe}$.

3.1.1.2 *Plasma complex permittivity and Conductivity*

Consider a uniform plasma with a background gas that is driven by a small amplitude time varying electric field in the x direction:

$$E_x(t) = \widetilde{E_x} \cos \omega t = \mathrm{Re}\, \widetilde{E_x}\, e^{j\omega t} \tag{17}$$

where $\widetilde{E_x}$ is the complex electric field amplitude. For the ease of the calculation, again let the ion mass to be infinite and assuming all quantities to vary sinusoidal in time with frequency ω. Using the isothermal approximation, the changes in pressure are ascribed only to the changes in density [56][66]. Therefore the pressure gradient is given as $\nabla p = k_B T_e \nabla n_e$ (with k_B as the Boltzmann constant) and here the electron density gradient is not significant and thus we can effectively ignore electron thermal energy in equation (9). Since small amplitude time varying electric field is considered this implies a small velocity and thus the quadratic term $(\boldsymbol{u} \cdot \nabla)\boldsymbol{u}$ in equation (9) is negligible. The force equation for the electron becomes:

$$m n_0 \frac{du_x}{dx} = -e n_0 E_x - m n_0 v_c u_x \tag{18}$$

Letting,

$$u_x(t) = \mathrm{Re}\ \widetilde{u_x}\, e^{j\omega t} \tag{19}$$

Substituting equation (17) into equation (18), to obtain the complex velocity amplitude

$$\widetilde{u_x} = -\left(\frac{e}{m}\right)\left(\frac{1}{j\omega + v_c}\right)\widetilde{E_x} \tag{20}$$

The total current is a combination of the displacement current arising from the time – varying electric field and the conduction current due to the electron motion, is given as:

$$J_{T_x} = \epsilon_0 \frac{\partial E_x}{\partial t} + J_x \tag{21}$$

where, J_x is the conduction current due to the electron motion only. Under the cold plasma approximation, i.e $T_e = T_i = 0$,

$$\widetilde{J_x} = -en_0\widetilde{u_x} \tag{22}$$

we also have

$$\frac{\partial E_x}{\partial t} = \mathrm{Re}\, j\omega\widetilde{E_x}\, e^{j\omega t} \tag{23}$$

Now the amplitude of the total current is

$$\widetilde{J_{T_x}} = j\omega\epsilon_0\widetilde{E_x} - en_0\widetilde{u_x} \tag{24}$$

Substituting equation (20) into equation (24)

$$\widetilde{J_{T_x}} = j\omega\epsilon_0\tilde{E}_x + \frac{n_0e^2}{m(j\omega + \nu_c)}\tilde{E}_x = j\omega\epsilon_0\left[1 - \left(\frac{\omega_{pe}^2}{\omega(\omega - j\nu_c)}\right)\right]\widetilde{E_x} \tag{25}$$

Introducing an **effective complex permittivity of plasma** [56] **as:**

$$\epsilon_p(\omega) = \left[1 - \left(\frac{\omega_{pe}^2}{\omega(\omega - j\nu_c)}\right)\right] = 1 - \frac{\omega_{pe}^2}{\omega^2 + \nu_c^2} - i\frac{\nu_c}{\omega}\frac{\omega_{pe}^2}{\omega^2 + \nu_c^2} \tag{26}$$

Plasma conductivity [56] is defined by writing equation (25) in the form $\widetilde{J_x} = (\sigma_p + j\omega\epsilon_0)\widetilde{E_x}$, with

$$\boldsymbol{\sigma_p = \frac{\epsilon_0\omega_{pe}^2}{j\omega + \nu_c} = \epsilon_0\omega_{pe}^2\frac{(\nu_c - i\omega)}{\nu_c^2 + \omega^2}} \tag{27}$$

For low frequencies $\omega \ll \nu_c, \omega_{pe}$, $\sigma_p \rightarrow \sigma_{dc}$, where

$$\boldsymbol{\sigma_{dc} = \frac{\epsilon_0\omega_{pe}^2}{\nu_c} = \frac{e^2n_0}{m\nu_c}} \tag{28}$$

which is the ***dc plasma conductivity*** [56] in the cold plasma approximation.

3.1.1.3 *Power density*

The work done per unit time and unit volume on electrons is $\widetilde{\boldsymbol{J_T}}^* \cdot \tilde{\boldsymbol{E}}$ and by taking its temporal average the power density [56] is obtained as follow:

$$P = \frac{1}{2}\mathrm{Re}\left(\widetilde{J_T}^* \cdot \tilde{E}\right) = \frac{1}{2}\mathrm{Re}\left(\widetilde{J_T} \cdot \tilde{E}^*\right) \tag{29}$$

By substituting $\widetilde{\boldsymbol{J_T}} = (\sigma_p + j\omega\epsilon_0)\tilde{\boldsymbol{E}}$ into equation (29), the collisional power absorbed by the electrons in terms of the electric field amplitude $\tilde{\boldsymbol{E}}$ is given as:

$$P = \frac{1}{2}\left|\tilde{E}\right|^2\epsilon_0\omega_{pe}^2\left(\frac{\nu_c}{\nu_c^2 + \omega^2}\right) \tag{30}$$

This shows the importance of collisions in heating the plasma, if $\frac{\nu_c}{\omega}$ is small then power density is proportional to collision frequency ν_c. In the following sections, it will be shown that not only collisional heating [56] leads to plasma heating but there is also a mechanism called collision-less heating [63] which leads to plasma heating. This mechanism is dominant in low pressure RF discharges.

3.1.1.4 *Plasma Skin depth*

Again considering that the ions do not respond to high frequency perturbation, the dispersion of electromagnetic waves in plasma is equivalent to that in dielectrics, in that one can define a refractive index $n_{ref}^2 = \epsilon_p$. According to [66], given the complex nature of the relative permittivity for plasma, one can set $n_{ref} = n_{real} + in_{imag}$ and comparing with equation (26) gives:

$$n_{real}^2 - n_{imag}^2 = 1 - \frac{\omega_{pe}^2}{\omega^2\left(1 + \frac{\nu_c^2}{\omega^2}\right)} \tag{31}$$

$$2n_{real}n_{imag} = \frac{\nu_c}{\omega}\frac{\omega_{pe}^2}{\omega^2\left(1 + \frac{\nu_c^2}{\omega^2}\right)} \tag{32}$$

There are two frequency domains:

- Above the plasma frequency, $\omega > \omega_{pe}$ (typically in the GHz range), up to pressures of 100 Pa or so, the collision frequency is usually very small compared to the wave frequency, so that $\frac{\nu_c}{\omega} \ll 1$. Then,

  $$n_{imag} \cong 0 \ \ and \ n_{real}^2 \cong 1 - \frac{\omega_{pe}^2}{\omega^2} \tag{33}$$

  The electromagnetic waves propagate in the plasma, which behaves as the dielectric of refractive index $\left(1 - \frac{\omega_{pe}^2}{\omega^2}\right)^{1/2}$. The damping length is very long and the wave propagates with very weak attenuation. This frequency regime typically corresponds to microwaves with which interferometry or reflectometry can be used to determine plasma characteristics.
- At lower frequency, $\omega < \omega_{pe}$, which is typical of the radio frequency domain, the waves decay. Consider a pressure low enough for $\frac{\nu_c}{\omega} \ll 1$. Since $\frac{\omega_{pe}^2}{\omega^2} > 1$, $\mathrm{n_{real}} \to 0$ and $\mathrm{n_{imag}^2} \approx \frac{\omega_{pe}^2}{\omega^2}$. The electron response to the electric field is dominated by the inertial term in the momentum balance. The perturbations are evanescent and diminish with a characteristic scale, the inertial (or collision-less) skin depth is given by

  $$\delta = \frac{c}{\omega\, n_{imag}} = \frac{c}{\omega_{pe}} \tag{34}$$

  In the opposite high pressure limit of $\frac{\nu_c}{\omega} \gg 1$, the response to the electric field is dominated by the collision term that lead to low conductivity (that is high resistivity) and $n_{imag}^2 \approx \omega_{pe}^2/(2\omega\nu_c)$, which leads to

$$\delta = \frac{c}{\omega\, n_{imag}} = \sqrt{\frac{2c^2 v_c}{\omega_{pe}^2}} = \sqrt{\frac{2}{\mu_0 \omega \sigma_P}} \tag{35}$$

which is called the **resistive (or collisional) skin depth** [66].

3.1.2 Model for the estimation of the plasma electron temperature

Consider a cylindrical volume with the radius a and length l as shown in Figure 30, filled with plasma and neutral particles. Assumption of low to intermediate ion mean free path, λ_i [56] regime is made to estimate the plasma electron temperature and its variation with pressure and source geometry. With σ_i as the total ionization cross section, the ion-neutral mean free path is given as

$$\lambda_i = \frac{1}{n_g \sigma_i} \tag{36}$$

For Hydrogen gas at room temperature $\sigma_i \approx 10^{-21} m^2$. Here, n_g is the gas density calculated from the known gas pressure P_{gas} and gas temperature T_{gas} within the plasma volume, and is given as follow

$$n_{gas} = \frac{p_{gas}}{k_B T_{gas}} \tag{37}$$

Here k_B is the Boltzmann constant.

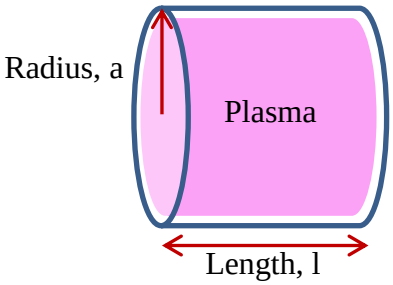

Figure 30: Sketch of plasma radius and length.

In this model, the plasma electron density is considered nearly uniform in the bulk cylindrical plasma, with the density falling sharply near the sheath edges. With this assumption the edge to centre density ratio, h_l and h_a can be calculated [56], and these are given as follows:

$$h_l \approx \frac{0.86}{\sqrt{3 + \frac{l}{2\lambda_i}}} \qquad h_a \approx \frac{0.8}{\sqrt{4 + \frac{a}{2\lambda_i}}} \tag{38}$$

An estimation of the plasma electron temperature within the driver region of the ion source is provided based on the principle of the particle balance equation [38]. In this case, the particle balance equation gives:

$$\frac{K_{iz}(T_e)}{u_B(T_e)} = \frac{1}{n_g d_{eff}} \tag{39}$$

Here, K_{iz} is the ionization rate constant given as [56]

$$K_{iz}(T_e) = \sigma_0 v_{th}\left(1 + \left(\frac{2T_e}{\varepsilon_{iz}}\right)\right)\exp\left(-\frac{\varepsilon_{iz}}{T_e}\right) \tag{40}$$

The formula of K_{iz} found in [66] is different from [56] and gives much lower estimation of electron temperature in comparison with the experimental results when calculated for the different ion sources like ELISE or NIO1. Therefore the used formula of K_{iz} in this model is the one taken from [56] that gives results more in line with the measurements (see section 5.2.1 and 6.2.1). Here, $\sigma_0 = \pi\left(\frac{e}{4\pi\varepsilon_0\varepsilon_{iz}}\right)^2$ with ε_0 as the vacuum permittivity and ε_{iz} as the atomic ionization potential. v_{th} is the thermal electron velocity, $v_{th} = \sqrt{\frac{k_B T_e}{m_e}}$, u_B is the Bohm velocity and is given as;

$$u_B = \sqrt{\frac{k_B T_e}{m_{ion}}} \tag{41}$$

Both K_{iZ} and u_B are the functions of electron temperature. d_{eff} is the effective plasma size.

$$d_{eff} = \frac{1}{2}\frac{al}{ah_l + lh_a} \tag{42}$$

By numerically solving equation (39) one can obtain electron temperature as a function of P_{gas} and T_{gas}.

3.1.3 Plasma heating mechanisms

The power deposition in an inductively coupled plasma source can be described as a decay of cylindrical transverse electric (TE) wave into plasma [59]. The decay length (skin depth) δ can be calculated in terms of the applied frequency ($f = 2\pi/\omega$), plasma density and other parameters. The detailed description of the model and the assumptions involved are given in reference [59]. The power deposition in the plasma depends upon the two main effects:

- Ohmic (collisional) heating
    - Classical skin depth
- Stochastic (collision-less) heating

Here, we will model all these parameters and then use them to calculate the power transfer to the plasma, first with the help of the transformer model and then with the help of the multi-filament model.

3.1.3.1 *Ohmic (collisional) heating*

Ohmic heating is present in all discharges and it is due to the transfer of energy gained from the electrons accelerated by the electric fields into thermal electron energy, through local collisional processes. This is the dominant heating mechanism in the highly collisional limit ($v_m \gg \omega$, here v_m is the total collision frequency for momentum loss) where the nonlocal and kinetic effects are unimportant. Hence, in this limit a fluid (local) approach is used to arrive at an expression for the ohmic power (see reference [59]). Electrons inside plasma can undergo several kinds of collisions with the neutral particles and ions, which leads to momentum and energy transfer between the particles. The collision frequency for a process j can be written as $v_j = n_{target} k_j$, where k_j is the reaction rate for the j-th process and n_{target} is the number density of the target particles. The reaction rate is calculated as the product σ|v| averaged over a Maxwellian distribution function[56][67]:

$$k(T) = <\sigma v>(T) = \sqrt{\frac{8e}{\pi m_e}} \frac{1}{T^{\frac{3}{2}}} \int_0^\infty \sigma(E_n) E_n e^{-\frac{E_n}{T}} dE_n \qquad (43)$$

With E_n defined as the energy of the electrons and T as the electron temperature expressed in eV. For electron collisions with neutrals, n_{target} corresponds to the gas density n_{gas} which is same as described in equation (37).

Ionization is a physical process by means of which an electron is removed from the neutral atom or from a previously ionized ion. A characterization of the ionization level of the plasma can be done in terms of the degree of ionization 'η' defined as follow:

$$\eta = \frac{n_i}{n_i + n_0} \qquad (44)$$

The value of η varies from 0 (non-ionized plasma) to 1 (completely ionized plasma).
The total collision frequency for momentum loss v_m between electrons and the other particles inside the plasma is the sum of three collision frequencies (see reference [67]).

$$v_m = v_{en}^p + v_{en}^{iz} + v_{ei}^p \qquad (45)$$

Where,

- v_{en}^p is the momentum transfer electron neutral collision frequency. It is obtained using the following equation:

$$v_{en}^p(T_e) = n_{gas} k_{en}^p(T_e) \qquad (46)$$

k_{en}^{p} is the reaction rate calculated from momentum transfer electron neutral collision cross section, σ_{en}^{p} taken from reference [68] for hydrogen gas.

- v_{en}^{iz} is the electron neutral ionization collision frequency. It is obtained using the following equation:

$$v_{en}^{iz}(T_e) = n_{gas} k_{en}^{iz}(T_e) \tag{47}$$

k_{en}^{iz} is the reaction rate calculated from electron neutral ionization cross section, σ_{en}^{iz} taken from reference [69] for hydrogen gas.

- v_{ei}^{p} is the electron-ion collision frequency for momentum loss. It is calculated by averaging the Coulomb cross-section over a Maxwellian distribution function, neglecting the ion motion ,

$$< v_{ei}^{p} > = \frac{n_e \frac{4\sqrt{2\pi}}{3} \left(\frac{ze^2}{4\pi\varepsilon_0}\right)^2 \ln \Lambda_e}{\sqrt{m_e (k_B T_e)^3}} \tag{48}$$

Here, $\ln \Lambda_e$ is the Coulomb logarithm evaluated at v_{th} (the thermal velocity of the electron, described in section 3.1.2):

$$\ln \Lambda_e = \ln \left[\frac{4\pi m_{ion}}{e^3 (m_e + m_{ion})} \frac{(\varepsilon_0 k_B T_e)^{\frac{3}{2}}}{n_e^{\frac{1}{2}}} \right] \tag{49}$$

In this hypothesis, we have considered quasi – neutrality condition i.e. $n_{ion} = n_e$.

v_{ei}^{p} increases considerably with the increase in degree of ionization.

MATLAB® scripts have been written to calculate the total momentum loss collision frequency v_m for different plasma parameters like the electron temperature T_e, electron density n_e, gas temperature T_{gas} and pressure P_{gas} .

3.1.3.1.1 Classical skin depth

The calculation presented in the reference [59] shows that the classical skin depth δ depends not only on the frequency (collision frequency 'v_c' and the applied frequency 'ω') and electron density (n_e) but also on the chamber radius a of the ion source (see equation (50)).

$$\delta = \frac{c}{\omega_{p_e}} \left(\frac{2\left[1 + \left(\frac{{v_c}^2}{\omega^2}\right)\right]}{y\left\{1 + \left[1 + \left(\frac{{v_c}^2}{\omega^2 y^2}\right)\right]^{\frac{1}{2}}\right\}} \right)^{\frac{1}{2}} \tag{50}$$

Where, c is the velocity of light, $y = 1 + x\left(1 + \left(\frac{{v_c}^2}{\omega^2}\right)\right)$ and $x = \left(\frac{c}{\omega_{p_e}}\right)^2 \left[\left(\frac{3.83}{a}\right)^2 - \left(\frac{\omega}{c}\right)^2\right]$.

3.1.3.1.1.1 Estimation of the minimum electron density within the ion source

When $a \gg \frac{c}{\omega_{pe}}$, the geometrical effects in the skin depth, i.e., the dependence on the source chamber radius, can be neglected since x<<1 and y~1. Considering this assumption, a relation between the electron density and the chamber radius is worked out in order to find possible value of the minimum electron density within the plasma chamber.

$$n_e \gg \frac{\epsilon_0 c^2 m_e}{e^2 a^2} \tag{51}$$

For the case of $a = 3.83\frac{c}{\omega_{pe}}$, the finite radial effects can be important in calculating the skin depth for compact geometries. In addition, considering the finiteness of the plasma within the chamber, it was also discovered that the geometrical affect can be important [70]. We will see in the application of the developed methodology that these effects are important for the smaller source like NIO1 (see section 6.4), while are negligible for the relatively bigger ion source like ELISE (see section 5.5).

MATLAB® code is written to evaluate the skin depth δ based on the expression provided in equation (50).

3.1.3.2 *Stochastic (Collision less) heating*

A spatially non uniform electric field $\boldsymbol{E}$ by itself might lead to electron heating, provided that the electrons have thermal velocities sufficient to sample the field inhomogeneity during the RF period. This phenomenon is called collision-less, stochastic or nonlocal heating and was first developed by Landau [63]. This effect is important in the low-pressure limit. The collision-less electron heating is a warm plasma effect because in cold collision-less plasma (where $T_e = 0$) each electron samples the electric field $\boldsymbol{E}$ at a single location in space, and since the field has a harmonic time variation it averages to zero everywhere, so no energy can be gained. However, if the electrons are in thermal motion as in the warm plasma, they sample the field along some trajectory and in general the field does not average to zero along a trajectory [64]. The $\boldsymbol{E}$ field is confined to the skin depth layer, δ, so if an electron can traverse the skin depth layer in a time that is short compared to the period of the field, then it will gain net energy from the field (see reference [64]). This situation arises when

$$\omega\delta_a \leq \left(\frac{k_b T_e}{m_e}\right)^{\frac{1}{2}} \tag{52}$$

The skin depth in this case is defined as:

$$\delta_a = \left[\left(\frac{2k_bT_e}{\pi m_e}\right)^{\frac{1}{2}} \frac{c^2}{\omega_{pe}^2 \omega}\right]^{1/3} \tag{53}$$

The assumption that the plasma is half infinite is valid when

$$\delta_a \leq L \tag{54}$$

where, L is the distance between the two infinite plane walls where the plasma is enclosed.

3.1.3.2.1 Identification of the region for the onset of stochastic heating

For a plasma of fixed size, density, and temperature, there is a finite range of frequencies that allows effective collision-less excitation. Combining the above inequalities (equations (52) – (54)), implies that, for plasma of fixed size and temperature, there is a threshold plasma density below which collision-less excitation is not possible at all [64]. It can be shown that the threshold density depends only on L:

$$n_e^{threshold} \approx \left(\frac{2}{\pi}\right)^{\frac{1}{2}} \frac{c^2 \varepsilon_0 m_e}{L^2 e^2} \tag{55}$$

While the corresponding excitation angular frequency is

$$\omega^{threshold} \approx \frac{1}{L}\left(\frac{k_bT_e}{m_e}\right)^{\frac{1}{2}} \tag{56}$$

Based on the equations (55) – (56), MATLAB® code has been written to identify the region where collision - less heating becomes effective.

3.1.3.2.2 Calculation of stochastic heating collision frequency

A model to describe the stochastic heating phenomena is presented in [59]. In this model, only electron inertia is considered. The applied frequency is assumed to be higher than the ion plasma frequency; so that ions do not respond to the RF fields i.e. the ion plasma frequency is much smaller than the excitation frequency. Based on this assumption a stochastic collision frequency ν_{stoc} is defined and identified by solving a set of equations involving a parameter called α and the penetration depth δ as a function of ν_{stoc} (neglecting the geometric effects in the equation (50), ν_c is replaced by ν_{stoc}, see equation (57)).

$$\delta = \frac{c}{\omega_{p_e}} \left(\frac{2\left[1 + \left(\frac{{\nu_{stoc}}^2}{\omega^2}\right)\right]}{y\left\{1 + \left[1 + \left(\frac{{\nu_{stoc}}^2}{\omega^2 y^2}\right)\right]^{\frac{1}{2}}\right\}} \right)^{\frac{1}{2}} \tag{57}$$

Where, $y = 1 + x\left(1 + \left(\frac{{\nu_{stoc}}^2}{\omega^2}\right)\right)$ and $x = \left(\frac{c}{\omega_{p_e}}\right)^2 \left[\left(\frac{3.83}{a}\right)^2 - \left(\frac{\omega}{c}\right)^2\right]$.

The parameter α is defined (see reference [59]) as:

$$\alpha = \frac{4\delta^2\omega^2}{\pi v_{th}^2} \propto \left(\frac{transit\ time\ through\ \delta}{rf period}\right)^2 \quad (58)$$

Here v_{th} is calculated as mentioned in section (3.1.2). It can be shown after the integration on the whole plasma volume that the power per unit surface absorbed by the plasma is

$$P_{plasma} = \frac{e^2 E_0^2 n_e \delta}{4m_e} \frac{4\delta}{v_{th}} \mathcal{J}(\alpha) \quad (59)$$

Where $\mathcal{J}(\alpha)$ is defined as

$$\mathcal{J}(\alpha) = \frac{1}{\pi}(e^{\alpha}(1+\alpha)\int_{\alpha}^{\infty}\left(\frac{e^{-x}}{x}dx\right) - 1) \quad (60)$$

The power deposition in the case of collision-less heating can be defined as;

$$P_{plasma} = \frac{e^2 E_0^2 n_e \delta}{4m_e} \frac{v_{stoc}}{v_{stoc}^2 + \omega^2} \quad (61)$$

Equating equation (61) with equation (59), one can obtain:

$$\frac{4\delta}{v_{th}} \mathcal{J}(\alpha) = \frac{v_{stoc}}{v_{stoc}^2 + \omega^2} \quad (62)$$

The solution of the stochastic collision frequency v_{stoc} [59] is obtained by numerically solving different set of equations involving α, δ and v_{stoc} equation (57), (58) and (60). The first step is to provide solution of equation (60) for different ranges of α [59]. This is given as follow:

$$\mathcal{J}(\alpha) \approx \begin{cases} \frac{\pi}{2} & 10^{-4} \leq \alpha \leq 0.03 \\ \frac{1}{8\pi\alpha} & 0.03 \leq \alpha \leq 10 \\ \frac{1}{\pi\alpha^2} & 10 \leq \alpha \end{cases} \quad (63)$$

To derive the solution for stochastic collision frequency v_{stoc} , the solution of $\mathcal{J}(\alpha)$ expressed in equation (63) is combined with equation (62). The following analytical solution [59] is obtained:

Case 1 – when $\alpha \ll 1$ then,

$$v_{stoc} = \frac{1}{2\pi}\left(\frac{v_{th}}{\delta}\right) \quad (64)$$

Case 2 – when $\alpha \sim 1$ then

$$v_{stoc} = \frac{1}{4}\left(\frac{v_{th}}{\delta}\right) \quad (65)$$

Case 2 – when $\alpha \gg 1$ then

$$v_{stoc} = \frac{\pi}{4\omega^2}\left(\frac{v_{th}}{\delta}\right)^3 \quad (66)$$

Again a MATLAB® code is written to solve the above equations. As a first step δ in equation (57) is obtained from ohmic heating collision frequency v_m. Then this δ is used in

equations (64)-(66) to obtain stochastic collision frequency, v_{stoc}. Since v_{stoc} is solved for ranges of $\alpha \ll 1$ and $\alpha \gg 1$ therefore a kink or a discontinuity is observed in the results obtained in Chapter 5 and Chapter 6. Thus, the resulting curves are connected with the dashed lines in the plots covering the $\alpha \approx 1$ range.

3.2 Effective collision frequency and effective skin depth

To take into account both the heating mechanisms, ohmic (see section 3.1.3.1) and stochastic (see section 3.1.3.2) heating, the total effective collision frequency v_{eff} has been defined [56], [59], [71], [72] as the sum of the momentum loss collision frequency v_m and the stochastic heating collision frequency v_{stoc}.

$$v_{eff} = v_m + v_{stoc} \tag{67}$$

From this effective collision frequency v_{eff}, the skin depth δ defined in equation (50) takes the following form:

$$\delta = \frac{c}{\omega_{p_e}} \left(\frac{2\left[1 + \left(\frac{{v_{eff}}^2}{\omega^2}\right)\right]}{y\left\{1 + \left[1 + \left(\frac{{v_{eff}}^2}{\omega^2 y^2}\right)\right]^{\frac{1}{2}}\right\}} \right)^{\frac{1}{2}} \tag{68}$$

Where, $y = 1 + x\left(1 + \left(\frac{{v_{eff}}^2}{\omega^2}\right)\right)$ and $x = \left(\frac{c}{\omega_{p_e}}\right)^2 \left[\left(\frac{3.83}{a}\right)^2 - \left(\frac{\omega}{c}\right)^2\right]$.

All the parameters described, modelled and evaluated in section (3.1) and (3.2) will be used in section (3.3) and will help in calculating the power transfer to the plasma.

3.3 Power transfer to the plasma – electrical model

3.3.1 Description and plasma electrical parameters

The classical approach described in [56] to model the plasma and its coupling with the RF coil is implemented in this section. As a first step towards the modelling a simplified driver is considered as shown in Figure 31, without the faraday shield and the surrounding metallic structures.

The electric (in the azimuthal direction) and the magnetic field (in the axial direction) induced by the RF coil acts with collisional and the collision-less mechanism to heat the plasma. The previous sections describe these heating mechanisms and lead to the identification of an equivalent region with thickness δ where the power is deposited in the plasma. To set up an electrical model of this region its geometrical extension and electrical

conductance needs to be defined, as described in the following. The geometrical dimension of the plasma-current sheet generated is described by the radial position of the end of the skin depth layer, called plasma radius in the Figure 31, the RF coil length and the skin depth δ.

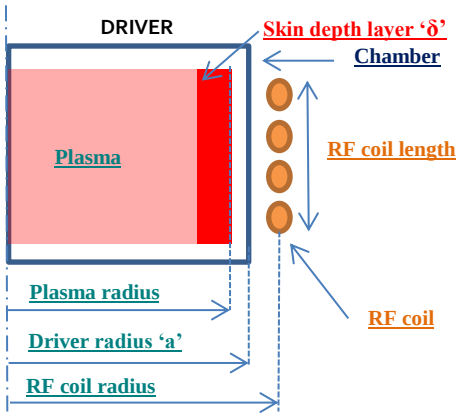

Figure 31: Schematic of the plasma within the driver region.

In the high density regime, this skin depth δ is smaller than the driver radius a (see section 3.1.3.1). In the skin depth layer, the electron density and electron temperature are assumed to be uniform. The inductive coupling mechanism can be described by calling j the current density at the driver radius a: in this way the plasma current I_P and the voltage V_P across the plasma loop are:

$$I_P = j\delta l = \sigma_P E_\theta \delta l \tag{69}$$

$$V_P = 2\pi a E_\theta \tag{70}$$

here, E_θ is the electric field at the driver radius a and σ_P is the plasma conductivity (see section 3.1.1.2 equation (27)) and l is the coil length. Combing these two equations, the plasma resistance R_P and the inductance L_P takes the following form:

$$V_P = \frac{2\pi a}{\delta l} \frac{(\nu_{eff} + i\omega)}{\varepsilon_0 \omega_{pe}^2} I_P \tag{71}$$

$$R_P = \frac{2\pi a}{\delta l \sigma_{dc}} \tag{72}$$

$$L_P = \frac{R_P}{\nu_{eff}} \tag{73}$$

here σ_{dc} is the dc plasma conductivity as defined in equation (28).

3.3.2 Transformer model

The electrical parameters R_P and L_P, along with the transformer model of an inductive discharge which has been proposed by Piejak et al. [57], are used to evaluate the power transfer to the plasma and eventually the estimation of the power transfer efficiency. In this model, the driver including the plasma are regarded as air core transformer with the plasma as a one turn secondary and the RF coil at the primary side. In Figure 32, the equivalent circuit of the driver is shown.

The classical model does not consider the surrounding metallic structure. On the contrary, in the transformer model presented here an equivalent resistance R_{cp} is assumed which takes into account both the coil and the metallic structure.

3.3.2.1 *Inductance calculation*

The mutual inductance L_{12} between the coil and the plasma, self-inductance of the current sheet in the plasma L_{22} and the self-inductance of the coil $L_{11}$are calculated from geometrical plasma/coil dimensions (radius and length) and the relative positions. These formulas are taken from [73] and are described below.

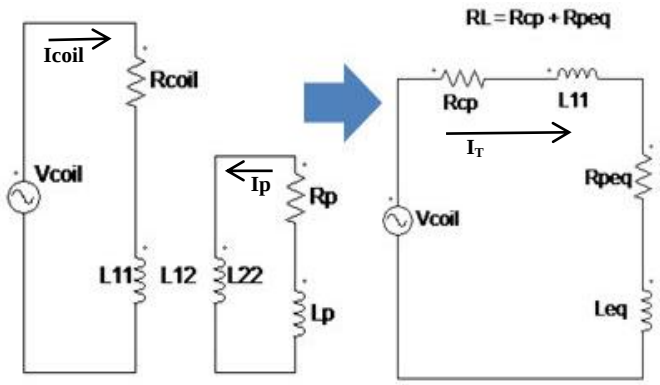

Figure 32: Equivalent electric scheme of the driver (Transformer Model).

The self-inductance of the coil (L_{11}) is given by:

$$L_{11} = 0.002\pi(D_w \times 100)\,(N^2)\left[\ln\left(\frac{4D_w}{l}\right) - \frac{1}{2}\right] \times 10^{-6} \quad [H] \qquad (74)$$

Here D_w is the winding diameter of the coil in meters, $D_w = 2b$ with b as the coil radius, l is the effective axial length of the coil in meters.

The self-inductance of the current sheet in the plasma (L_{22}) is given by:

$$L_{22} = 0.002\pi(D_P \times 100)\left[\ln\left(\frac{4D_P}{L}\right) - \frac{1}{2}\right] \times 10^{-6} \quad [H] \qquad (75)$$

Here, L is the discharge chamber length in meters and D_P is the plasma winding diameter in meter. The plasma winding diameter D_P is not clearly defined as plasma has no defined shape and therefore it is difficult to estimate. Hence as a first approximation, the chamber radius and length are taken as the plasma radius and length and then later they are varied to see the effect on the results obtained.

The mutual inductance L_{12} is calculated considering the magnetic flux through the coil due to the plasma current, yielding:

$$L_{12} = 0.0095N \frac{(D_P \times 100)^2}{\sqrt{(D_w \times 100)^2 + (l \times 100)^2}} \times 10^{-6} \quad [H] \tag{76}$$

Considering harmonic fields, the electrical equations for this transformer becomes:

$$\tilde{V}_{coil} = (R_{coil} + i\omega L_{11})\tilde{I}_{coil} + i\omega L_{12}\tilde{I}_P \tag{77}$$

$$\tilde{V}_P = i\omega L_{21}\tilde{I}_{coil} + i\omega L_{22}\tilde{I}_P \tag{78}$$

where, $\tilde{V}_{coil}$ and $\tilde{I}_{coil}$ are the voltage and current across the coil and $\tilde{I}_P$ is the current flowing in the plasma.

3.3.2.2 *Coil resistance*

Consider a solenoidal coil with a major radius r (i.e. the winding radius) and the minor radius r_w (i.e. the coil wire radius).The electrical resistance of the coil R_{coil} is a frequency dependent parameter and its calculation is defined as follows:

The effective area A of the coil for electrical calculation can be approximated by:

$$\mathrm{A} = 2\pi \mathrm{r_w} \delta_{\mathrm{coil}} \tag{79}$$

$$\delta_{coil} = \sqrt{\frac{2}{\mu_0 \omega \sigma_{coil}}} \tag{80}$$

Where σ_{coil} is the conductivity of the coil wire. The R_{coil} is given as:

$$R_{coil} = \frac{l}{\sigma_{coil} A} = \frac{l}{2\pi\sigma_{coil} r_w} \sqrt{\frac{\mu_0 \omega \sigma_{coil}}{2}} \tag{81}$$

$$R_{coil} \propto \sqrt{\omega} \tag{82}$$

If the coil resistance (= R_{coil0}) at a particular frequency f_0 is available from experimental data for the RF coil of the ion source, then the value of coil resistance R_{coil} at other frequencies can be calculated using the proportionality relation given in equation (82). So, R_{coil} becomes as follow:

$$R_{coil} = R_{coil0} \sqrt{\frac{f}{f_0}} \tag{83}$$

In my transformer model, I assumed an equivalent resistance R_{cp} accounting for the coil and the passive metallic structure and whose behaviour with the frequency is assumed to be similar to the coil resistance expressed in equation (83). The value of R_{cp0} is the assumed value chosen on the basis of the expected or measured value.

3.3.2.3 *Load Impedance*

By using the above equations one obtains:

$$\tilde{I}_P = -\frac{i\omega L_{12}}{i\omega(L_{22}+L_P)+R_P}\, I_{coil} \tag{84}$$

An expression for the load impedance $Z_L = R_L + i\omega L_L$ seen at the primary side of the transformer can be obtained as:

$$Z_L = \left[R_{cp} + \frac{\omega^2 R_P L_{12}^2}{R_P^2+\omega^2(L_{22}+L_P)^2}\right] + i\omega\left[L_{11} - \frac{\omega^2(L_{22}+L_P)L_{12}^2}{R_P^2+\omega^2(L_{22}+L_P)^2}\right] \tag{85}$$

here R_L is the load resistance given as:

$$R_L = R_{cp} + \frac{\omega^2 R_P L_{12}^2}{R_P^2+\omega^2(L_{22}+L_P)^2} = R_{cp} + R_{peq} \tag{86}$$

and L_L is the load inductance given as:

$$L_L = L_{11} - \frac{\omega^2(L_{22}+L_P)L_{12}^2}{R_P^2+\omega^2(L_{22}+L_P)^2} \tag{87}$$

R_{peq} is the plasma equivalent resistance and show the dependence on the applied frequency $\omega = 2\pi f$.

3.3.2.4 *Power transfer efficiency in pure inductive discharges*

The power absorbed by the plasma can be calculated as

$$P_{abs} = \frac{1}{2}\left(R_L - R_{cp}\right)I_P^2 \tag{88}$$

The total input power is given by

$$P_{in} = \frac{1}{2}R_L I_{coil}^2 \tag{89}$$

The power transfer efficiency ξ [67] can be calculated as the ratio between the power absorbed by the plasma P_{abs} and the total input power P_{in} [56] and is given as

$$\xi = \frac{P_{abs}}{P_{in}} = \frac{R_P}{R_L}\frac{\omega^2 L_{12}^2}{\omega^2(L_{22}+L_P)^2 + R_P^2} \tag{90}$$

Note that ξ depends only on frequency, the plasma and coil parameters and the gas density (through the collision frequency), not on the input power or voltage, nor on the value of the matching capacitors. MATLAB® code is written in order to calculate the power transfer efficiency of the plasma.

3.3.3 Multi-filament model

In order to apply the methodology presented in the following, the driver should feature geometrical axis symmetry of its conducting parts including the passive structure and plasma. The approach is to transform the original 3D electromagnetic problem into a simplified 2D axisymmetric problem to be solved in harmonic regime and quasi magneto-static approximation. As for the transformer model, capacitive coupling [56] between the parts is considered negligible also in this approximation.

It has been chosen to analyse the 2D problem with the equivalent circuital model approach, described in the following, in order to provide a logical extension of the concept already presented in the previous transformer model approach.

In the 2D model, each cross section of the driver conductor is divided into M user-defined layers and N user-defined current filaments (see Figure 33). The conductor can be of any shape and size, here in Figure 33 a conductor of square cross-sectioned is shown.

The model can be further simplified by considering that the current in the conductors (passive metallic conductors and plasma) at the frequency of interest for this study is significant only on the surface due to the skin effect. In this view the approach is to consider filaments only on the surface and assign to them an effective area calculated considering the geometrical extension of the filament along the surface and the skin depth at the assigned frequency. In Figure 34 an example of the 2D representation of the multi-filament model for NIO1 ion source with RF coil, plasma and passive metallic structure is shown. Each of these filaments represents a ring of material whose electric properties are described by a resistance R_i, inductance L_i and mutual inductance M_{ij} with all the other current filaments.

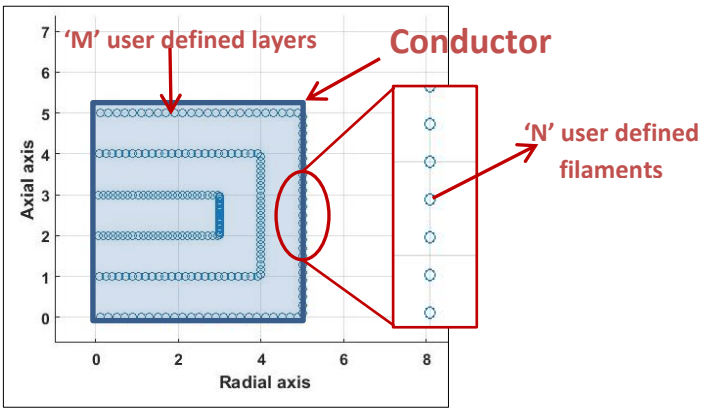

Figure 33: 'M' user defined layers and 'N' user defined filaments over the cross-section of the conductor.

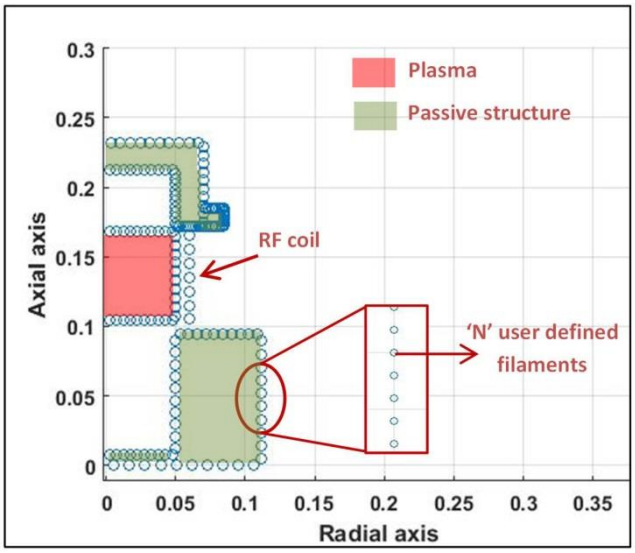

Figure 34: Representation of the 2D multi-filament model with 'N' user defined current filaments for the driver of NIO1 ion source.

The electrical equations to solve the problem resemble the set of equations of multiple mutually-coupled inductors, with usual sign convention for passive components, in harmonic regime at the frequency $\omega = 2\pi f$ and can be written as follow:

$$\begin{aligned} U_1 &= (R_1 + j\omega L_1)I_1 + j\omega M_{12}I_2 + j\omega M_{13}I_3 + \cdots + j\omega M_{1N}I_N \\ U_2 &= j\omega M_{21}I_1 + (R_2 + j\omega L_2)I_2 + j\omega M_{23}I_3 + \cdots + j\omega M_{2N}I_N \\ &\vdots \qquad\qquad \ddots \qquad\qquad \ddots \qquad\qquad \vdots \\ U_N &= j\omega M_{N1}I_1 + j\omega M_{N2}I_2 + j\omega M_{N3}I_3 + \cdots + (R_N + j\omega L_N)I_N \end{aligned} \tag{91}$$

Here, the filament resistance R_i and self-inductance L_i is given as:

$$R_i = \frac{\rho_i 2\pi r_i}{A_{i_{eff}}} \qquad\qquad L_i = \mu_0 r_i \log\left(\frac{8r_i}{a} - 2\right) \tag{92}$$

A_{ieff} is the effective area of current filament, μ_0 is the magnetic permeability of vacuum and ρ_i is the resistivity of each filament. M_{ij} is the mutual inductance between the two filaments at radius r_i, r_j and at the distance d_{ij} and it is defined as follow [74][75]:

$$M_{ij}(m) = 2\mu\left(\frac{\sqrt{r_i r_j}}{m}\right)\left[\left(1 - \frac{m^2}{2}\right)K(m) - E(m)\right] \tag{93}$$

Where,

$$m = \sqrt{\frac{4r_i r_j}{(r_i + r_j)^2 + {d_{ij}}^2}} \tag{94}$$

Here, K and E are elliptical integrals of m. For the estimation of filament resistance, in case of plasma, the same complex electrical conductivity σ_{el} is used as described by equation (27). Each turn of the RF coil is described as a single filament (with relative $U_i = \frac{V_{coil}}{number\ of\ turns\ in\ coil}$) and the same current is imposed on each of them. In particular, it is worth noting that the filaments representing the plasma and the passive structures are closed in short circuit and the relative U_i is set to zero.

3.3.3.1 *Output of the model - Power transfer efficiency*

By assuming a known value for the impressed current I_{coil} in the RF coil filaments, the currents I_P in the plasma and passive structure filaments can be calculated. From these currents and calculated resistances, the power dissipated in each filament, thus the power in the plasma P_{plasma} and passive structures P_{ps} can be obtained. The power transfer efficiency ξ in this case is given as:

$$PTE = \frac{P_{plasma}}{P_{total}} = \frac{P_{plasma}}{P_{coil} + P_{plasma} + P_{ps}} \tag{95}$$

With the known coil current I_{coil}, the plasma equivalent resistance R_{peq} and the passive structure resistance $R_{eq_{ps}}$ at the coil side are given as:

$$R_{eq_{plasma}} = \frac{P_{plasma}}{I_{coil}^2} \qquad R_{eq_{ps}} = \frac{P_{ps}}{I_{coil}^2} \tag{96}$$

From the calculated values of the current, the magnetic field can also be calculated and the magnetic field lines within the driver will also be represented along with the results.

Chapter 4.

Methodology on the estimation of power transfer efficiency

A methodology is developed and presented in this chapter which gives an estimation of the plasma equivalent electrical parameters and the power transfer efficiency to the plasma in an inductively coupled radio frequency ion source. It is the collection of the analytical expressions for different mechanisms like ohmic heating, stochastic heating and an electrical model like the transformer or the multi-filament model for the estimation of power deposition in the plasma. All these mechanisms and models are described in detail in Chapter 3. These mechanisms are then integrated and modelled in a MATLAB® code using the plasma parameters (like n_e, T_e and P_{gas}) as independent quantities (not related to each other) and therefore this model is not self – consistent in this regard.

4.1 Description of the methodology

Figure 35 represents the flow chart of the methodology. The first step is to choose an IC RF ion source of a given geometry, gas type (H_2, Ar etc.) and pressure P_{gas}, and plasma parameters like electron density n_e. From these parameters, an estimation of electron temperature T_e (see section 3.1.2) inside the driver is done (step (a.1) in Figure 35). All these parameters along with the electron temperature are then used as input parameters for the developed MATLAB® code (step (a) in Figure 35). The next step is to identify the parameters involved in describing the analytical model (see section 3.1) of the power transfer in the plasma. The region highlighted in light green in Figure 35 corresponds to this analytical model and it consist of step (b), (c) and (d). Step (b) is involved in the calculation of the ohmic heating collision frequency (see section 3.1.3.1) while step (c) is involved in calculation of skin depth δ (see section 3.1.3.1.1) from this ohmic heating collision frequency. Here, the skin depth can be calculated with or without the geometric effects present in equation (50). In step (d), the calculated skin depth is used as an input to calculate the parameter α (see section 3.1.3.2) based on which the stochastic heating collision frequency (see section 3.1.3.2.2) is estimated.

Either step (b) or step (d) or the sum of both step (b) and (d) leads to the calculation of the effective collision frequency v_{eff} (see section 3.2) in step (e). Based on this effective collision

frequency, the effective skin depth is calculated in step (f). This is the very crucial step as the results for skin depth obtained from this step helps in choosing the valid range of the working frequency applicable for the rest of the calculations.

The next phase is to integrate an electrical model for the power transfer to the plasma with the analytical model. The electrical model is shown with the light peach coloured box in Figure 35 and consists of step (g) and (h).The resulted skin depth from step (f) leads to the calculation of plasma electrical conductivity (see section 3.1.1.2) in step (g) of Figure 35. Two electrical models (see section 3.3) have been described in Chapter 3 and are responsible for the power transfer to the plasma. They are the transformer (see section 3.3.2) and the multifilament (see section 3.3.3) model, forming the step (h) of the methodology in Figure 35. As a first approach a transformer model has been developed; with respect to the classical one [57], it takes into account the presence of passive metallic structures, but considering them as a whole with the coil. Then an improved approach is presented based on the multi-filament model. This model accounts for the electrical coupling among the RF coil, the plasma and the passive metallic structure. The later takes into account the more realistic experimental set up in the methodology. After step (f) and step (g) of the methodology one can either choose the transformer model or the multi-filament model as the step (h) which prepares all the ingredients for the step (i).

The ultimate goal of the developed methodology, i.e., the evaluation of the plasma electrical parameters (plasma equivalent resistance in particular) and the power transfer efficiency is achieved in the last phase of the methodology. This is comprises of the step (i) and (j) in Figure 35 .

The outcome of the methodology can be analysed in various directions depending on the interest of the researcher. In this thesis, the developed methodology is applied to the ELISE and the NIO1 ion source. A comparison between transformer and multi-filament model has been made for both cases. The results of the methodology in terms of the plasma equivalent resistance and the power transfer efficiency have been analysed with respect to the applied frequency, electron density and gas pressure. All the above processes have led to some interesting findings which are reported in the next two chapters

.

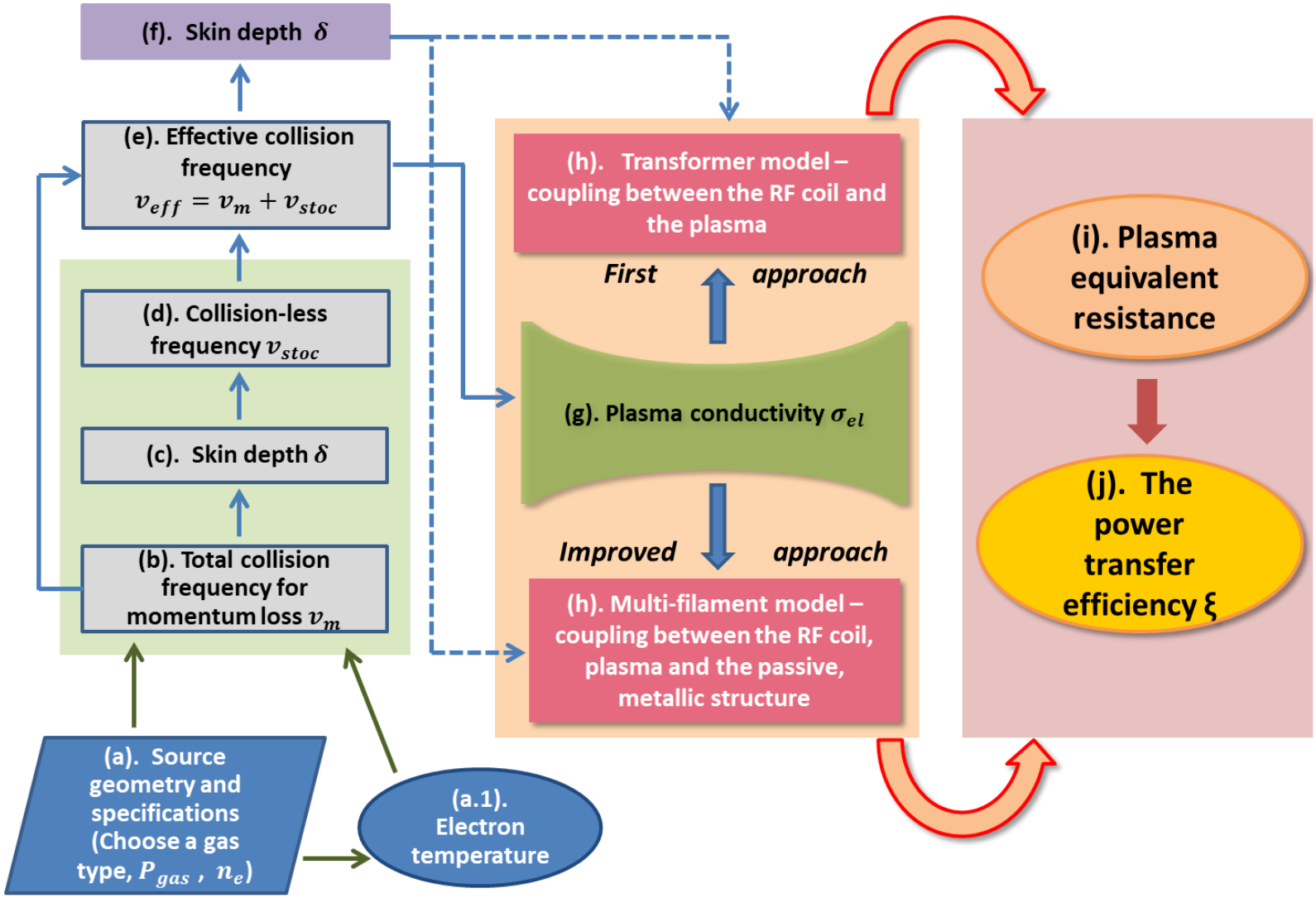

Figure 35: Methodology to calculate the power transfer efficiency in an IC RF ion source.

Chapter 5.

Application to the simplified driver of the ELISE ion source

In this chapter the methodology described in Chapter 4, with the transformer (see section 3.3.2) and the multi-filament (see section 3.3.3) model is applied to a simplified driver of the ELISE ion source with the maximum RF power of 90 kW per driver [53], operating with Hydrogen gas. In the first case, with the application of the transformer model, the faraday shield and the surrounding metallic structures in the driver of the ion source are not taken into account and a simplified driver of the ELISE ion source is considered. In the latter case, with the application of the multi-filament model, the surrounding metallic structures present in the driver are also considered.

The following sections will describe the driver and the input parameters taken for this ion source along with the calculation of the ohmic and stochastic heating collision frequencies. Identification of ranges of electron density and operating frequency for parametric scans will also be shown based on the calculation of the effective skin depth. The significance of the geometric effects will be highlighted during the calculation of the effective skin depth. Eventually, the results focusing on the plasma equivalent resistance and power transfer efficiency will be presented and compared for both models.

5.1 Description of the Driver

An overview of the driver for ELISE is shown in Figure 36. The driver consists of a cylinder made of Al_2O_3 [32] with an outer diameter of $300\ mm$, a wall thickness of $8\ mm$ and a length of $140\ mm$. This cylinder is in no direct contact with the metal flanges but floating between two O rings which protect the driver from mechanical damage. The back side of the driver is closed with the driver back plate which is supported by four rods from the driver plate. It is made from aluminium and equipped with a cooling loop and inside a pattern of permanent magnets ($9\ mm \times 13\ mm$) in a chequer board configuration. The RF coil with 6 windings is wound around the driver cylinder. The driver inner part is protected against erosion by an actively cooled Faraday shield whose thin walled structure was manufactured completely by electro deposition of copper. It consists of a back plate with two layers of spider like manifolds on top of each other, one acting as the water inlet and one as outlet manifold. They are

connected to the cylindrical side wall (only $3\ \mu m$ thick) where they feed always four stripes with cooling water. All inner surfaces of the Faraday shield are coated again with $3\ \mu m$ of Mo to prevent Cu sputtering. Each driver is also shielded with an electro-magnetic shield made of $4\ mm$ thick copper material (see Figure 27).

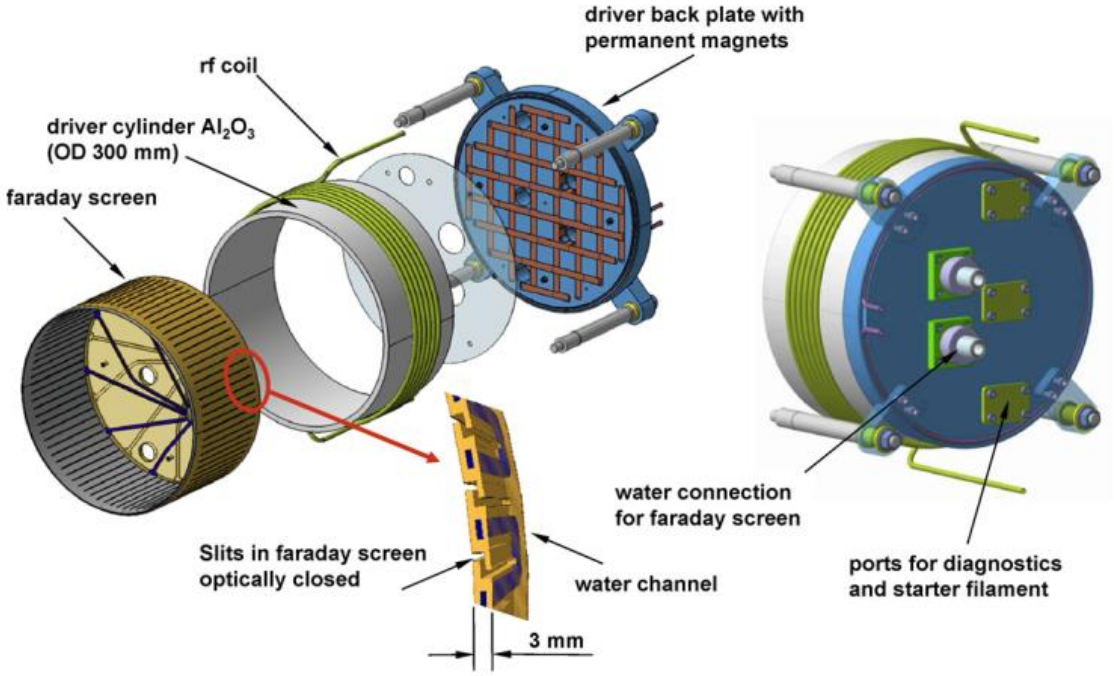

Figure 36: Design of the ELISE driver, right side complete assembly, left side exploded view from inside [32].

5.2 Input parameters

ELISE (Extraction from a Large Ion Source Experiment) ion source is described in section 2.5.1. ELISE test facility comprises 4 RF drivers - with two drivers in series, see Figure 27. For this study, only one simplified driver is considered. The design of the single driver of ELISE is shown in Figure 36. The geometrical parameters and typical plasma quantities (seen during the operation) for the ELISE driver region are listed in Table 6. Some of the geometrical parameters are taken from [32] and others are taken from the CAD drawings of the ELISE driver. These CAD drawings are shown in the Appendix.

It should be noted that some elements (like Cu, Mo) might be present in the ion source during the operation due to the sputtering or a leak [25]. As for the caesium its density is of the order of $\sim 10^{15}\ m^{-3}$ near the plasma grid [24] and is expected to be even lower within the driver region. The presence of these elements is very limited within the driver and their effect is neglected in this work.

Table 6: Geometrical and operative parameters for a simplified driver of ELISE

Geometrical parameters	Value
Driver case (Al_2O_3 or quartz)	
Inner Radius [cm]	14
Outer Radius [cm]	15
Length [cm]	14
RF coil (copper)*	
Number of turns	6
Radius [cm]	15.8
Solenoid coil length[cm]	8
Wire radius [cm]	0.4
Driver back plate (Aluminium)	
Radius [cm]	15
Thickness [cm]	3
Faraday shield (Copper)	
Back plate radius [cm]	14.1
Back plate thickness [cm]	1
Source back plate (Stainless Steel)*	
Inner radius [cm]	15
Outer radius [cm]	20.2
Thickness [cm]	4
Electromagnetic shield (copper)	
Inner radius [cm]	19.8
Outer radius [cm]	20.2
Length [cm]	14
Plasma quantities	
Electron density, n_e [m^{-3}][a]	~ 10^{18}
Electron temperature , T_e [eV][a]	5 - 30
Gas Pressure, P_{gas} [Pa][b]	Variable up to 1 Pa
Gas temperature, T_g [K][b]	1200-1500

Note - * is only a geometrical parameter for the simulation considered in this thesis, it is not the real " ELISE parameter". It is chosen on the basis of the assumption that the boundary of the source back plate for a single driver of ELISE is up to the outer radius of the electromagnetic shield.

[a] and [b] are reported in [76] and [77]

5.2.1 Estimation of the electron temperature

To estimate the electron temperature inside the driver, it is necessary to know the gas temperature and pressure (see section 3.1.2). Experimental measurements for the ELISE ion source have shown that the gas temperature is dependent on the gas flow and the applied RF power [77]. The gas pressure inside the driver of the ion source (BATMAN [33]) similar to the single driver of ELISE lies between 0.3 - 1 Pa and correspondingly the gas temperature lies between $900\,K \pm 1500\,K$ [33]. Considering these findings, a wider range of 0.1 – 1 Pa and 800K – 1600K is chosen for gas pressure P_{gas} and temperature T_{gas} to numerically calculate the electron temperature T_e. The results are shown in Figure 37 . It can be seen that T_e decreases

with the increase in pressure P_{gas} for all the gas temperatures T_{gas}. The same trend is also observed in other IC RF ion source of similar type [78].

It is shown in [76], that the electron temperature varies from $5 - 30\ eV$ at 0.3 Pa for the power range of 40-80 kW. In [79], it has been shown experimentally that at a gas pressure of 0.6 Pa, the electron temperature T_e~$8\ eV$ is found in the driver region of the IPP type ion source. In Figure 37, an electron temperature close to 7 eV is obtained numerically for gas temperature in the range of (1400 – 1600) K (this temperature range is little different from the one reported in Table 6). The small discrepancy between the two results occurs because the experimental results are sensitive to the gas temperature and the applied power. However, the same T_e has been estimated in the ELISE like ion source presented in [78], where the T_e~$7\ eV$ for the power of 50 kW and at 0.6 Pa, thus providing the validation of the calculation presented in Figure 37. Hence, the estimated value of $9\ eV$ for the electron temperature at 0.3 Pa and $1200 - 1500\ K$ gas temperature, seems reasonable and is chosen as an input parameter for the further analysis in this work.

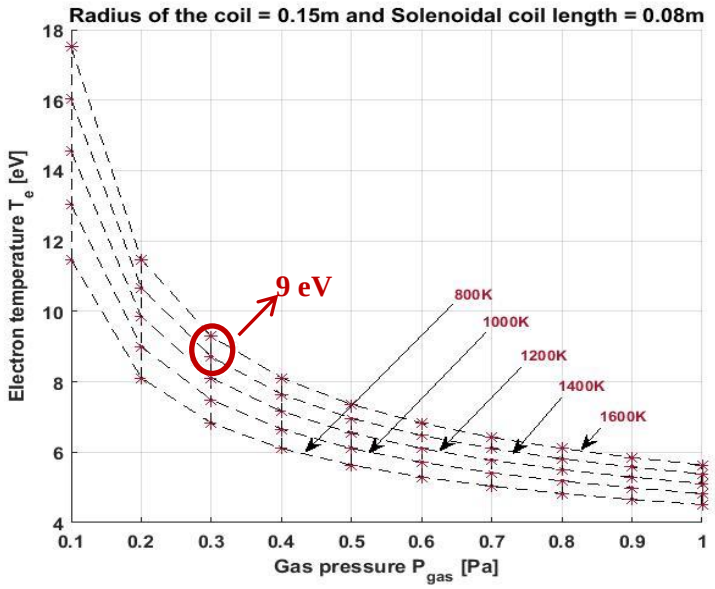

Figure 37: Estimation of electron temperature (for different values of gas temperature) with gas pressure for the driver of ELISE ion source.

5.2.2 Electron density range

I limit the maximum electron density for my analyses to be one order of magnitude higher than the experimental operating electron density (10^{18} m^{-3}) [76] seen for the ELISE driver. As far as the minimum electron density is concerned, it is given by the inequality (51) involved in the section 3.1.3.1.1.1. For ELISE this minimum electron density is calculated to be $1.4 \times$

$10^{15}\ m^{-3}$. To take a certain margin in equation (51), the minimum electron density n_e for the analyses has been chosen more than one order of magnitude higher $5 \text{ x } 10^{16} \text{m}^{-3}$.

5.3 Estimation of different collision frequencies

5.3.1 Ohmic heating collision frequency

From the input parameters, ohmic heating collision frequency ν_m is obtained as described in 3.1.3.1 where ν_{en}^{p} and ν_{en}^{iz} are calculated from the available cross sections σ_{en}^{p} and σ_{en}^{iz} for Hydrogen gas, taken from reference [68] and [69].

Figure 38 provides an example to show the variation of total momentum loss collision frequency ν_m (for Hydrogen gas) with the electron temperature T_e for the typical operating parameters seen in ELISE driver where electron density, $n_e = 5e18\ m^{-3}$, gas temperature $T_{gas} = 1200\ K$ and gas pressure $P_{gas} = 0.3\ Pa$ are considered. It can be seen that at high electron temperature (approximately above $T_e \approx 20eV$), electron neutral collision frequency ν_{en}^{p} dominates as compared to electron ion collision frequency ν_{ei}^{p}.

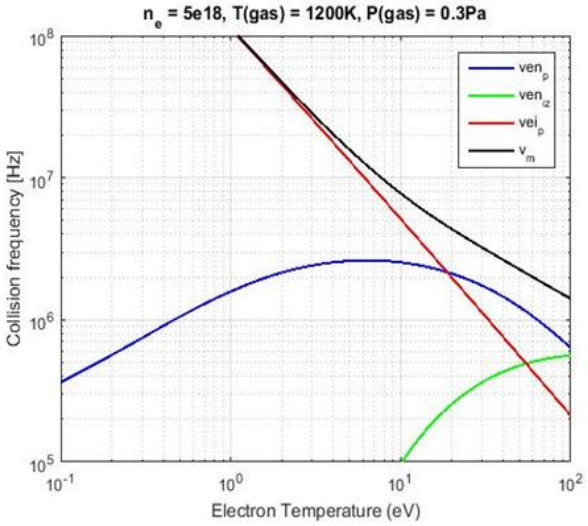

Figure 38: Variation of total collision frequency with electron temperature for Hydrogen gas (for ELISE ion source).

5.3.2 Estimation of the region of the onset of stochastic heating

From the input parameters, the region (in terms of electron density and applied frequency) of onset of stochastic heating is identified as described in section 3.1.3.2. Figure 39 shows the region where the collision-less heating is effective. It also indicates the minimum frequency and electron density required for the onset of collision-less heating for one

particular electron temperature and length of the ion source. For the parameters of ELISE ($T_e = 9\ eV$ and $L = 28\ cm$), the same trend is observed as found in [64].

On the basis of Figure 39 it can be said that for the onset of collision-less heating in ELISE driver, the minimum electron density required is of the order of $3.16 \times 10^{14} m^{-3}$ and the minimum frequency required is of the order of $0.7\ MHz$. Please note that the axis (x and y) in the figure is logarithmic. The typical operational electron density for ELISE is $n_e \approx 10^{18} m^{-3}$ and this is well within the region of the onset of stochastic collision frequency even at 1 MHz.

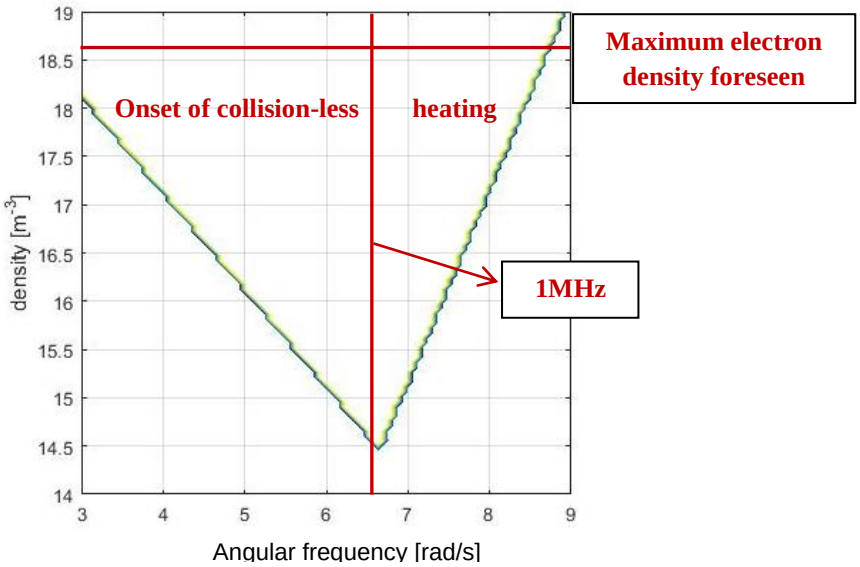

Figure 39: A region showing the onset of collision-less heating for T_e = 9 eV and L = 28 cm (parameters similar to ELISE).

5.3.3 Stochastic heating collision frequency

Using the input parameters and v_m, the stochastic heating collision frequency v_{stoc} is calculated and is shown in Figure 40. As expected v_m shows no variation with respect to frequency but increases with increase in density (dashed line in Figure 40). The v_{stoc} (solid line in Figure 40) first increases and then decreases with respect to frequency and shows a similar behaviour with respect to density as that of v_m. It should be noted that v_{stoc} remains lower than v_m at the lowest and the highest frequencies. It is pointed out that v_{stoc} is modelled based on the assumption that the ions do not respond to the RF fields (see section 3.1.3.2). However, this assumption may not hold to be true for hydrogen gas at 1 MHz; in this case, the ion plasma frequency is found to be higher than the applied frequency. Nevertheless, the electron plasma frequency is found to be much larger than the ion plasma frequency and therefore as a first order approximation, the ion plasma frequency can be neglected [56]. Please note that here v_{stoc} is calculated from skin depth without the consideration of

geometric effects (see section 3.1.3.1.1). Furthermore, the trend of v_{stoc} with electron density remains the same even when geometric effects are considered. A jump (or a discontinuity) observed in Figure 40 is the consequence of the model used for v_{stoc} for two different regimes $\alpha \ll 1$ and $\alpha \gg 1$. The jump here is indicated at $\alpha \approx 1$. This jump has no physical significance.

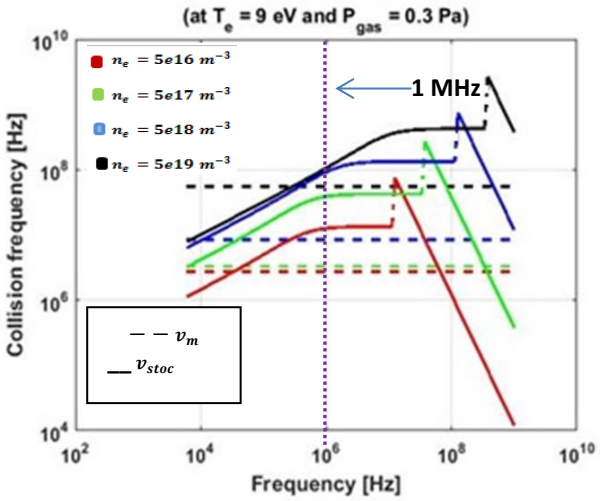

Figure 40: Variation of collision frequency with frequency for different electron densities (for ELISE ion source).

5.4 Effective collision frequency

From the ohmic v_m and the stochastic v_{stoc} heating collision frequencies, the effective collision frequency v_{eff} is calculated (see section 3.2) and it is represented in Figure 41.

Figure 41 shows the variation of v_{eff} (the black curve), v_m (the red curve) and v_{stoc} (blue curve) with the gas pressure at a frequency of 1 MHz, $n_e = 5 \times 10^{18} m^{-3}$ and $T_e = 9\ eV$. It can be seen that stochastic heating is dominant heating mechanism at pressures below 1 Pa. The dominance of stochastic heating at low pressure is in accordance with various research articles [56][59][64][80][81]. The stochastic heating collision frequency v_{stoc} shows a very little dependence on the gas pressure and depends only on n_e (see Figure 40) and T_e (see equations (64) – (66)) while v_m increases with the increase in pressure.

5.5 Effective skin depth

The sum of these two collision frequencies gives the effective collision frequency v_{eff} from which the effective skin depth is calculated using the equation (68). The results are shown in Figure 42 and Figure 43. Usually, when the radius of the chamber is large (i.e. when the radius is much larger than the skin depth), then the geometric effects present in equation (68) are neglected. However, for the smaller chamber these effects should be taken into consideration [59] (see section 3.1.3.1.1). Furthermore, in [70] it is shown that the

finiteness of the plasma have some effects on the calculation of the skin depth. Therefore, in the following graphs a comparison in the calculation of skin depth with and without geometric effects is shown.

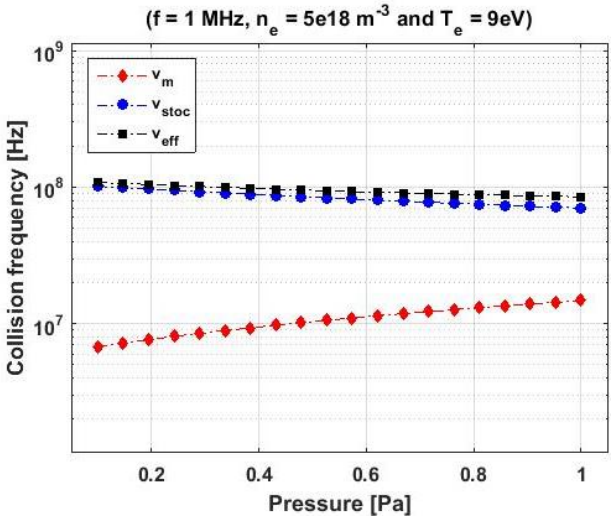

Figure 41: Variation of ohmic, stochastic and effective collision frequency with the pressure (for ELISE source).

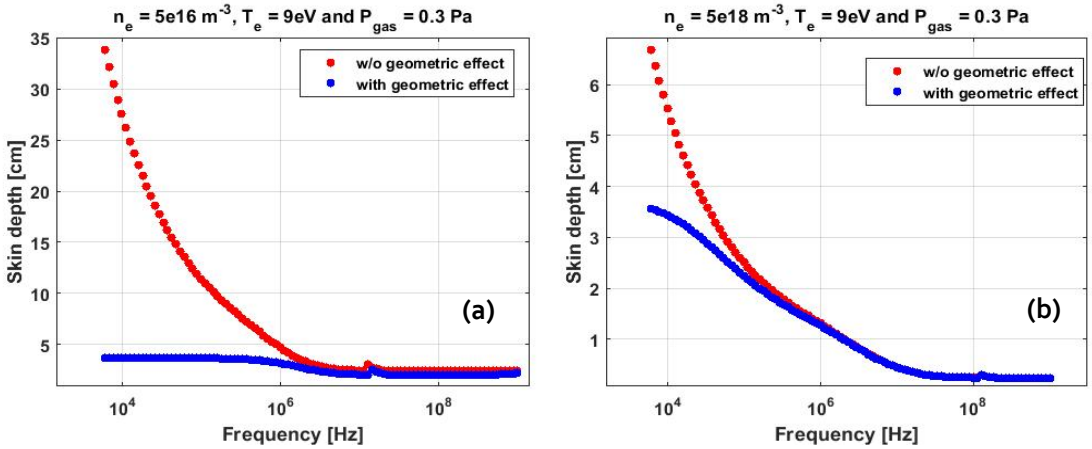

Figure 42: Variation of skin depth with applied frequency for ELISE ion source at (a) low electron density ($n_e = 5e16\ m^{-3}$) and (b) high electron density ($n_e = 5e18\ m^{-3}$).

In Figure 42, the skin depth variation is shown for two conditions (with and without geometric effects) as a function of frequency. Here, two cases are considered; one is shown for low electron density $n_e = 5 \times 10^{16}\ m^{-3}$ (see Figure 42(a)) and other for the usual electron density $n_e = 5 \times 10^{18}\ m^{-3}$ (see Figure 42(b)) observed experimentally in the driver of the ELISE ion source. In both the cases, it can be seen that when geometric effects are not considered, the skin depth increases with decrease in frequency, reaching comparable values to the driver radius. This certainly does not represent a physical scenario. Conversely,

considering the geometric effects it can be seen that the increase in skin depth is minimal with respect to the decrease in frequency for low electron density (this is in accordance with [70]) whereas for high electron density the geometric effects are not so appreciable at high frequencies and are slightly visible only for low frequencies.

The variation of skin depth with and without geometrical effects for different electron densities and gas pressures is shown in Figure 43. With increase in electron density (Figure 43(a)), the skin depth decreases for both cases, i.e., with and without geometric effects. This is because $\delta \propto \frac{1}{\sqrt{n_e}}$ (see equation (68)). The geometrical effects are visible only for lower electron densities and as the density increases the skin depth calculated approaches the same value as the one calculated without geometric effect. With increase in gas pressure (Figure 43(b)), there is very slight decrease in skin depth from 1.3 cm to 1.2 cm (without geometric effect) and from 1.26 cm to 1.16 cm (with geometric effect). This is because v_{eff} decreases very slightly with the increase in gas pressure, see Figure 40.

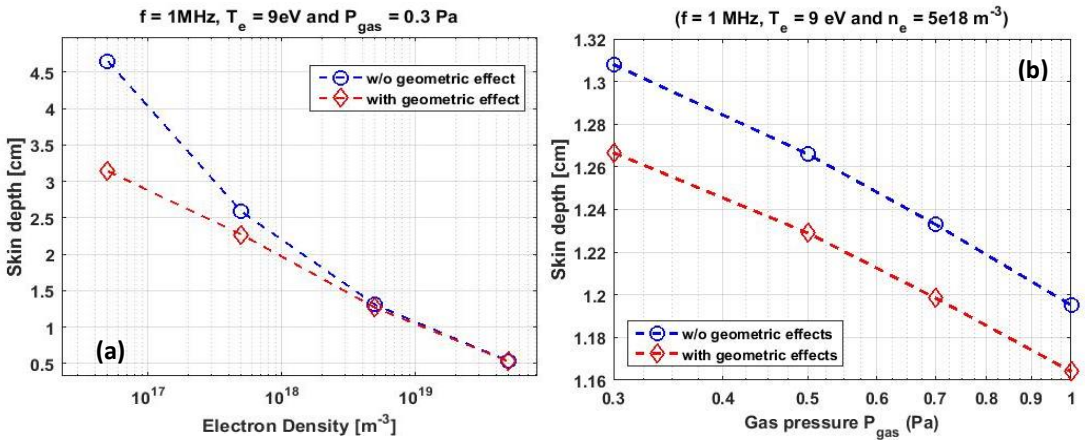

Figure 43: Skin depth variation with (a) Electron density and (b) gas pressure for ELISE ion source.

From Figure 42 and Figure 43, it can be concluded that geometric effects are non-significant at the operating parameters for ELISE ($n_e = 5 \times 10^{18}\, m^{-3}, T_e = 9\, eV$ and $P_{gas} = 0.3\, Pa$) but are slightly significant at low electron density. Therefore, in the following section, the results are shown considering the geometric effects, thus applying equation (50), (57) and (68).

5.5.1 Applied frequency range

The frequency range of 0.6-50 MHz is chosen for the analyses, for several reasons; within this range the frequencies 1 and 13.56 MHz are present. 1 MHz is the working frequency of the ITER and ELISE ion source and 13.56 MHz is the common working frequency of ICPs. We limit the upper frequency range to 50 MHz because above this frequency other phenomena like ion

- ion collisions may start playing an important role in plasma heating, which is not taken into account in the model.

5.6 Electrical model for the power transfer to the plasma

The methodology described in Chapter 4 is applied to the ELISE ion source to calculate the plasma equivalent resistance (PER), R_{peq} and the power transfer efficiency (PTE) ξ. Both the first (transformer) and the improved (multi-filament) approach are applied and are described in the following sections.

5.6.1 Transformer model

The transformer model described in section 3.3.2 is considered which presents some improvements with respect to the classical one [57]. The equivalent electrical scheme of the driver of the ELISE ion source is shown in Figure 32. R_{cp} is taken to be varying proportional to $f^{\frac{1}{2}}$, a reasonable choice considering the small skin depth in conductors at 1 MHz with respect to the conductor thickness. At 1 MHz, R_{cp} and L_{11} are assumed to be 0.5 Ω and $7.5\,\mu H$ respectively [82].

5.6.2 Multi-filament model

The 2D axis symmetrical geometry of the simplified driver of ELISE driver, (the design is shown in Figure 36), along with the passive metallic structure is used as an input for the multi-filament model (described in section 3.3.3), built in MATLAB® (Figure 44). It should be noted that the cylindrical side wall of the Faraday shield is not considered in the model because the structure is not axially symmetric and one needs a 3D model to incorporate it in the model. Therefore only the back plate of the Faraday shield is considered.

Furthermore, in order to reduce the model complexity and the computational time, the exploitation of the skin effect present in harmonic regime has been considered with a simplified approach, namely considering only a single layer of filaments on the surface of the metal parts. These filaments are visible in Figure 44 as blue circles located at the surface of the conductors.

5.7 Results

The results of the application of the methodologies to ELISE ion sources are first shown as a function of frequency $f = \frac{\omega}{2\pi}$. Then, the focus is on the operating parameters of the ELISE ion source at the working frequency of 1 MHz. The relative merit of the multi-filament model

against the transformer one is presented. In all these cases, the plasma radius is assumed to be the same as the chamber radius. Finally, the results are also shown for a scan with respect to the equivalent plasma radius.

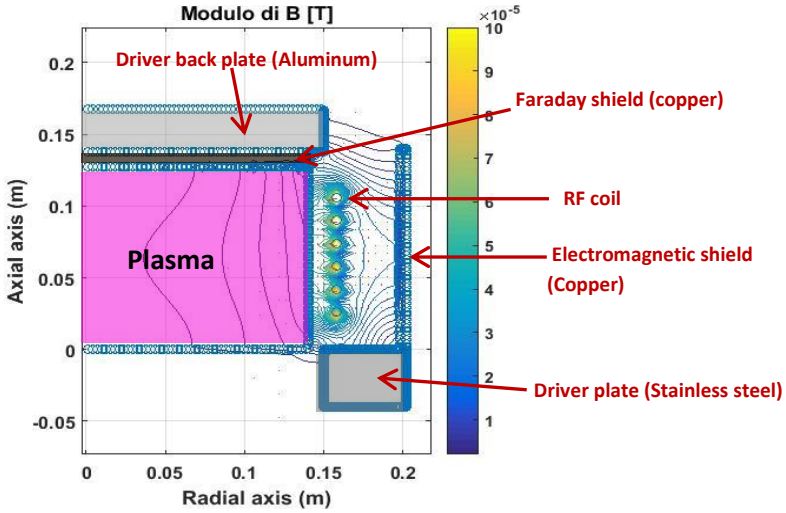

Figure 44: Schematic of the 2D axis-symmetry multi-filament model of the driver of ELISE ion source. An example of the magnetic field pattern within the driver region are also represented when applying an I_{coil} imposed current of 1 A.

5.7.1 Application of the transformer model – PER and PTE versus frequency

In this section the results for the transformer model are shown.

5.7.1.1 *Plasma equivalent resistance (PER) at the primary side of the transformer*

The value of the plasma equivalent resistance is calculated (as shown in equation (86)) at different frequencies and plotted in Figure 45. In these plots we can see that the value of R_{peq} obtained is increasing with the increase in frequency and reaching very high values. In a particular case of low electron density $n_e = 5 \times 10^{16}\, m^{-3}$, R_{peq} first increases and then decreases with the increase in frequency, see Figure 45(a). This behaviour is due to the stochastic heating collision frequency, ν_{stoc}, which increases with the increase in frequency and is much higher than ν_m and then decreases with increase in frequency (see Figure 40). Moreover, it should be noted that at 1 MHz, R_{peq} is found to be about 13 Ω for typical values for ELISE operation. The same methodology is also applied to the ion source mentioned in an example in [56] at 13.56 MHz for an Argon gas discharge. The PER obtained in this case is about 25 Ω which is same as that obtained in [56], thus providing a validation of the developed methodology.

A discontinuity arises as explained in section 5.3.3 due to the modelling of the stochastic heating collision frequency ν_{stoc}, this discontinuity is shown with an interpolation (dashed line) in Figure 45 and Figure 46.

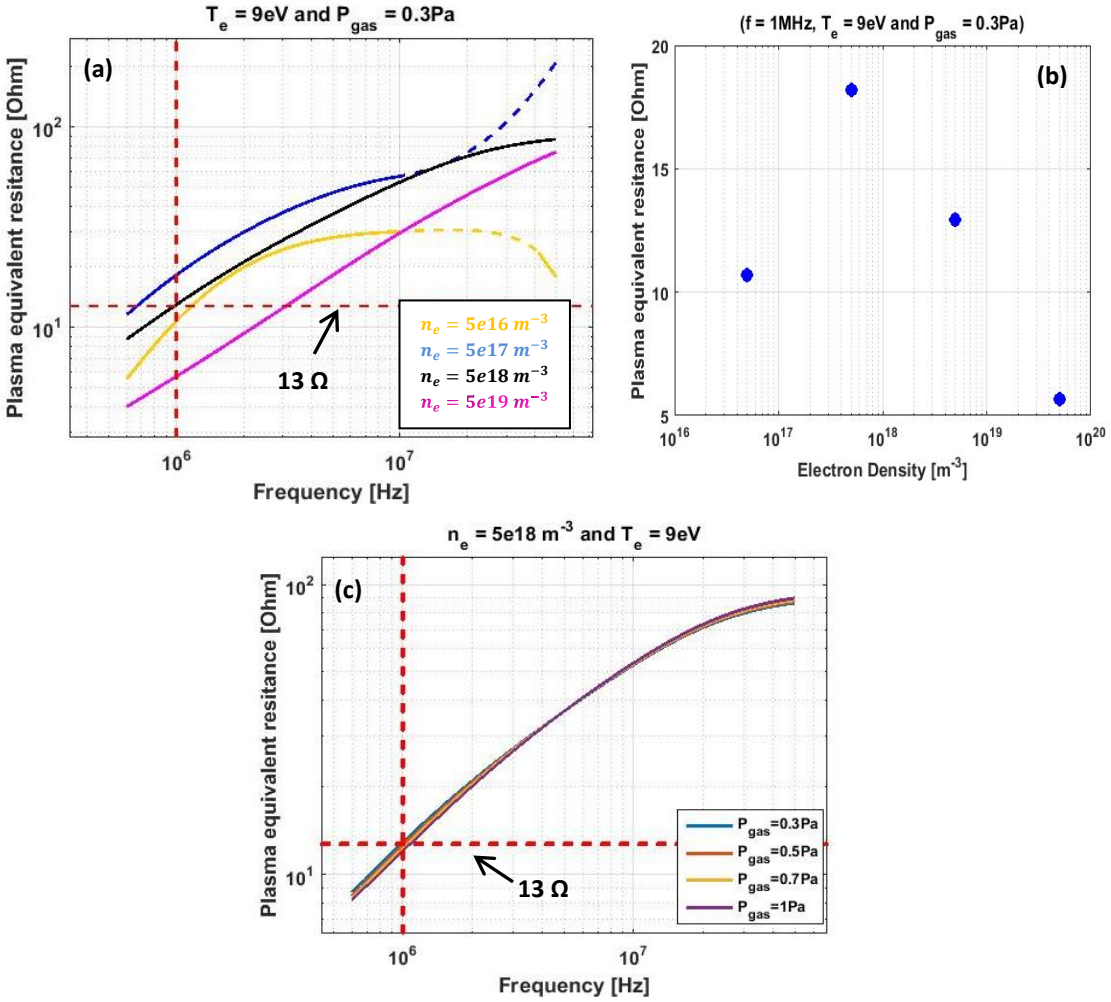

Figure 45: Plasma equivalent resistance for ELISE ion source (a) versus frequency for different densities, (b) for different electron densities at a fixed frequency and (c) for different gas pressures.

With the density variation, see Figure 45(b), the PER first increases and then decreases as also observed in [65]. Furthermore, the mentioned non-monotonic behaviour of the PER in [65] is only observed for a numerical investigation in Argon. All measurement results provided in [65] indicate a monotonic increase with electron density, which is the frequently reported result. Finally, with the pressure variation (see Figure 45(c)), the analyses shows no particular trend of the resistance which is different from what is observed in [65] where the resistance increases with increase in the pressure. This is because in the model considered, ν_{stoc} does not change with the change in pressure, and within this frequency range it is the dominant

collision frequency as compared to the ν_m (Figure 41). It should be noted that the gas used in [65] is a noble gas and the numerical results in Argon may well be valid, however they may not be applicable to hydrogen discharges due to a very different electron neutral collision frequency in Hydrogen and Argon.

5.7.1.2 *Power transfer efficiency (PTE)*

The value of power transfer efficiency at different frequencies is calculated and plotted in Figure 46. With density variation (Figure 46(a)) we can see that ξ increases with the increase in frequency and is over 90%, including the operational working frequency of 1 MHz for ELISE, with the exception at low density and high frequency where the PTE goes as low as ~ 84% . PTE in Figure 46(a), show similar trend with respect to electron density as is seen with the PER, in Figure 45(a) and (b).

With respect to pressure variation (Figure 46(b)), PTE first increases with the increase in frequency, reaches a maximum value and then decreases with the further increase in frequency. This maximum arises at a frequency one magnitude higher than the working frequency of ELISE source. It can also be seen that with the increase in pressure, PTE decreases at low frequency but increases at high frequency.

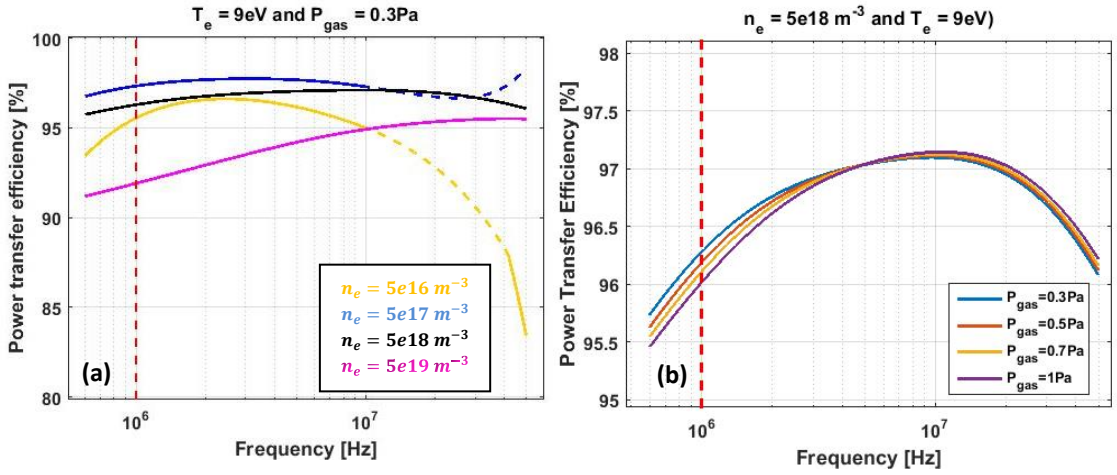

Figure 46: Variation of power transfer efficiency with frequency for different (a) electron densities and (b) gas pressure for ELISE source.

5.7.2 Application of the multi-filament model and comparison with the transformer one

In this section the results for the multi-filament model are shown and are also compared with the results obtained from the transformer model.

5.7.2.1 *PER and PTE versus frequency*

Figure 47 shows a comparison between the results of both transformer (dashed line) and multi–filament (solid line) models for the typical operational parameters for ELISE ion source as a function of frequency. It can be seen that with the multi-filament model both PER and PTE follows the same trend as that of the transformer model. The PER obtained from the multi-filament model is reduced by half as compared to the transformer model, whereas the PTE is reduced by about 4 % (this is due to the consideration of the passive metallic structures in the multi current filament model). Again it can be seen for both the models that PTE increases with the increase in frequency, reaches a maximum value (at around 10 MHz) and then decreases with the further increase in frequency.

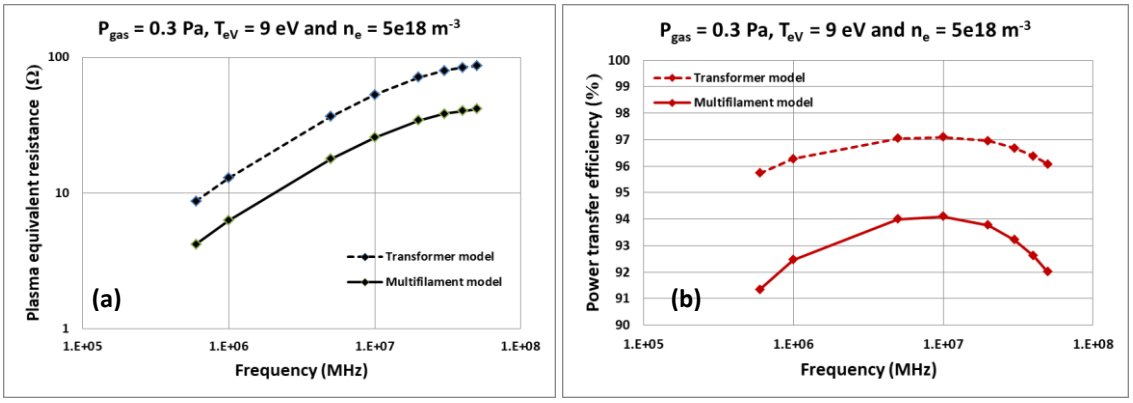

Figure 47: Plasma equivalent resistance variation with frequency and (b) Power transfer efficiency variation with frequency for ELISE source.

5.7.2.2 *PER and PTE versus electron density*

The value of PER and PTE for different electron densities is plotted in Figure 48. In this graph, it can be seen that both PER and PTE increases with the increase in electron density, reaches a maximum value (around $n_e = 5 \times 10^{17}\ m^{-3}$) and then decreases with further increase in electron density. The PER estimated from the multi-filament model is roughly half the value obtained from the transformer model. The PTE reduces by 8 % for high electron density and about 6 % for low electron density.

5.7.2.3 *PER and PTE versus gas pressure*

The value of PER and PTE for different gas pressure is plotted in Figure 49. The PER estimated from the multi-filament model is roughly half the value obtained from the transformer model and the PTE is reduced by approximately 4%. In this graph, it can be seen that both PER and PTE decreases slightly with the increase in gas pressure. The behavior of PER is different from what is observed experimentally in [65] for different inert gases like Ne, Ar and Kr. However, for He the same behavior is seen at higher gas pressure above 2.6 Pa. A

possible interpretation of the discrepancies between the results obtained from the noble gases and hydrogen is that they could be due to the different electron neutral collision frequency in Hydrogen and in noble gases.

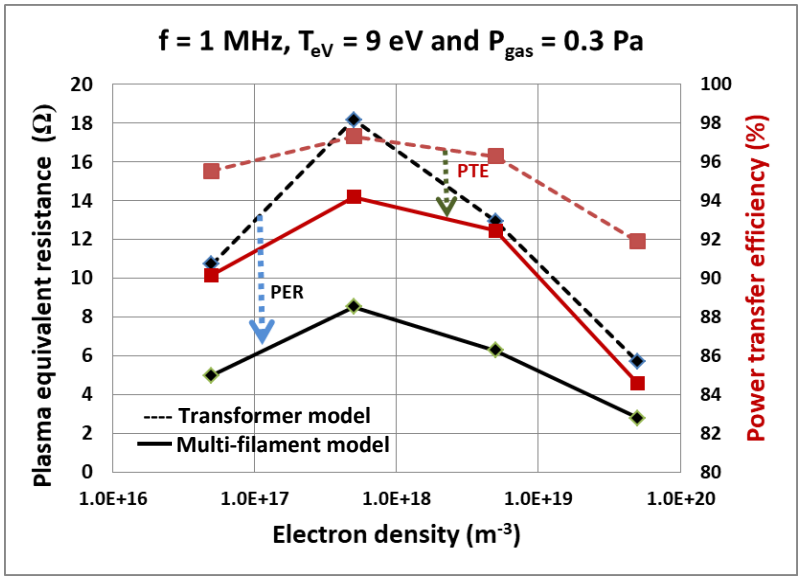

Figure 48: Plasma equivalent resistance and power transfer efficiency variation with electron density for ELISE source.

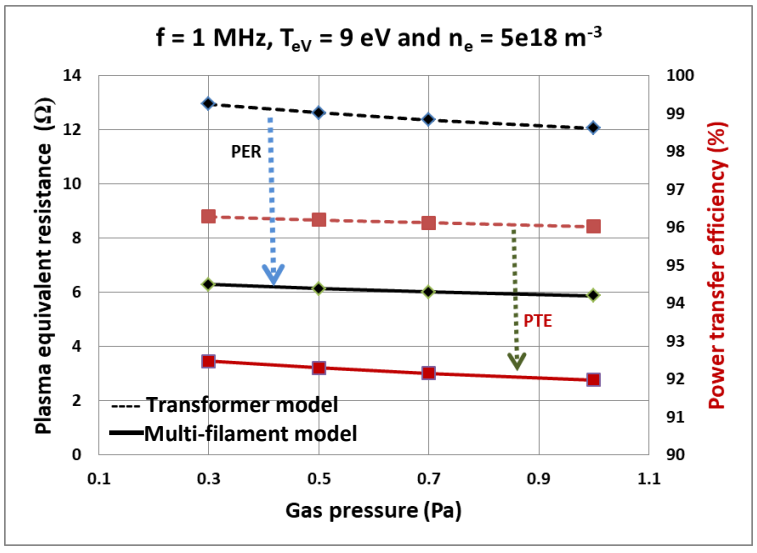

Figure 49: Plasma equivalent resistance and power transfer efficiency variation with gas pressure for ELISE source.

5.7.2.4 *PER and PTE versus the plasma radius*

In the work of Kralkina [65], it is shown numerically that the plasma equivalent resistance does not reach very high values with the increase in frequency. This is contrary to what is found in section 5.7.1.1 and 5.7.2.1 (sometimes reaching more than 100 Ω at 50 MHz).

Moreover, at 1MHz, a reasonable value for the driver equivalent resistance for ELISE source has been derived experimentally to be around 1.8 Ω [83], whereas in section 5.7.1 and 5.7.2 the values obtained at this frequency (for typical operating parameters for ELISE) are found to be about 13 Ω with the transformer model and about 6.5 Ω with the multi-filament model. From the developed methodology, it is reasonable to expect high plasma equivalent resistance (PER) because the influence of the effect of the induced and external magnetic field [62] [84], the effect of the density profile [85] etc. are not considered. Therefore, to start facing one of these model limitations, analyses have been made, particularly addressed to understand the effect of the geometric dimension of the plasma-current sheet (in particular the plasma radius). It has been observed experimentally that the plasma density is not uniform in the entire chamber region; it is maximum at the centre and decreases near the edges [85]. This means that the plasma in the outer region near the boundary is less conductive than in the inner one. Assuming a step wise approximation for the density profile and considering the outer region as non-significant, the equivalent plasma resistance can be calculated for an intermediate value of the radius.

Since the plasma equivalent resistance calculated from the multi-filament model can be considered more realistic than that obtained from the transformer model, in this section the results are presented only for the multi-filament model. A scan with respect to plasma radius (from 5 – 14cm) is presented in Figure 50 at 1MHz (for typical values of ELISE operation). It is pointed out that the consideration of such unrealistic range for the variation of the plasma equivalent radius is done only to perform a sensitivity analysis.

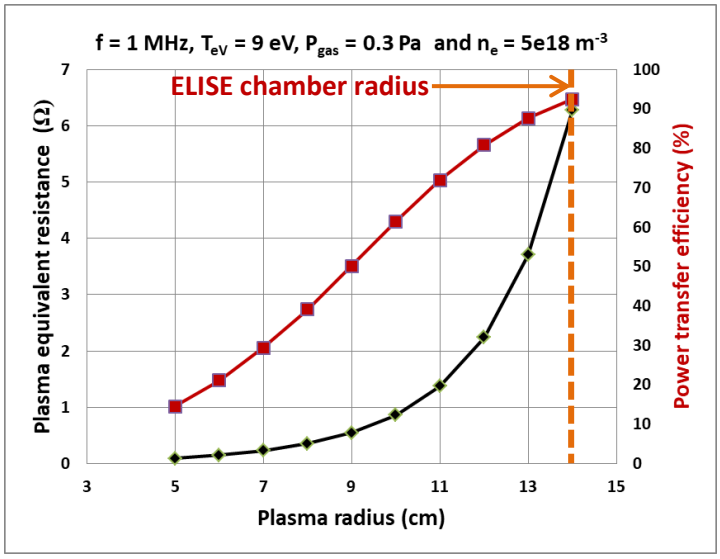

Figure 50: Plasma equivalent resistance and power transfer efficiency variation with plasma radius using multi-filament model for ELISE ion source.

The reduction of the equivalent plasma radius within the chamber suggests a reduction in the PER and PTE. The PER reduces from about 6.5 Ω at 14 cm plasma radius to about 0.1 Ω at the plasma radius of 5 cm. The PTE decreases by 85% in reducing the plasma radius from 14 cm to 5 cm. The experimentally derived value of 1.8 Ω [83] is found at a plasma radius of 11 – 12 cm from the methodology presented in this thesis with the multi-filament model.

5.8 Discussion

The methodology presented in Chapter 4 with transformer and multi-filament model is applied to the specific case of ELISE IC ion source. As far as heating mechanisms for the plasma is considered, stochastic heating is found to be dominant in comparison with the ohmic heating, in the gas pressure range below 1 Pa. It is found that geometric effects for skin depth calculations are less significant for ELISE source and are visible only for low electron densities.

With the transformer model, the results show that for most of the cases, plasma equivalent resistance increases with the increase in frequency reaching relatively high values and, at 1 MHz in particular, it is approximately seven times higher than the experimentally derived value (section 5.7.1.1). However, with the implementation of the multi-filament model, the plasma equivalent resistance reduces by half the value obtained from the transformer model and assuming an equivalent plasma radius in order to account in some way for the non-uniform plasma density profile, the experimental value is found for a plasma radius of about 20% lower.

The models worked out surely presents some limits, in particular in the description of the stochastic heating contribution for plasma heating and in the validity of some assumptions, like for example the equivalent plasma radius.

From both models, it can be seen that the power transfer efficiency increases with the increase in operating frequency reaching maximum values around 10 MHz, thus indicating in this range the preferable operating frequency.

Chapter 6.

Application to the NIO1 ion source

In this chapter the methodology described in Chapter 4, with the transformer (see section 3.3.2) and the multi-filament (see section 3.3.3) model is applied to NIO1 ion source operating with Hydrogen gas. The following sections will describe the driver and the input parameters taken for this ion source along with the calculation of the ohmic and stochastic heating collision frequencies. Identification of ranges of electron density and operating frequency for parametric scans will also be shown based on the calculation of the effective skin depth. The significance of the geometric effects will be highlighted during calculation of the effective skin depth. Eventually, the results focusing on the plasma equivalent resistance and power transfer efficiency will be presented and compared for both models.

6.1 Description of the Driver

The schematic and the 3D drawing cut-view of the NIO1 ion source are shown in Figure 51. NIO1 has a small RF negative ion source (with the chamber diameter of 10 cm), designed to have a high degree of flexibility in the hardware configuration. The RF coil has 7 windings and is made of copper. The Faraday screen and the expansion region are not present in the NIO1 ion source and this is the main difference with respect to the IPP type ion sources. The inner surface of the source is made up of copper material except in the middle of the RF module where an alumina cylinder isolates the region in vacuum from the RF coil. Permanent magnets are mounted in the source body to protect the inner surfaces and reduce plasma losses.

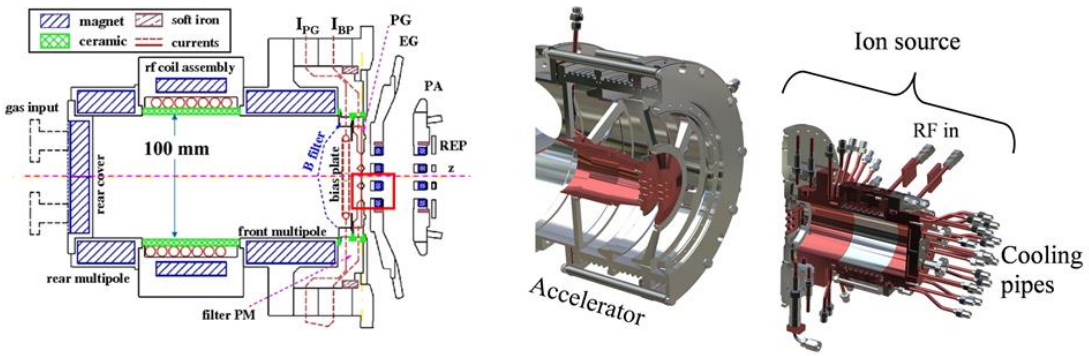

Figure 51: NIO1 ion source: schematic (left) [86] and 3D drawing cut-view (right) of the driver and the accelerator region.

6.2 Input parameters

The description of NIO1 (Negative Ion Optimization 1) ion source is provided in section 2.5.2 and the schematic of the NIO1 ion source can be seen in Figure 51. The geometrical parameters and plasma quantities (seen during the operation) for the NIO1 driver region are listed in Table 7.

Table 7: NIO1 driver parameters

Geometrical parameters	**Value**
Chamber radius [mm]	50
Number of coil turns	7
Coil radius [mm]	59.5
Solenoid coil length[mm]	63.8
Plasma quantities*	
Gas type	Hydrogen
Electron density, n_e [m^{-3}]*	$\sim 10^{17}$
Electron temperature , T_e [eV]**	<7
Gas Pressure, P_{gas} [Pa]	Above 1 Pa
Gas temperature, T_g [K]	400-500

* and ** are taken from [87] and depends upon P_{gas} , T_{gas} and B field in the source

6.2.1 Estimation of the electron temperature

An estimation of the electron temperature within the driver region of NIO1 ion source is obtained as a function of gas pressure and temperature (see section 3.1.2) and is shown in Figure 52.

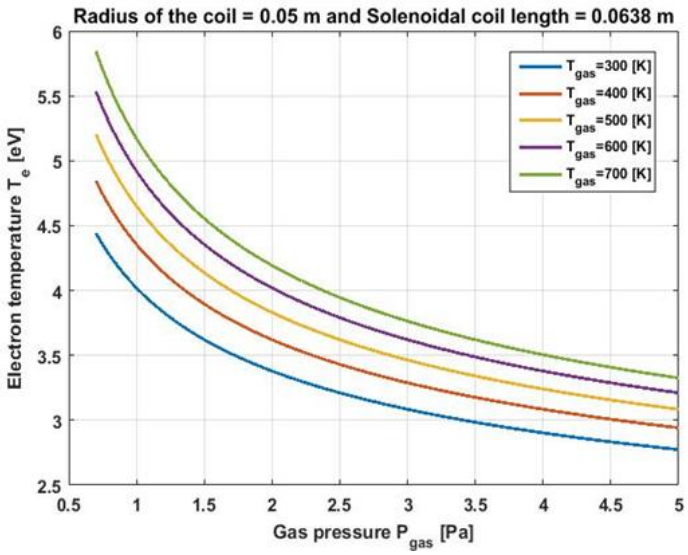

Figure 52: Estimation of electron temperature with gas pressure for the driver of NIO1 ion source.

It can be seen that T_e decreases with the increase in pressure P_{gas} for all the gas temperatures T_{gas}. The same trend is also observed in other ion source of similar type [78].

From Figure 52, we see that at 400 K and at the pressure of 2.5 Pa (typical value for NIO1 operation), T_e is around 3.5 eV and is used as one of the input parameters of the developed methodology.

6.2.2 Electron density range

As far as the minimum electron density is concerned, it is given by the inequality (51) involved in the section 3.1.3.1.1.1. For NIO1 this minimum electron density is calculated to be $1.13 \times 10^{16} m^{-3}$. To take a certain margin in equation (51) the minimum electron density n_e for the analyses has been chosen one order of magnitude higher, i.e., $1 \times 10^{17} m^{-3}$.

In [87], it is shown experimentally that electron density is about $2 \times 10^{17} m^{-3}$ at the edge of the driver region of NIO1 ion source. This electron density is measured at the RF power of 1 kW and gas pressure of 1.5 Pa with a negligible external magnetic field. In this work, four electron densities n_e from $(1-4) \times 10^{17} m^{-3}$ are taken, in order to observe the trend of the results with the density variation.

6.3 Estimation of different collision frequencies

6.3.1 Ohmic heating collision frequency

From these input parameters, ohmic heating collision frequency v_m is obtained as described in 3.1.3.1 where v_{en}^{p} and v_{en}^{iz} are calculated from the available cross sections σ_{en}^{p} and σ_{en}^{iz} for Hydrogen gas, taken from reference [68] and [69]. Figure 53 provides an example to show the variation of total momentum loss collision frequency v_m (for Hydrogen gas) with the electron temperature T_e for the typical operating parameters seen in NIO1 driver where electron density, $n_e = 3e17\ m^{-3}$, gas temperature $T_{gas} = 400\ K$ and gas pressure $P_{gas} = 2.5\ Pa$. It can be seen that at high electron temperature (approximately above $T_e \approx 1eV$), electron neutral collision frequency v_{en}^{p} is higher as compared to electron ion collision frequency v_{ei}^{p}.

6.3.2 Estimation of the region of the onset of stochastic heating

From the input parameters, the region (in terms of electron density and applied frequency) of onset of stochastic heating is identified as described in section 3.1.3.2. Figure 54 shows the region where the collision-less heating is effective. Both x and y axis in the Figure 54 are logarithmic. It also indicates the minimum frequency and electron density required for the onset of effective collision-less heating for one particular electron temperature and length

of the ion source. For the parameters of NIO1 ($T_e = 3.5\,eV$ and $L = 10\,cm$), we see that the same trend is observed as found in [64].

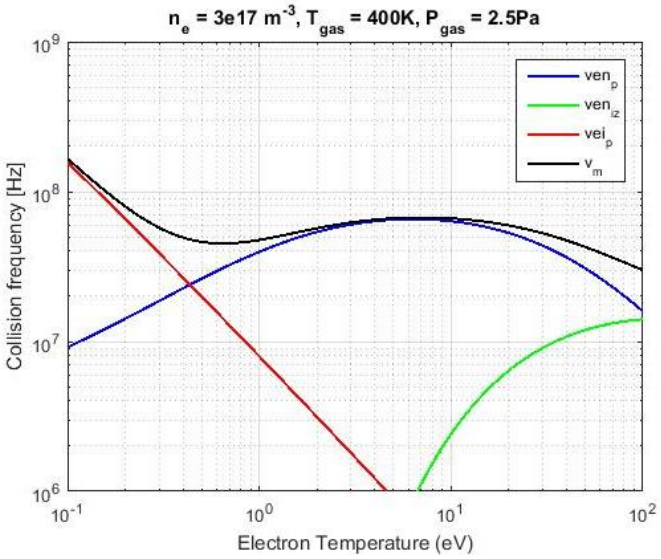

Figure 53: Variation of total collision frequency with electron temperature for Hydrogen gas (for NIO1 ion source).

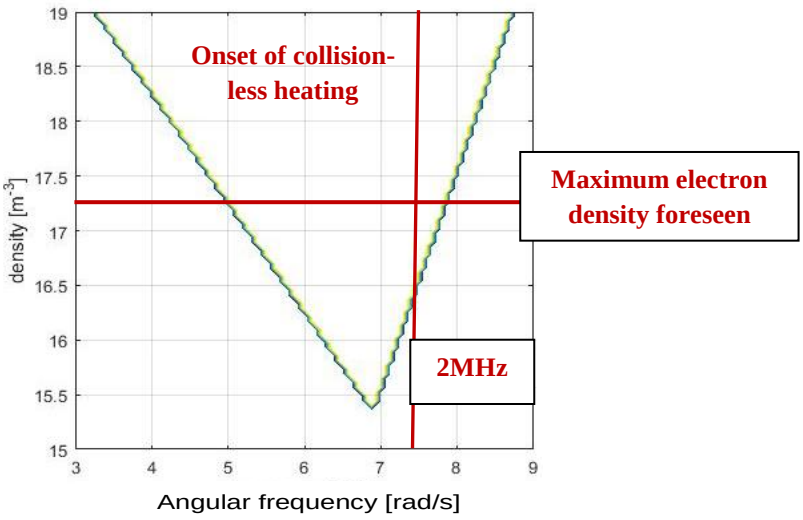

Figure 54: A region showing the onset of collision-less heating for T_e = 3.5 eV and L = 10 cm (parameters similar to NIO1).

On the basis of Figure 54, it can be said that for the onset of collision-less heating in NIO1 driver, the minimum electron density required is of the order of $2.5 \times 10^{15}\,m^{-3}$ and the minimum frequency required is of the order of $1.1\,MHz$. Please note that the axis (x and y) in the figure is logarithmic. The typical operational electron density for NIO1 is $n_e \approx 10^{17} m^{-3}$. This electron density is at the verge of the green curve on the right hand in Figure 54 at 2 MHz.

This suggests that the stochastic heating within the NIO1 may exist and maybe is also significant. Hence the stochastic heating collision frequency is included in the analyses performed and the results are in the next section.

6.3.3 Stochastic heating collision frequency

Using the input parameters and v_m, the stochastic heating collision frequency v_{stoc} is calculated and is shown in Figure 55.

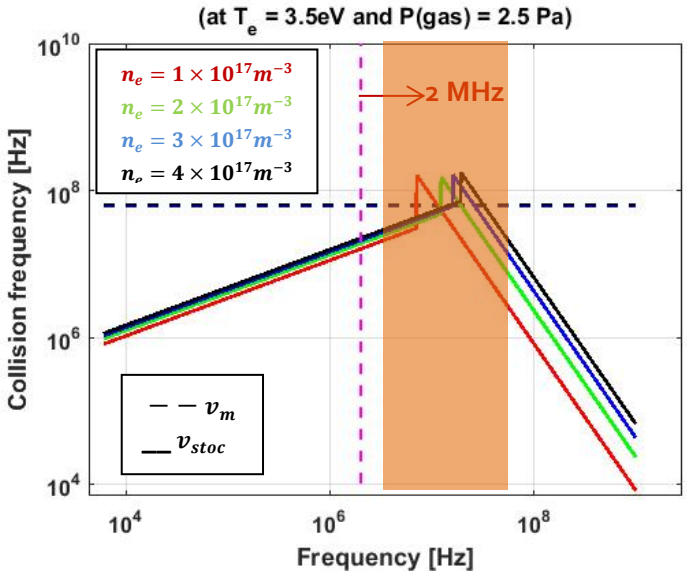

Figure 55: Variation of collision frequency with frequency for different electron densities (NIO1 source). The region highlighted in orange shows a discontinuity which appears because of the model considered for v_{stoc} where the solution for v_{stoc} is available for two disjoint regimes.

As expected, v_m shows no variation with respect to frequency, but increases with increase in density (see the dashed line Figure 55). This effect is not visible here, because of the scale of the graph considered on the y axis, taken to be very large in order to show stochastic heating collision frequency as well. The v_{stoc} (solid line in Figure 55) first increases and then decreases with respect to frequency and shows a similar behaviour with respect to density as that of v_m. It should be noted that v_{stoc} usually remains lower than v_m for most of the applied frequencies. It is pointed out that v_{stoc} is modeled based on the assumption that the ions do not respond to the RF fields. However, this assumption may not be true for hydrogen gas at 2 MHz; in this case, the ion plasma frequency is found to be higher than the applied frequency. Nevertheless, the electron plasma frequency is found to be much larger than the ion plasma frequency and therefore as a first order approximation ion plasma frequency can be neglected [56]. Please note that here v_{stoc} is calculated from skin depth without considering of

geometric effects. Furthermore, the trend of v_{stoc} with electron density remains same even when the geometric effects are considered.

6.4 Effective collision frequency and skin depth

From the ohmic v_m and the stochastic v_{stoc} heating collision frequencies, the effective collision frequency v_{eff} is calculated (see section 3.2) and is shown in Figure 56.

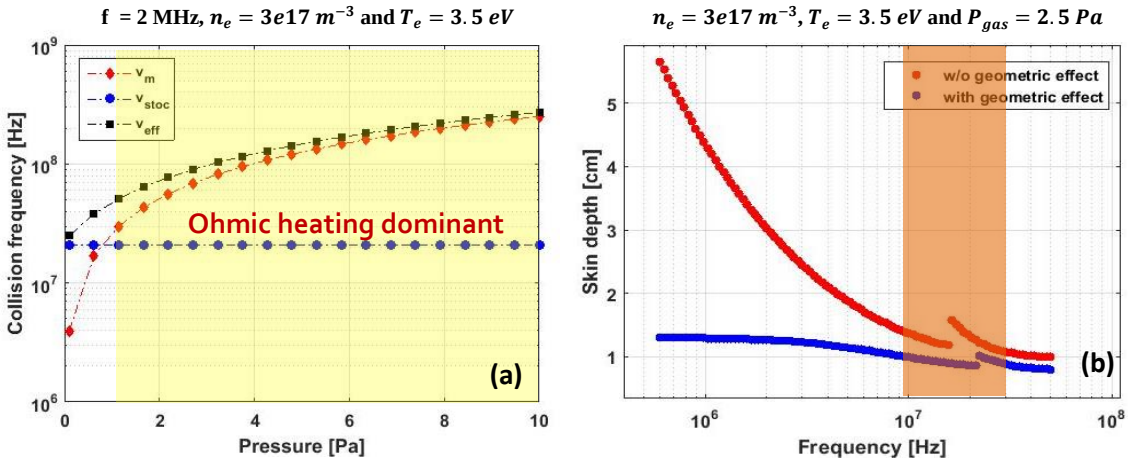

Figure 56: Variation of (a) effective, ohmic and stochastic collision frequency with gas pressure and (b) skin depth with applied frequency for NIO1 source .The region highlighted in orange shows a discontinuity which appears because of the model considered for v_{stoc} where the solution for v_{stoc} is available for two disjoint regimes.

Figure 56(a) shows the variation of v_{eff} (the black curve), v_m (the red curve) and v_{stoc} (blue curve) with the gas pressure at the frequency of 2 MHz, $n_e = 3 \times 10^{17} m^3$ and $T_e = 3.5\ eV$ (typical operating parameters). It can be seen that stochastic heating is dominant heating mechanism at low pressures (below 1 Pa), whereas ohmic heating is dominant at higher pressures (yellow area). The dominance of stochastic heating at low pressure is in accordance with various research articles [56], [59], [64], [80], [81]. It can be seen that v_{stoc} is independent of the pressure variation and depends only on n_e and T_e, while v_m increases with the increase in pressure.

From the input parameters and the effective collision frequency v_{eff}, the effective skin depth is calculated from equation (68) and the results are shown in Figure 56(b) and Figure 57. Usually, when the radius of the chamber is large, then the geometric effects present in equation (2) are neglected. However, for the smaller chamber these effects should be taken into consideration [59], [70]. In Figure 56 (b), the skin depth variation is shown for two conditions (with and without geometric effect) as a function of frequency. Without the consideration of the geometric effect, it can be seen that the skin depth increases with the

decrease in frequency, reaching values comparable to the driver radius. This certainly does not represent a physical scenario. Conversely, considering the geometric effects it can be seen that the increase in skin depth is minimal with respect to the decrease in frequency. This is in accordance with [70] where it is shown that due to the finiteness of the plasma within the driver, the skin depth does not increase very much even at the low frequencies.

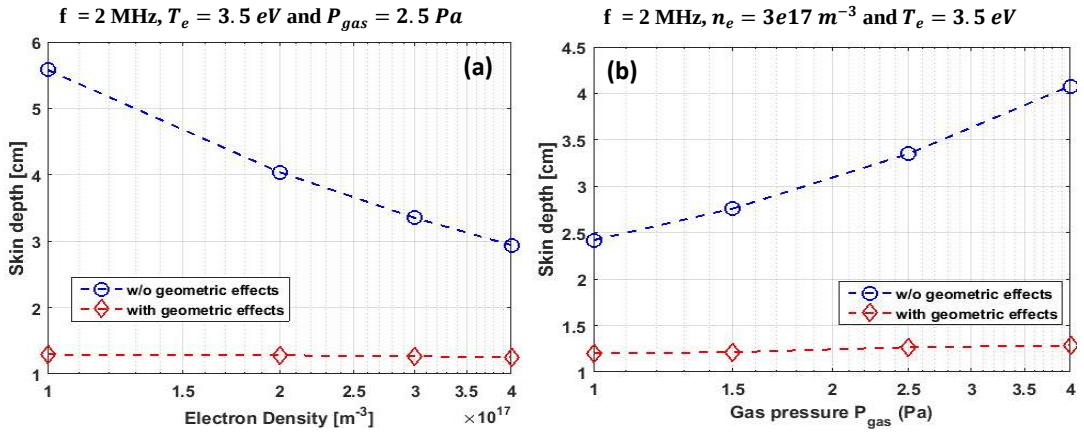

Figure 57: Skin depth variation with (a) electron density and (b) gas pressure for NIO1 source.

A discontinuity in the skin depth curves highlighted in the orange region in Figure 56(b) appears because of the model considered for v_{stoc}, where the solution for v_{stoc} is available as a limit for two disjoint regimes (see also Figure 55). The variation of skin depth with and without geometrical effects for different electron densities and gas pressures is shown in Figure 57. Without the geometric effects, the skin depth decreases with the increase in density, (Figure 57(a)), this is because $\delta \propto \frac{1}{\sqrt{n_e}}$ (see equation (68)). On the other hand, the skin depth increases with the increase in gas pressure (Figure 57 (b)) because v_{eff} increases with the increase in gas pressure, see Figure 56(a). The effect of electron density and gas pressure on the skin depth is less prominent when geometric effects are considered and this seems reasonable. In the following section, the results are shown considering the geometric effects, thus applying equation (50), (57) and (68).

6.4.1 Applied frequency range

The frequency range of 0.6-50 MHz is chosen for the analyses, for several reasons; within this range the frequencies 1, 2 and 13.56 MHz are present. 1 and 2 MHz are the working frequency of the ITER ion source and NIO1 ion source and 13.56 MHz is the common working frequency of ICPs. We limit the upper frequency range to 50 MHz because above this frequency other phenomena like ion - ion collisions may start playing an important role in plasma heating, which is not taken into account in the model.

6.5 Electrical model for the power transfer to the plasma

The methodology described in Chapter 4 is applied to the NIO1 ion source to calculate the plasma equivalent resistance (PER), R_{peq} and the power transfer efficiency (PTE). Both the first and the improved approach are applied and are described in the following sections.

6.5.1 Transformer model

As described in section 3.3.2, the "classical" transformer model is considered with some improvements. The equivalent electrical scheme of the driver of the NIO1 ion source is shown in Figure 32. R_{cp} is taken to be varying proportional to $f^{\frac{1}{2}}$, a reasonable choice considering the small skin depth with respect to the conductor thickness. At 2 MHz, R_{cp} is assumed to be 0.3 Ω.

6.5.2 Multi-filament model

The 2D axis symmetrical geometry of the full NIO1 driver, shown in Figure 51, along with the passive metallic structure is built in MATLAB® (Figure 58) and is used as an input for the multi-filament model (described in section 3.3.3). Furthermore, in order to reduce the model complexity and the computational time, the exploitation of the skin effect present in harmonic regime has been considered with a simplified approach, namely considering only a single layer of filaments on the surface of the metal parts. These filaments are visible in Figure 58 as blue circles located at the surface of the conductors. Magnetic field pattern within the driver region are also represented when applying an I_{coil} impressed current of 1 A

6.6 Results

The results of the application of the methodologies to the NIO1 ion sources are first shown as a function of frequency, $f = \frac{\omega}{2\pi}$; then, the focus is more on the operating parameters of the NIO1 ion source at the working frequency of 2 MHz. The relative merit of the multi-filament model against the transformer one is presented. In all these cases, the plasma radius is assumed to be the same as the chamber radius. Finally, the results are also shown for a scan with respect to the equivalent plasma radius.

6.6.1 Application of the transformer model – PER and PTE versus frequency

6.6.1.1 *Plasma equivalent resistance (PER) at the primary side of the transformer*

The value of the plasma equivalent resistance is calculated (as shown in equation (86)) at different frequencies and plotted in Figure 59.

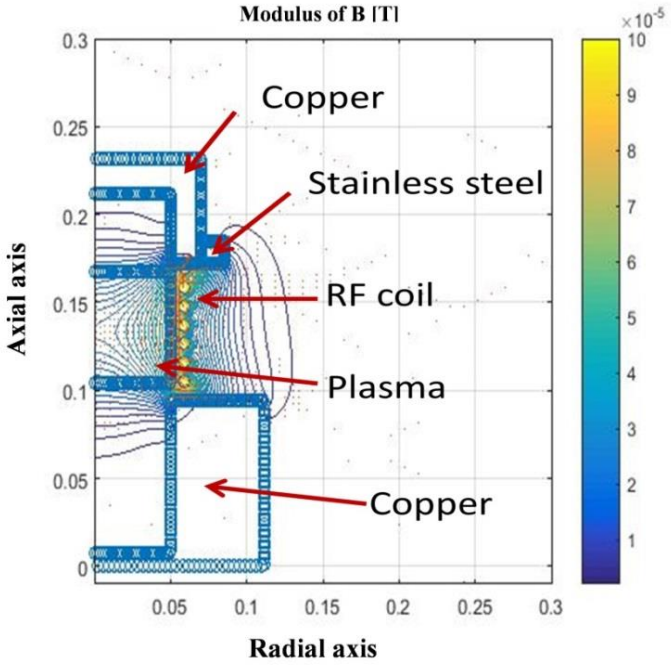

Figure 58: Schematic of the 2D axis-symmetry multi-filament model of the driver of the NIO1 ion source. An example of the magnetic field pattern within the driver region are also represented when applying an I_{coil} impressed current of 1 A.

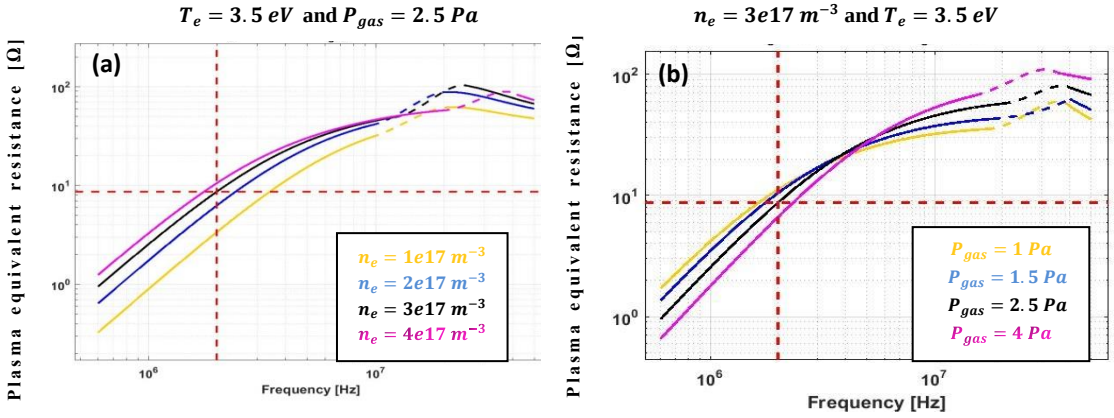

Figure 59: Variation of plasma resistance with frequency for different (a) electron density and (b) gas pressure for NIO1 source.

It can be noticed that at 2 MHz, PER is found to be about 9 Ω for typical values for NIO1 operation. In these plots, we can see that the value of PER obtained is first increasing with the increase in frequency, reaches a maximum value and then decreases with a further increase in frequency. A discontinuity arises as explained in section 6.4 due to the modelling of the stochastic heating collision frequency ν_{stoc}, this discontinuity is shown with an interpolation (dashed line) in Figure 59 and Figure 60. The results obtained in this range may not be reliable.

With the density variation, see Figure 59(a), the PER increases with the density increase. All the measurement results provided in [65] indicate a monotonic increase with electron density, which is also the frequently reported result. With the pressure variation (see Figure 59 (b)), the analyses show that at lower frequencies, the PER decreases with the increase in pressure whereas at higher frequencies the PER increases with the increase in pressure. This trend of the increase of the resistance with the increase in pressure is also observed in [65]. It should be noted that the gas used in [65] is a noble gas (like He, Ne, Ar and Kr) and here we use hydrogen gas, which has a very different electron-neutral collision frequency as compared to a noble gas.

6.6.1.2 *Power transfer efficiency (PTE)*

The value of power transfer efficiency at different frequencies is calculated and plotted in Figure 60. In these plots we can see that PTE increases with the increase in frequency and then reaches a maximum value. At low frequency and low density, the PTE reaches as low as 65 % whereas at high frequency it reaches as high as 97 %. With respect to the density or pressure variation, PTE in Figure 60(a) and (b), show similar trend as is seen with the PER, in Figure 59.

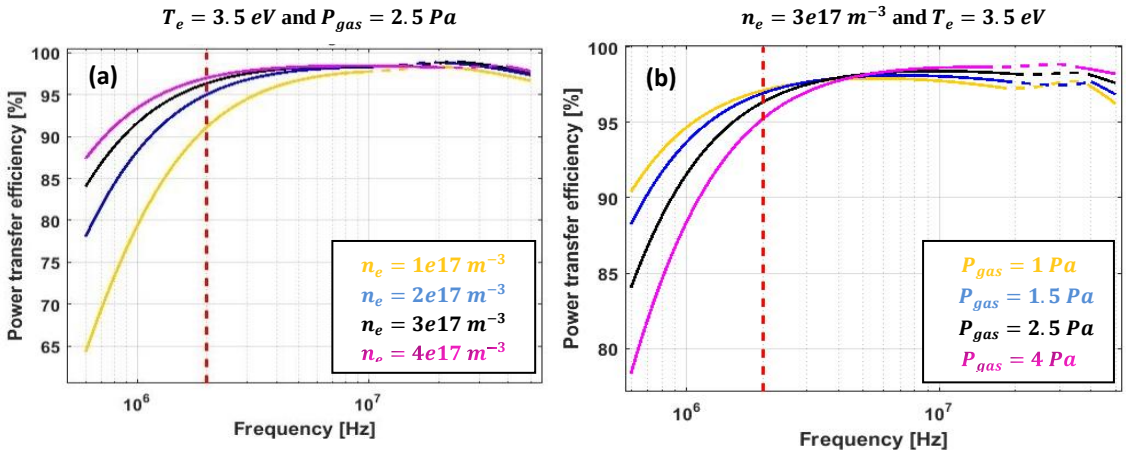

Figure 60: Variation of power transfer efficiency with frequency for different (a) electron densities and (b) gas pressure for NIO1 source.

6.6.2 Application of the multi-filament model and comparison with the transformer one

6.6.2.1 *PER and PTE versus frequency*

Figure 61 shows a comparison between the results of both transformer (dashed line) and multi-filament (solid line) models for the typical operational parameters for NIO1 ion source as a function of frequency. It can be seen that with the multi-filament model both PER and PTE follows the same trend as that of transformer model. The PER obtained from multi-filament

model is reduced by half as compared to the transformer model, whereas the PTE is reduced by 2 %, with an exception at low frequency where it is reduced considerably to about 18 %. At lower frequencies, the value of PTE is lower compared to the value at higher frequencies; this is because at lower frequencies the PER is comparable to the resistance of the passive metallic structure. However, as the frequency increases, the PER becomes much larger than the resistance of the passive metallic structure and thus negligible power is dissipated in the metallic structure.

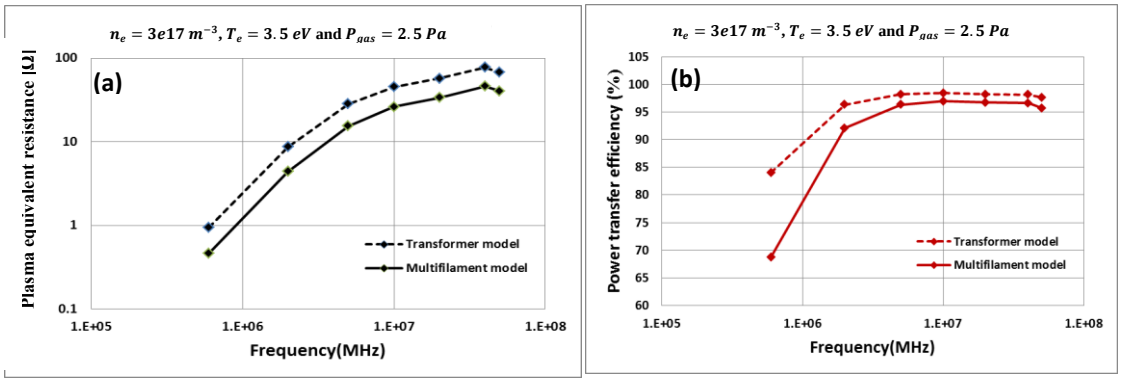

Figure 61: (a) Plasma equivalent resistance variation with frequency and (b) Power transfer efficiency variation with frequency for NIO1 source.

6.6.2.2 *PER and PTE versus electron density*

The value of PER and PTE for different electron densities is plotted in Figure 62. In this graph, it can be seen that both PER and PTE increases with the increase in electron density. The same behavior of PER is also observed experimentally in [65] for different inert gases like He, Ne, Ar and Kr. The PER estimated from the multi-filament model is roughly half the value obtained from the transformer model. The PTE reduces by 4 % for high electron density and about 10 % for low electron density.

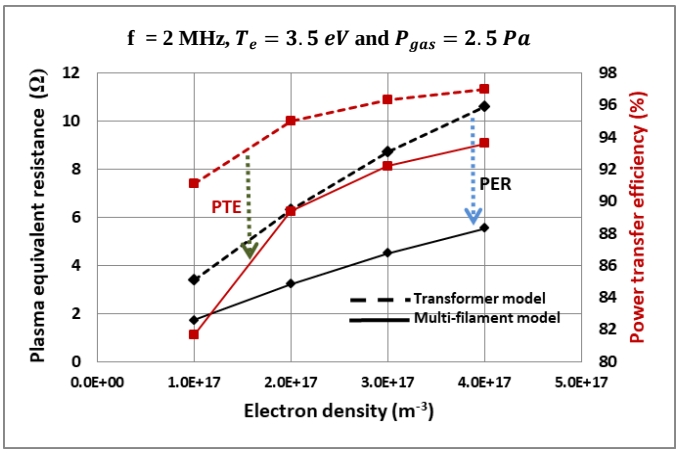

Figure 62: Plasma equivalent resistance and power transfer efficiency variation with electron density for NIO1 source.

6.6.2.3 *PER and PTE versus gas pressure*

The value of PER and PTE for different gas pressure is plotted in Figure 63. The PER estimated from the multi-filament model is roughly half the value obtained from the transformer model. The PTE reduces by 4% for low gas pressure and about 6% for high gas pressure.

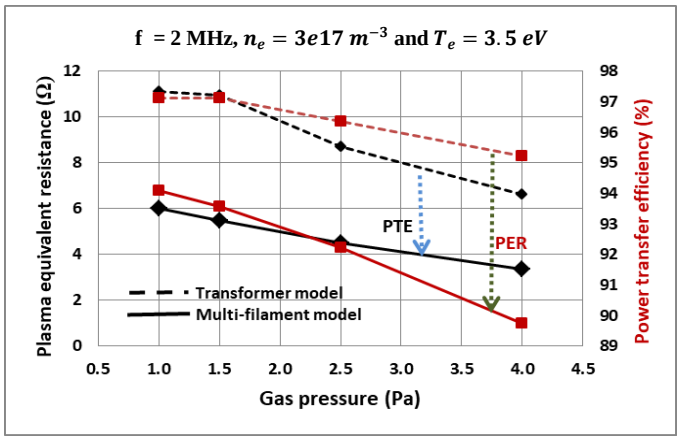

Figure 63: Plasma equivalent resistance and power transfer efficiency variation with gas pressure for NIO source.

In this graph, it can be seen that both PER and PTE decrease with an increase in gas pressure. The behavior of PER is different from what is observed experimentally in [65] for different inert gases like Ne, Ar and Kr. However, for He the same behavior is seen at higher gas pressure above 2.6 Pa. A possible interpretation of the discrepancies between the results obtained from the noble gases and hydrogen is that they could be due to the different electron neutral collision frequency in Hydrogen and in noble gases.

6.6.2.4 *PER and PTE versus the plasma radius*

The results obtained in the previous sections are calculated by considering the uniform electron density within the plasma chamber. However it has been observed experimentally that the plasma electron density is not uniform in the entire chamber region; it follows a profile showing a maximum at the center and decreasing values near the edges [85]. This implies that the plasma in the inner region is more conducting than that in the outer region because an increase in the density means an increase in the conductivity (see equation 27 in section 3.1.1.2). So as a first approximation, the outer region is considered non-significant and a radial step-wise density profile is assumed. The equivalent plasma resistance can be calculated for an intermediate value of the radius. Since the plasma equivalent resistance calculated from the multi-filament model can be considered more realistic than that obtained from the transformer model, in this section the results are presented only for the multi-

filament model. A scan with respect to the plasma radius (from 5-2 cm) is presented in Figure 64 at 2 MHz and for typical values of NIO1 operation. It is pointed out that consideration of such unrealistic range for the variation of the plasma equivalent radius is done only to see its effect on the trend of the results obtained.

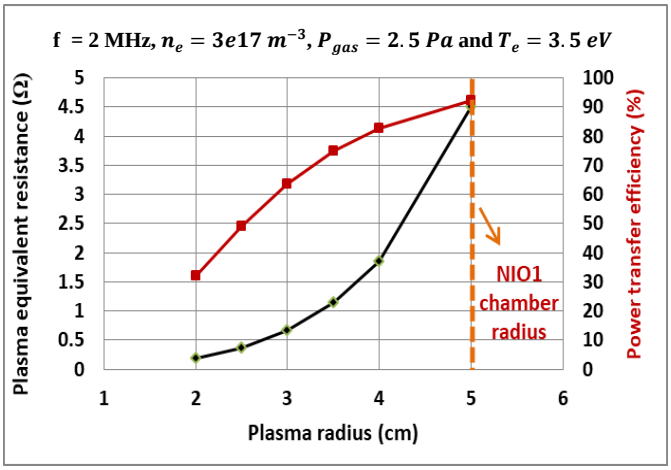

Figure 64: Plasma equivalent resistance and power transfer efficiency variation with plasma radius using multi-filament model for NIO1 ion source.

The reduction of the equivalent plasma radius within the chamber suggests a reduction in the PER and PTE. The PER reduces from about 4.5 Ω at 5 cm plasma radius to about 0.18 Ω at the plasma radius of 2 cm. The PTE decreases by 60% in reducing the plasma radius from 5 cm to 2 cm. In [88] an estimation of the load resistance (RF coil, passive structures and plasma) of 1.7 Ω is given for NIO1 ion source. This value is found at a plasma radius of 3.5 - 4 cm from the methodology presented in this paper.

6.7 Discussion

The developed methodology with transformer and the multi-filament model is applied to the NIO1 ion source. With the transformer model, it is found that the plasma equivalent resistance is about 9 Ω at the NIO1 operating frequency of 2 MHz. With the implementation of the multi-filament model, it is found that the plasma equivalent resistance reduces to about half the value obtained from the transformer model and the PTE reduces by 4 % for the typical values of NIO1 operation. These results seem to correspond to a more realistic description of the real phenomena. In addition, the assumption of a reduced equivalent plasma radius of about 25%, accounting in some way for a more realistic density profile leads to an evaluation of plasma equivalent resistance closer to the estimated value.

From both the models, it can be seen that the power transfer efficiency increases with the increase in operating frequency reaching maximum values around 10 MHz, thus indicating in this range the preferable operating frequency.

Early predictions/recommendations

This research activity was started with an aim to study and estimate the power transfer efficiency of the IC RF ion sources. For this a methodology was developed and applied to some existing ion sources; NIO1 and ELISE, operating with Hydrogen gas. The final goal is to apply the developed methodology to the driver of ITER NBI (or SPIDER/MITICA) in order to analyse its performance and explore possible improvements.

To study the ITER NBI case based on the results obtained from the application of the methodology, one should first overcome the present limitations and improve the methodology (this activity is ongoing), then apply the improved methodology to SPIDER ion source along with the validation of the methodology against the experimental results. However, since the driver of ITER NBI ion source (or SPIDER/MITICA) and the driver of the ELISE source are similar in many aspects, therefore, some early suggestions/predictions for achieving higher power transfer efficiency based on various plasma operating parameters and plasma heating mechanisms can be made from the knowledge gained so far from the application of the methodology to the simplified driver of the ELISE ion source.

- If the plasma electron density in the driver of SPIDER/MITICA is kept similar as that in the driver of the ELISE $\sim 10^{18}\ m^{-3}$, then the stochastic heating will most likely be present at gas pressure below 1 Pa. It is expected that stochastic heating will play a major role in plasma heating and eventually in the estimation of the power transfer efficiency.
- Similar to the results found for the simplified driver of ELISE, it is expected that geometric effects for calculating the skin depth should not be very significant in the simplified driver of SPIDER/MITICA/ITER NBI ion source as well, because they share almost the same dimensions for the driver. Although these geometric effects were found to be predominant in smaller ion source like NIO1.
- One of the main findings is that higher power transfer efficiency is seen when the working frequency is around 10 MHz instead of 1 MHz. This is found to be true for all electron densities (from low $5e16\ m^{-3} - 5e19\ m^{-3}$ (high)) and gas pressures (from $0.3 - 1\ Pa$) considered. It is expected that the same results will be obtained when the present methodology will be applied to the simplified driver of SPIDER ion source. So maybe it will be better to operate the future ion source at higher frequency of around 10 MHz.
- For the simplified driver of the ELISE ion source, it is seen that power transfer efficiency first increases, reaches a maximum ($\sim 5e17\ m^{-3}$) and then decreases with the increase in electron density; similar results are expected for the simplified driver of SPIDER/MITICA. Thus it is possible to choose the best operating density.

- To obtain higher power transfer efficiency it is suggested to work with the gas pressure as low as possible provided the plasma is ignited.

In addition, it will be interesting to explore the performances of the driver on the bases of different geometry. So far no particular analyses was performed in this direction, however, the results of the application of the methodology to two different driver geometry, NIO_1 and ELISE, show that it is possible to attain high power transfer efficiency although with different input parameters (operating frequency, electron density, type of gas, gas pressure). At present it difficult to generalize the results and say anything regarding the role of the driver geometry in particular. Further studies in this direction might lead to the estimation of the optimum driver geometry for ITER NBI.

Part 2: Activities on High Voltage Radio Frequency Test Facility (HVRFTF)

This part of the thesis presents the work done for the set-up of the HVRFTF at the Consorzio RFX, Italy. In the following chapters, at first the test facility is introduced and then the specific contributions in terms of characterisation of the coupled inductor, thermal analyses of the components inside the vacuum vessel and the analyses for the electromagnetic shielding are highlighted.

Chapter 7.

Introduction to the HVRFTF

The PRIMA project consist of two test facilities: MITICA and SPIDER (see section 2.3 for the description). A radio-frequency ion source is the main component in both the facility where the plasma is produced via inductive coupling by the RF coils wound around a driver case. At 1 MHz, a power of up to 100 kW is applied to the coil and with nominal plasma parameters it is expected to reach a voltage of about 12 kV. These ion sources are placed in vacuum and therefore high electric fields are expected to occur in the small gaps which exist between the RF coil and the case of the Driver (see Figure 22). These electric fields can then lead to possible breakdowns within the RF circuit [89]. From the finite element model analysis, an electric field of about 70 MV/m has been estimated in between these small gaps [41]. Therefore, there is an issue of voltage holding capability in different parts of the ion source and the associated RF circuit. Hence a test facility called High Voltage Radio-Frequency Test Facility (HVRFTF) was launched in 2014 to address this issue in operational environment similar to the one foreseen in SPIDER and MITICA. HVRFTF is now currently under operation in the premises of Consorzio RFX, with the first experimental test campaign started in 2016.

7.1 Aim of the HVRFTF

The goal of the HVRFTF is to characterize the dielectric strength in vacuum of the RF drivers at 1 MHz and to increase the understanding of the occurrence of the breakdowns on the RF drivers on NBI ion sources. The breakdown voltage depends upon various parameters like gas species, pressure, surface materials and on the geometry of the system. Therefore, it will be necessary to reproduce the real operating experimental conditions of the RF circuits of SPIDER and MITICA ion sources.

The ranges of the operating conditions (such as the electric field, voltage applied, gas type, pressure, materials etc.) for the HVRFTF will be wider than those foreseen in SPIDER and MITICA, as this will help to check some margins in the design of SPIDER and MITICA.

7.2 Design of the HVRFTF

The schematic diagram of the HVRFTF is shown in Figure 65. The aim of HVRFTF is to produce the High Voltage (up to 17 kV) with the radio frequency inductive capacitive resonant circuit supplied with a low voltage power amplifier. The produced high voltage will then be applied to the couple of electrodes (called Device Under Test (DUT)) of different shapes placed inside the vacuum vessel equipped with a pumping system capable of producing a pressure in a range of $10^{5} - 10^{-3}\ Pa$. A gas injector and a baking system are also present in the vacuum vessel. An EM shield is also provided, in order to block the electric and magnetic fields generated during the operation of the test facility.

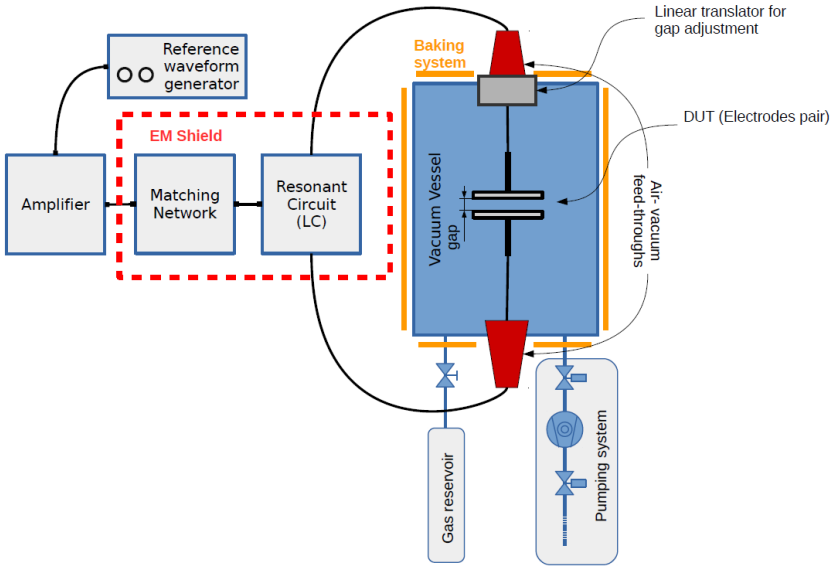

Figure 65: Schematic of the HVRFTF.

7.3 Contribution to the HVRFTF development

I gave a significant contribution towards the development of the HVRFTF both in terms of the analytical studies and experimental work. Three main tasks were performed which helped in the set-up of the test facility and eventually led to its successful operation. The tasks performed are as follow:

- RF power resonant circuits - Characterisation of the two solenoids coupled inductor
- Thermal analysis for the components installed in the vacuum vessel
    - EM shielding - Identification of the EM field and the safety measures to be taken, shielding calculation, design and test.

Chapter 8.

RF power resonant circuits – Characterisation of the two solenoids coupled inductor

The equivalent electrical scheme of the HVRFTF comprising of RF power matching network, resonant circuit and the vacuum vessel components is shown in Figure 66. To extract the maximum power from the amplifier and to obtain a desired voltage, it is necessary to design a suitable RF circuit with a good matching network. The matching network resonant circuit comprises of two capacitors –one series C_1 and one parallel C_2; and an inductor, see Figure 66.

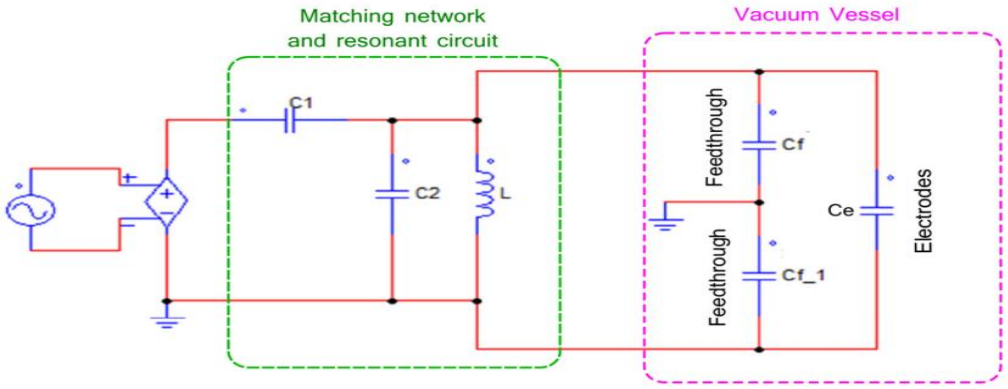

Figure 66: Electrical equivalent circuit of HVRFTF.

To design an inductor L, it is necessary to take into account not only the inductance but also its stray parameters which strongly influence its impedance (magnitude and phase) at RF. In this section a two solenoid coupled inductor called "I" is described whose characterisation was performed and which now also forms a part of the present resonance circuit in the HVRFTF.

The inductor "I" is composed of two copper solenoids called "I1" and "I2" which are mutually coupled and connected in parallel, see Figure 67. It is expected that this configuration should result in an inductance very similar among "I1", "I2" and I, but with reduced resistance, this is a result due to approximately equal current sharing between the two inductors. This concept of magnetically coupled solenoids connected in parallel was already tested on several small scale mock-up inductors, with positive results in terms of reduction of the stray resistance with respect to a single copper solenoid.

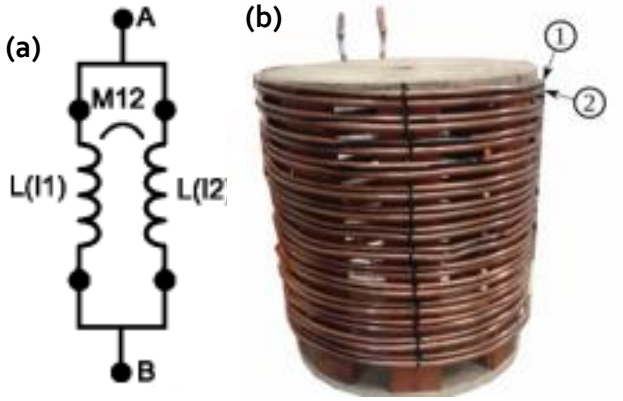

Figure 67: (a) Scheme and (b) photo of inductor "I".

Electrical characterisation of this two solenoid coupled inductor was done by taking the following measurements;

- Measure of the impedance of "I", "l_1", "l_2", "l_1+l_2" (i.e. l_1 connected in series with l_2) with an RLC bridge and with an impedance meter;
- Assessment of its stray resistance with a resonant circuit;
- Calculation of the voltage gain of the resonant circuit
- Measure of the current sharing when supplied with low voltage sinusoidal waveform at high frequency;

The aim of the tests was to verify the two solenoids have similar impedances, that the current sharing is good and that the stray resistance is reduced.

8.1 Geometry of the inductor "I"

The geometric characteristics of the inductor "I" are listed in Table 8 :

Table 8: Geometrical characteristics of inductor "I"

Parameter	**Value**
Inner diameter of inductor [cm]	49
Outer diameter of inductor [cm]	51.4
Diameter of inductor wire [cm]	1.2
Distance between two insulated inductor wires [cm]	0.1
Distance between the two turns of the same inductor wire [cm]	3.5
Number of turns	14

The two solenoids I1 and I2 are wound very close one to the other, as can be seen in Figure 67. The air gap between two turns is large enough to reduce the turn to turn stray capacitance and to assure electrical insulation.

8.2 Calculation of the electrical parameters

The electrical model (developed at Consorzio RFX [90]) of the solenoid I1 (or I2) predicts an effective inductance of **65.9 µH** and an effective stray resistance of **266 mΩ**.

Under the assumption of perfect coupling the mutual inductance between the two solenoids can be calculated using the formula shown below:

$$M_{12} = \frac{\mu_0 N_1 N_2 A}{l} \tag{97}$$

Where, $N_1$and N_2 are the number of turns of the two solenoids, A is the area of the inductor $A = \pi r_0^2$, r_o is the radius of the coil, l is the length of the inductor. This equation for the mutual inductance is valid only if the ratio (l/r_0) of the inductor is very large. For small inductors, the above equation gets modified as shown in the equation below:

$$M_{12}^{*} = \alpha M_{12} \tag{98}$$

Where, α is the Nagaoka coefficient and is given as:

$$\alpha = \sqrt{1 + \left(\frac{1}{4\left(\frac{l}{2r_0}\right)^2} \right)} - \frac{1}{2\left(\frac{l}{2r_0}\right)} \tag{99}$$

The calculated value of M_{12} (with the correction coefficient) is $\mathbf{62.9\ \mu H}$.

8.3 Set up for the measurement

The inductor is placed vertically on a table with the surrounding structures at more than 1 m (except the measuring equipment). The impedance and inductance measurements are taken directly on the inductor while a resonant circuit is used to derive the stray resistance of the inductor (see Figure 68).

8.3.1 Measuring equipment

8.3.1.1 *Impedance meter*

The impedance of the inductor as a function of frequency has been measured with the impedance meter HP4194A (see Table 9 for the main characteristics), using the "impedance"

port (frequency range 100 Hz - 40 MHz) which has floating terminals. The data has been acquired with a PC via GPIB port, stored in a csv file and analysed with Python scripts.

Table 9: Main characteristics of impedance meter HP4194A

Range	Min	Max	Resolution
Frequency	100 Hz	40 MHz	1 mHz
Impedance	10 mΩ	100 MΩ	100 μΩ

8.3.1.2 *LCR meter*

HP Model 4262A was used and it can measure L, C and R at the frequencies of 120 Hz, 1 kHz and 10 kHz.

8.3.1.3 *Oscilloscope*

Yokogawa DL1740 and a voltage probe were used.

8.3.1.4 *Current probe and amplifier*

Current probe used was Tektronix TCP312. Amplifier used was Tektronix TCPA300.

8.4 Resonant circuit for resistance evaluation

The matching and the resonant circuit shown in Figure 66 have been analyzed and the input port AB (see circuit of Figure 68) is connected to the impedance meter. The inductor under test is indicated with L and its stray resistance is indicated as R_L (stray capacitances are not shown). The rated capacitances of the capacitors used in the circuit are $C_s = 25\,pF$ and $C_p = 250\,pF$; the measured values of the capacitances are $C_s = 28\,pF$ and $C_p = 248\,pF$, and these values are used to evaluate the stray resistance. The impedance of the connections indicated as Co1 and Co2 are neglected.

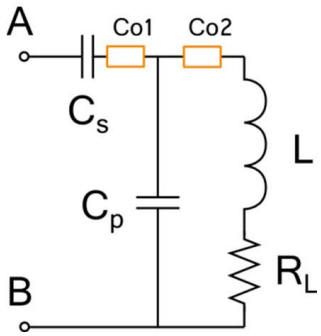

Figure 68: Resonant circuit used to evaluate R_L.

From the measurement of the impedance of the circuit, it is possible to derive impedance of the inductor $\dot{Z}_L$ and then its resistance R_L at the resonance frequency by the following:

$$\dot{Z_L} = \left[\left(\dot{Z_{AB}} - j\frac{1}{\omega C_S}\right)^{-1} + j\omega C_p\right]^{-1} \quad (100)$$

R_L is the real part of $\dot{Z}_L$. It is also possible to derive the inductance from the imaginary part of $\dot{Z_L}$.

8.5 Measurements

With the aim to identify the inductor L characteristics different set up for the measurements of "I", I1, I2 and I1+I2 are analyzed and reported in the following sections. In particular the impact on the impedance measurement of the grounding of either one of the inductor terminal is evaluated, in order to take into account different connections to ground in the final circuit.

8.5.1 Measurement of the inductance of the inductor "I"

The inductance of the inductor "I", I1, I2 and I1+I2 has been measured using the LCR meter described in paragraph 8.3.1 , at the three available frequencies (120 Hz, 1 kHz, 10 kHz), see Table 10. A 4-wires setup was used, the inductor terminals where left floating since the reading was not possible with a grounded terminal.

Table 10: Inductance measured with the RLC bridge

Frequency	120 Hz	1 kHz	10 kHz
Inductance of I1 [µH]	69	67.8	66.6
Inductance of I2 [µH]	70	68.4	67
Inductance of I [µH]	68	66.5	65.6
Inductance of I1 + I2 [µH]	270	266	263

It is easy to evaluate the mutual inductance M_{12} from the measurements on the solenoids "I1" and "I2" and from the inductance measured when "I1" and "I2" are connected in series by the following formula:

$$M_{12} = \frac{L(I_1 + I_2) - L(I_2) - L(I_2)}{2} \quad (101)$$

The results of the calculations are reported in Table 11.

Table 11: Calculated mutual inductance

Frequency	120 Hz	1 kHz	10 kHz
M12 [µH]	65.5	64.9	64.7

Since l1 inductance differs from l2 inductance and both differs from M12 the current will not be perfectly shared between the two solenoids composing inductor "l", so the stray resistance of inductor "l" will not be half of the stray resistance of l1 or l2.

8.5.2 Measurement of the impedance of the inductor

8.5.2.1 *Floating terminals*

The measurements are done with an impedance meter and the plots of the impedance (modulus and phase) of the inductor "l" (where "l1" and "l2" are in parallel), solenoid "l1" and "l2" are shown in Figure 69.

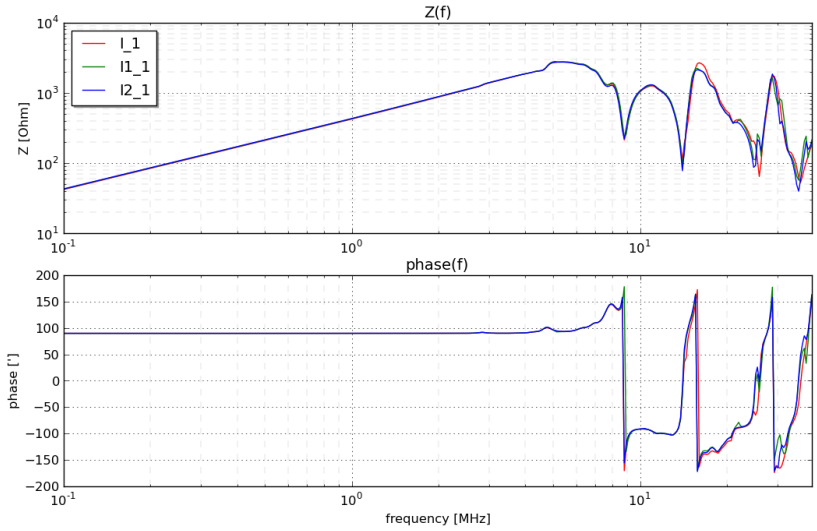

Figure 69: Measured impedance and phase of the inductor with floating terminals.

Table 12: Measured impedance and inductance with floating terminals

Inductor	Natural resonance frequency [MHz]	Impedance [Ω] @ 1 MHz	Inductance [µH] @ 1MHz
l1	8.9	416.1	66.2
l2	8.8	418.5	66.6
l (l1 and l2 in parallel)	8.9	410.7	65.4

8.5.2.2 *Grounded terminal*

The plots of the impedance (modulus and phase) of the solenoid "l1" with floating terminals (red curve) and with one terminal grounded (green curve top terminal grounded, blue curve bottom terminal grounded) are shown in Figure 70.

The plots of the impedance (modulus and phase) of the solenoid "I2" with floating terminals (red curve) and with one terminal grounded (green curve top terminal grounded, blue curve bottom terminal grounded) are shown in Figure 71.

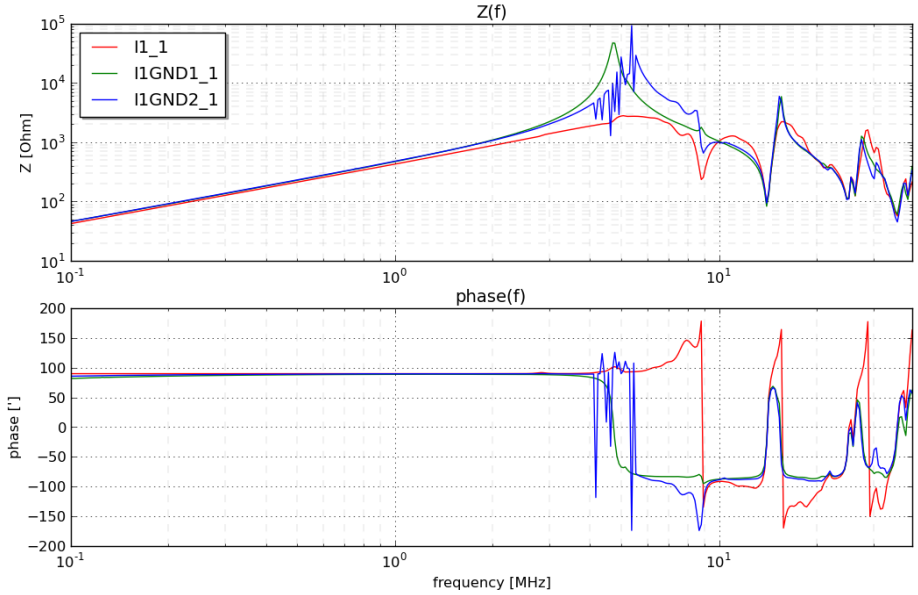

Figure 70: Measured impedance and phase of the solenoid I1 with floating terminals (red curve), with top terminal grounded (green curve) and with bottom terminal grounded (blue curve).

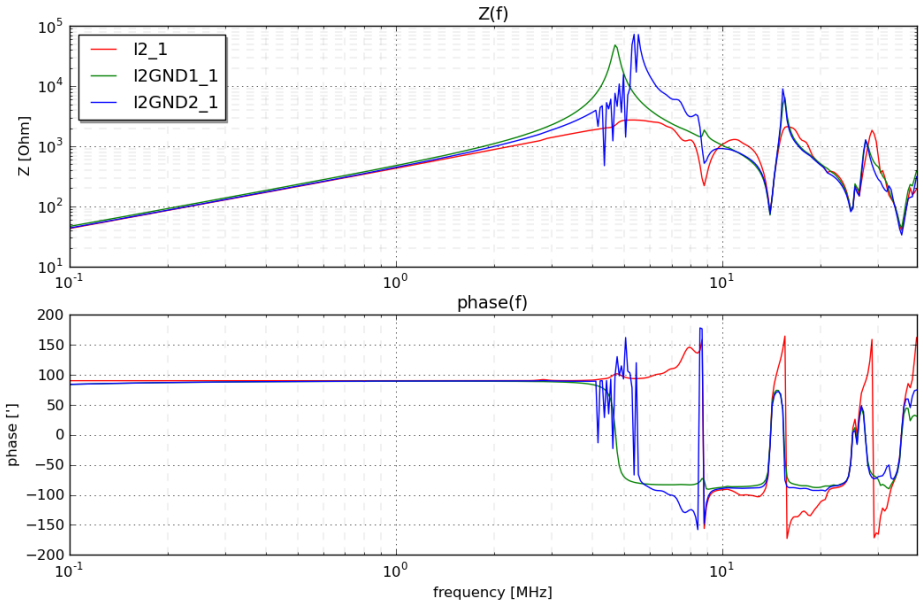

Figure 71: Measured impedance and phase of the solenoid I2 with floating terminals (red curve), with top terminal grounded (green curve) and with bottom terminal grounded (blue curve).

The plots of the impedance (modulus and phase) of the inductor "I" with floating terminals (red curve) and with one terminal grounded (green curve top terminal grounded, blue curve bottom terminal grounded) are shown in Figure 72.

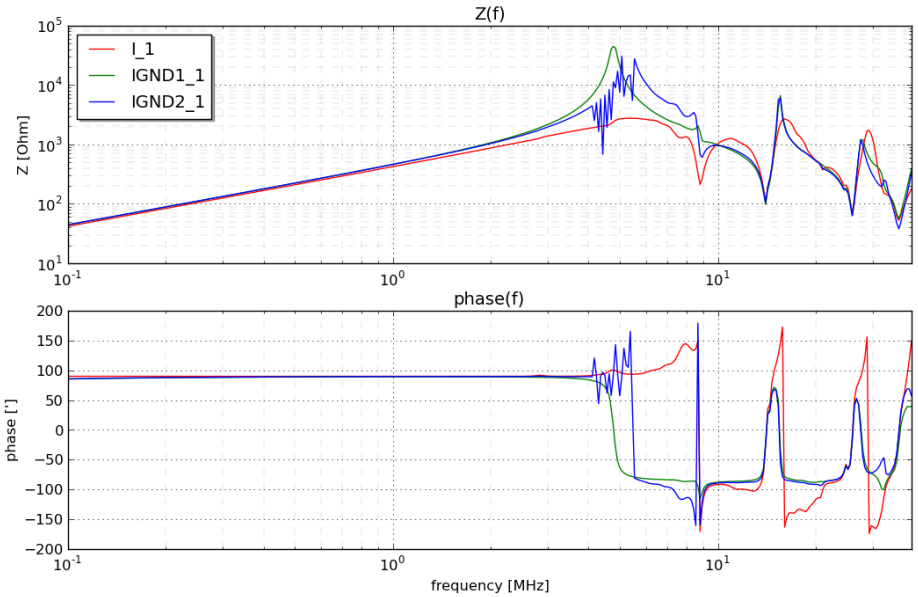

Figure 72: Measured impedance and phase of the inductor "I" with floating terminals (red curve), with top terminal grounded (green curve) and with bottom terminal grounded (blue curve).

The summary of the measurements are reported in Table 13.

Table 13: Measured impedance and inductance with a grounded terminal

Inductor	Natural resonance frequency [MHz]	Impedance [Ω] @ 1 MHz	Inductance [μH] @ 1MHz
I1 Top terminal grounded	4.7	451.6	71.9
I1 Bottom terminal grounded	5.5	470.0	74.8
I2Top terminal grounded	4.7	454.2	72.3
I2 Bottom terminal grounded	5.5	462.0	73.5
I (I1 and I2 in parallel) Top terminal grounded	4.7	462.2	73.6
I Bottom terminal grounded	5.4	460.0	73.2

The inductance of the inductor "I" have an increment of 7.8 - 8.2 μH, corresponding to 12-12.5 %, with respect to the inductance shown with floating terminals. The difference between the values of inductance obtained from measurements with grounded terminal and floating terminals could be due to the stray capacitances.

8.5.3 Measurement for the evaluation of the resistance of the inductor of the resonant circuit with floating terminals

The impedance meter has been connected to the port AB of the circuit of Figure 68, the measured impedance (modulus and phase) at port AB for the three cases of the inductor "I" (where "I1" and "I2" are in parallel), solenoid "I1" and "I2" are reported in Figure 73. From the graphs it can be seen that the modulus shows a minimum and a phase transition takes place from $-90°$ to $+90°$, this happens at the resonant frequency of the circuit where the sum of the reactance of the circuit goes to zero, i.e., $X_L + X_C = 0$. Here $X_L = \omega L$ and $X_C = -\frac{1}{\omega C}$, are the inductive and the capacitive reactance respectively. Thus the resonant frequency occur when $\omega = \frac{1}{\sqrt{LC}}$

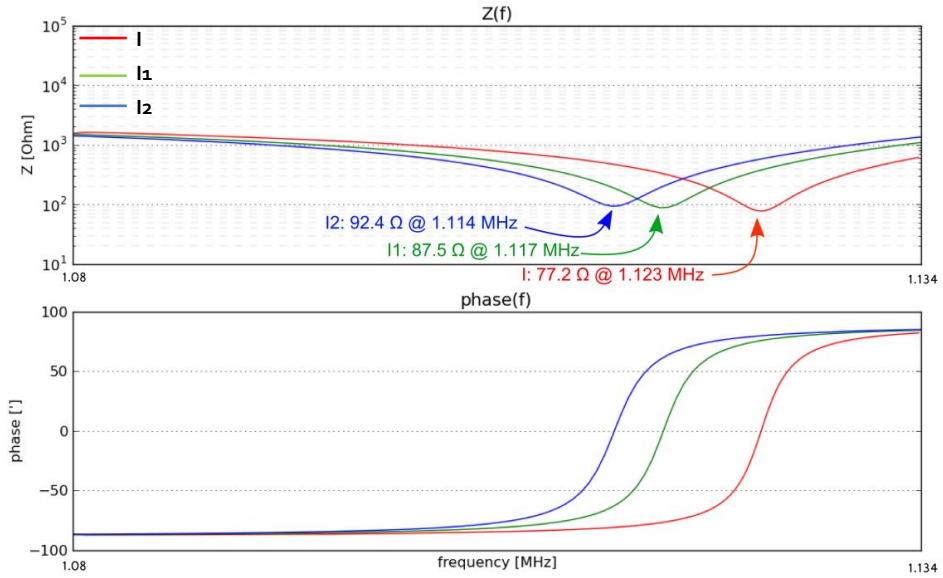

Figure 73: Measured impedance and phase seen from port AB with floating terminals.

Using the method described in section 8.4 it is possible to calculate the stray resistance of the inductor.

Table 14: Calculated stray resistance with floating terminals

Circuit	Resonance frequency (fr) [MHz]	Input Impedance [Ω]/argument [°] @ fr	Inductance [µH] @ fr	Resistance [Ω] @ fr
Resonant circuit with I1	1.117	87.8 (∟-7.35°)	72.5	0.86
Resonant circuit with I2	1.114	93.0 (∟-1.43°)	72.9	0.92
Resonant circuit with I	1.123	77.3 (∟-7.36°)	71.7	0.76

The inductance value derived from the measurement with the resonant circuit (see paragraph 8.4) is higher than the value derived from the measurement on the inductor alone: about **72 µH** versus **66 µH**. This difference can be due to the two different electrical systems (due to the stray capacitances and electrical connections).

The resistance value is similar for I1 and I2, it slightly decreases for the inductor "I" when the two solenoids are connected in parallel.

8.5.4 Calculation of the voltage gain of the resonant circuit with floating terminals

It is also possible to calculate the expected voltage gain, defined as the ratio between the voltage across the inductor and the voltage applied to the resonant circuit at port AB, using the measured impedance at port AB and the value of the series capacitor's capacitance:

$$Gain = \left|\frac{Z_{AB} - Z_{CS}}{Z_{AB}}\right| \qquad (102)$$

The expected gain as a function of frequency is reported in Figure 74.

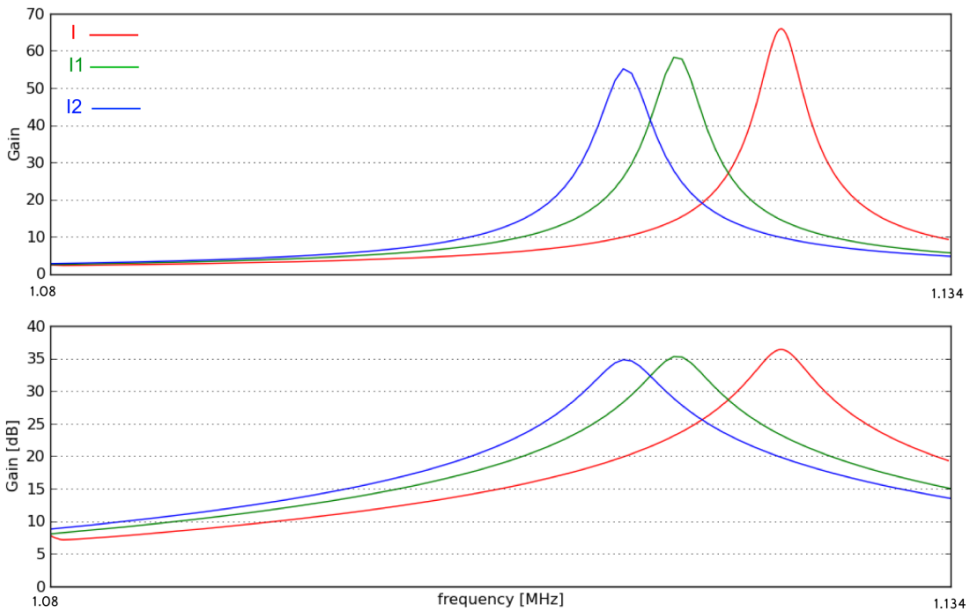

Figure 74: Gain of the resonance circuit with floating terminals.

Once the gain of the circuit and the impedance seen at port AB are known (See Table 14 for floating terminals measurements), it is possible to calculate the required voltage at the port AB and the RF power to reach 17 kV on the inductor L (in this case the target voltage to be reached with the resonant circuit, higher values are taken, in order to keep the margin on the design of HVRFTF):

$$required\ voltage = \frac{17000}{Gain} \tag{103}$$

$$required\ power = \left(\frac{required\ voltage}{Input\ impedance}\right)^2 \cdot \text{input impedance} \cdot \cos(argument\ of\ input\ impedance) \tag{104}$$

The gain is increased by 1.1 - 1.6 dB (see Table 15) thanks to the use of the "coupled inductor" concept, and the power required is reduced to about 11.3 – 16.3%.

Table 15: Gain of the resonance circuit and required power with floating terminals

Inductor	l1	l2	l
Resonance frequency [MHz]	1.117	1.114	1.123
Gain [-]	58.2	55.2	65.9
Gain [dB]	35.3	34.8	36.4
Required voltage [V] to reach 17 kV	292	308	258
Required power [W] to reach 17 kV	963	1020	854

8.5.5 Measurement for the evaluation of the resistance of the inductor of the resonant circuit with grounded bottom terminal

Only the measurements with bottom terminal grounded are reported in this paragraph, since in the actual circuit the bottom terminal is grounded. The impedance meter has been connected to the port AB of the circuit of Figure 68, the measured impedance is reported in Figure 75.

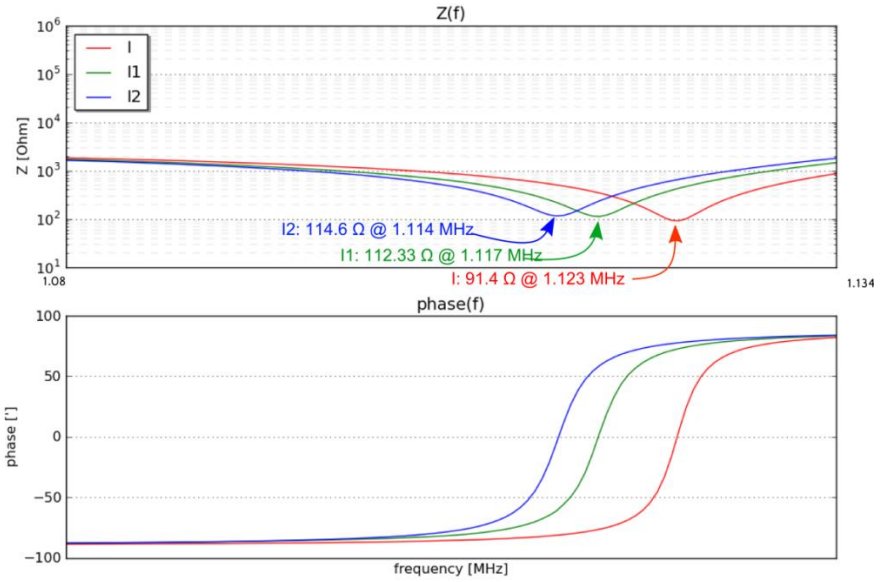

Figure 75: Measured impedance and phase seen from port AB with bottom terminal grounded.

Using the method described in section 8.4 it is possible to calculate the stray resistance of the inductor. In this case (with the bottom terminal grounded, corresponding to the point of the circuit where the voltage source is grounded) the inductance value derived from the measurement with the resonant circuit (see paragraph 8.4) is similar to the value derived from the measurement on the inductor alone: about 72 µH.

The resistance value is similar for I1 and I2, it slightly decreases when the two solenoids are connected in parallel. With a grounded terminal the resistance of the inductor "I" increases of about 18 % with respect to the case of floating terminals.

Table 16: Calculated stray resistance with grounded terminal

Circuit	Resonance frequency (fr) [MHz]	Impedance [Ω]/ argument [°] @ fr	Inductance [µH] @ fr	Resistance [Ω] @ fr
Resonant circuit with I1	1.117	112.3	72.6	1.104
Resonant circuit with I2	1.114	114.6	72.9	1.130
Resonant circuit with I	1.123	91.4	71.8	0.896

8.5.6 Calculation of the voltage gain of the resonant circuit with grounded bottom terminal

The expected gain as a function of frequency is reported in Figure 76.

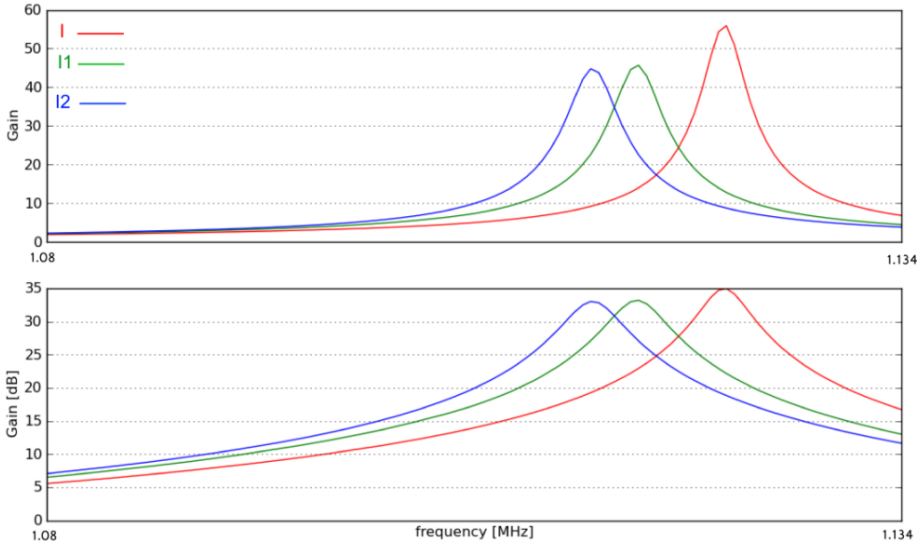

Figure 76: Gain of the resonance circuit with bottom terminal grounded.

Table 17: Gain of the resonance circuit and required power with grounded terminal

Inductor	l1	l2	l
Resonance frequency [MHz]	1.117	1.114	1.123
Gain [-]	45.7	44.8	55.9
Gain [dB]	33.2	33.0	34.9
Required voltage [V] to reach 17 kV	372	379	304
Required power [W] to reach 17 kV	1232	1253	1011

As shown in Table 17, the gain is increased by 1.7 - 1.9 dB thanks to the use of the "coupled inductor" concept, and the power required is reduced to about 17.9 – 19.3 %.

8.5.7 Measurement of the current sharing with grounded bottom terminal

The inductor has been supplied with a sinusoidal waveform with amplitude of 10 V (rms) at 300 kHz and at 1 MHz, with bottom terminal connected to ground (corresponding to the point of the circuit where the voltage source is grounded).

The total current as well as the current flowing through each branch (solenoids l1 and l2) has been measured. The results are reported in Table 18.

Table 18: Current sharing measurement

Frequency [MHz]	Voltage applied from the amplifier V_{rms} (V)	Branch	Current measured [mA]	%
0.3	10.1	l	$I_T = 71.2$	100
		l1	$I_1 = 40$	56
		l2	$I_2 = 28.9$	41
1	10.2	l	$I_T = 21.5$	100
		l1	$I_1 = 12.37$	58
		l2	$I_2 = 8.6$	40

The total current is not equal to the sum of the current of the two branches; the error is within the DC accuracy of ±3% of the current probe. The current is not equally shared between the two solenoids, this may be the reason for which the effective resistance of the inductor "l" is not half of the resistance of one solenoid.

8.6 Discussion

The summary of the results obtained from the measurements and calculations is presented in Table 19. The calculated self-inductance is close to the one measured on the

inductor alone with floating terminals (65.9 μH and 65.4 μH respectively) while its stray resistance is about three times larger than the calculated one.

The mutual inductance M12 from the measurement has been estimated to be 65.0 μH, which is about 3% more than what estimated analytically.

The inductance value derived from direct measurement on the inductor with floating terminals is lower than the inductance value derived from the measurement on the resonant circuit with floating terminals. The difference is about 9%. However, no significant difference is observed between the two inductance values when one of the terminals is grounded.

Table 19: Summary of the results obtained from measurements and calculations

Inductor	Resonance frequency (fr) [MHz]	Inductance measured directly [μH] @ 1 MHz	Inductance derived with method of paragraph (8.4) L[μH] @ fr	Resistance derived with method of paragraph (8.4) RL [Ω] @ fr	Gain [dB] @ fr	Required power [W]
I1 Floating terminals	1.117	66.2	72.5	0.86	35.3	963
I2 Floating terminals	1.114	66.6	72.9	0.92	34.8	1020
I Floating terminals	1.123	65.4	71.7	0.76	36.4	854
I1 bottom terminal grounded	1.117	74.8	72.6	1.104	33.2	1232
I2 bottom terminal grounded	1.114	73.5	72.9	1.130	33.0	1253
I bottom terminal grounded	1.123	73.2	71.8	0.896	34.9	1011

The measured inductance of the two solenoids I1 and I2 is similar and it is similar to the inductance of the inductor "I", at the same conditions.

Increase in the gain and reduction in the power required to reach the maximum voltage is higher in the inductor "I" when one terminal is grounded in comparison with the floating terminals.

Chapter 9.

Thermal analysis for the components installed in the vacuum vessel

Three couples of circular electrodes of different diameters have been studied to perform the experiments in the HVRFTF. During the experiments foreseen to be performed in the HVRFTF, that the steel rods supporting the electrodes present inside the vacuum vessel (see Figure 77) may get heated due to the current flowing through them at the frequency of 1 MHz. Due to the joule heating effect this may also lead to an increase of the temperature (more than the maximum allowed temperature) in the metallic part of the steel rods in the feed-through.

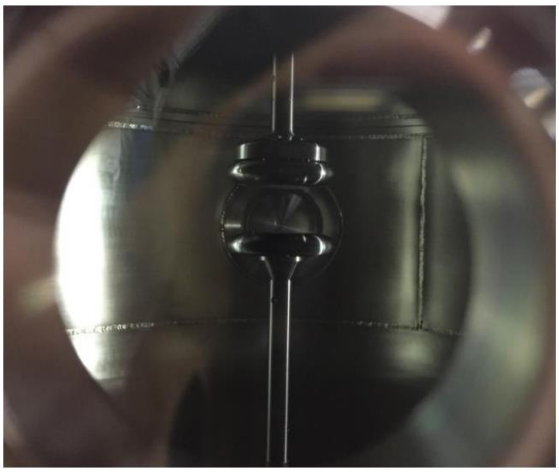

Figure 77: Photo of the electrodes.

This maximum rod temperature is limited by the electrical feed-through component since it has a brazed ceramic-metallic joint and the thermal expansion of the heated metal can mechanically stress the surrounding ceramic and finally damage the feed-through. In this chapter, the analysis for the time required to heat the steel rods to a certain limit is provided. As a first approximation, the idea is to conservatively limit the temperature difference to about 40 K (condition acceptable for the feed-through) with respect to the ambient room temperature.

In case, the time required to reach 40 k for the steel rods is found to be less than that of reasonable experimentation time (which is of the order of few minutes or at maximum 1 hour

as in the case of SPIDER), then there is a possibility to replace the steel rods with copper rods because copper has better thermal properties (higher density along with lower heat capacity and resistivity) than steel. Therefore, in this chapter, the analysis for copper rods for comparison and possible replacement of the existing steel rods is also present.

9.1 Analyses of the rod heating

The analysis is carried out considering an adiabatic process. Since the experiments will take place in vacuum we will not take into account the effect of convection. A preliminary calculation was done in order to analyse the effect of conduction and it was found that the difference between the surface temperature and the bulk temperature of the steel rod was negligible. Therefore, the effect of conduction was neglected. To be more conservative, the effect of radiation is also neglected.

9.1.1 Heating power and temperature rise time calculations

The power loss due to the current 'I' flowing in the rod is given by:

$$P_{loss} = RI^2 \tag{105}$$

Here R is the resistance offered by the rods and can be calculated by the following equation:

$$R = \frac{\rho l}{A_{eff}} \tag{106}$$

'ρ' is the resistivity (Ωm) and is used to calculate the conductivity of the material.

$$\sigma = \frac{1}{\rho} \tag{107}$$

'l' is the length of the rods, whereas A_{eff} is the effective area (used by the current to flow, i.e. taking into account the effect of skin depth), calculated as follow:

$$A_{eff} = A_T - \pi\left(\frac{D}{2} - \delta\right)^2 \tag{108}$$

Here, D is the diameter of the steel rod, A_T is the total area and 'δ' is the skin depth.

$$\delta = \frac{1}{\sqrt{\pi \sigma f \mu_0 \mu_r}} \tag{109}$$

μ_o is the magnetic permeability of free space and μ_r is the relative permeability.

Considering negligible thermal exchange (radiation and conduction) between the rod and the surrounding component, the rod experiences an adiabatic heating. In this condition, the

amount of power ($P_{allowed}$) needed to raise the temperature of the rods of a particular amount ΔT within a Δt time is given by

$$P_{allowed} = \frac{C_P m \Delta T}{\Delta t} \quad (110)$$

Here, C_P is the specific heat capacity in (J/kgK). 'm' is the mass of the material and is calculated as $m = d \cdot v$. 'd' is the density of the material (kg/m^3) and v is the volume and is given by $v = l \cdot A_T$

Equating the power loss P_{loss} and the allowed power $P_{allowed}$ we can calculate the time Δt required to raise the rod temperature of ΔT (in adiabatic condition).

$$P_{loss} = P_{allowed} \quad (111)$$

$$\Delta t = \frac{C_P \, d \, A_T \, A_{eff} \, \Delta T}{\rho I^2} \quad (112)$$

9.1.2 Parameters used to perform the calculations

Considering the adiabatic heating, the temperature of the rod has been analysed for the two different materials - steel and copper, with the electrical and physical parameters listed in Table 20.

Table 20: Parameters used to perform calculations

Material	Steel 304L	Copper
Density 'd' [kg/m^3]	7900	8950
C_P [J/kgK]	500	384.4
ρ [Ωm]	71.3 x 10^{-8}	1.68 x 10^{-8}
Diameter of rod 'D' [m]	0.024	0.024
μ_o [H/m]	4π x 10^7	4π x 10^7
μ_r	1.02	1
Room Temperature [K]	293	293
Frequency [MHz]	1	1

9.1.3 Resistivity variation with temperature

The effect of variation in resistivity with the change in temperature is also considered. The resistivity variation with temperature for steel 304L and copper are taken from the reference [91] and [92] . This is also represented graphically in the Figure 78 and Figure 79. The 'x' axis corresponds to the temperature (K) and the 'y' axis corresponds to the resistivity (Ωm) in the equations displayed in these graphs. These equations are used to calculate the resistivity and eventually the time required to heat the rod to the temperature difference of 40 K.

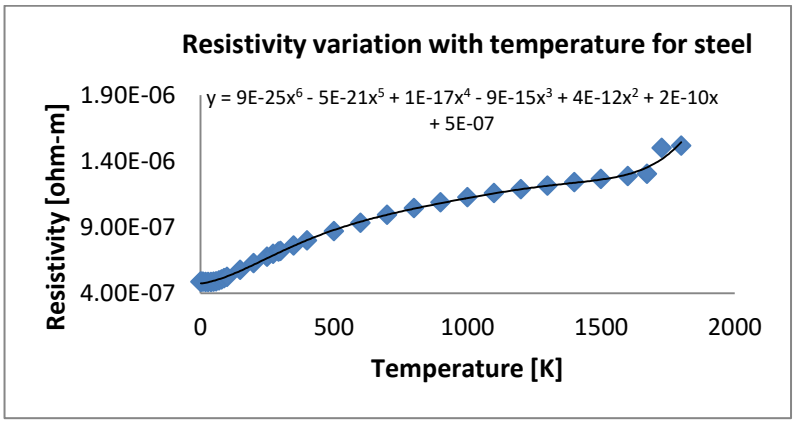

Figure 78 - Resistivity variation with temperature for Stainless steel 304L.

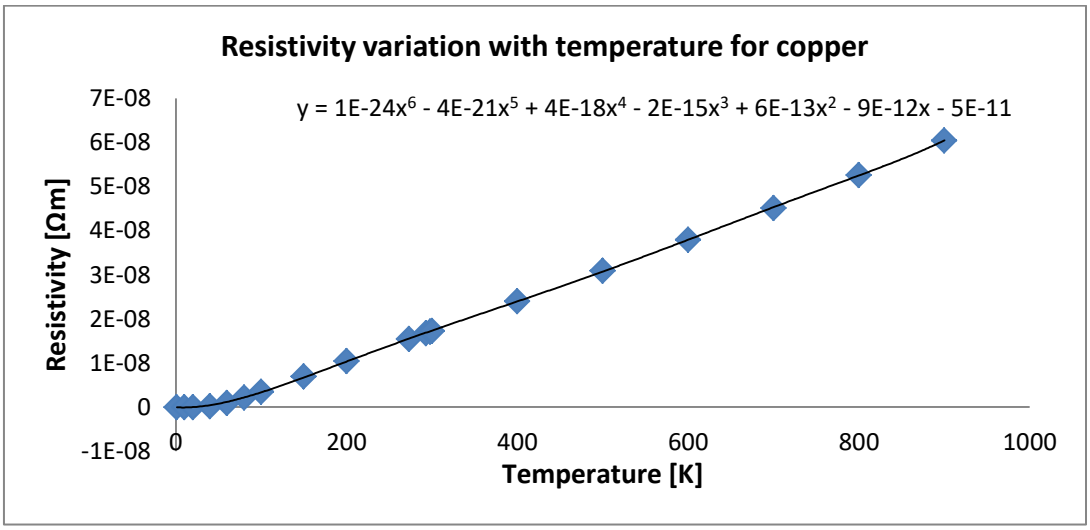

Figure 79 - Resistivity variation with temperature for Copper.

9.2 Calculation of the heating time of the rod

At present three different pair of circular electrodes (machined with Rogowski profile) with the diameter of 300 mm, 180 mm and 108 mm respectively are available at the RF laboratory. The electrodes can be mounted on the feedthroughs and the distance between the electrodes can be adjusted to match the test requirements. The capacitance C_e in Figure 66 represents the capacitance between the electrodes which can be calculated with the help of a simple formula:

$$C_e = \frac{\varepsilon_0 A}{d} \tag{113}$$

Taking the distance between the two electrodes to be $d = 3mm$ and $A = \pi r^2$, where r is the radius of the electrodes, the capacitance C_e of the different couples of electrodes are calculated and reported in Table 21. The current flowing through the three pair of circular

electrodes is different because of the different capacitances offered by the different electrodes.

Taking into account all the parameters described in section 9.1.2, the analyses of the rise time of the rod temperature was done using equations described in section 9.1. A MATLAB® code is written to perform the analysis. The dependence of the resistivity of the material with the temperature is considered. With an initial condition of 293 K, the initial resistivity of the material is calculated. The code calculates the time to reach the desire temperature difference of rod (40 K) by updating the resistivity value with the time step of 'dt =1 s'. In order to verify the results obtained, different time steps 'dt' were also considered. However, no change was observed in the total time to heat the rod to reach the temperature difference of 40K.

The time duration to increase the temperature of the rod by 40 K as a function of the current flowing through the electrodes is shown in Figure 80for the two materials copper and stainless steel.

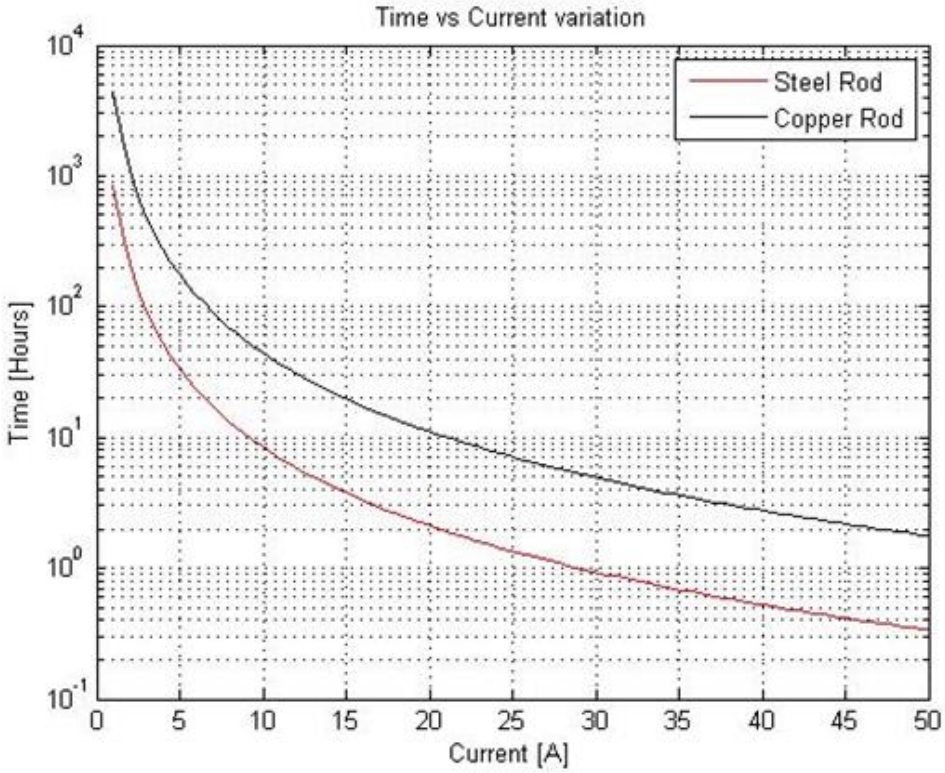

Figure 80 - Time duration to increase the rod temperature by 40K, as a function of the current flowing in the electrodes.

In Table 21 we can see the results obtained for the three different electrodes available to perform the experiment.

Table 21: Calculation of the time required to heat the rods by 40 K

	Electrodes		
	Large	**Medium**	**Small**
Electrode Diameter (mm)	300	180	108
Capacitance(pF)	208.4	75	27
Current (A)	39	14	5
Time (Hr) (SS 304L) for dT = 40 K	0.55	4.37	34.16
Time (Hr) (Copper) for dT = 40 K	2.89	22.95	179.5

9.3 Discussion

It is observe that:

- In case of the smallest electrodes (with the current of 5 A), it takes approximately 34 hours to raise the temperature of the steel rods by 40 K from the ambient room temperature (293 K).
- Even with the largest electrodes (with the current of 39 A), the time required to raise the temperature of the steel rods by 40 K is approximately 33 minutes.

Since for the first experiments in HVRFTF, the smallest electrodes will be used, it is acceptable to use the steel rods as it is, i.e. without any replacement because the rise time is much higher than the maximum experimentation time (which is 1 hour as that in SPIDER).

In case of maximum experimentation time of 1 hour, it is not advisable to use the electrodes with the largest diameter because the rise time will be lesser. So in this case, the possibility to replace the steel rods with copper should be considered since the rise time is approximately 3 hours in case of copper.

Chapter 10.

Electro-magnetic (EM) shielding

This chapter presents the evaluation of electric and magnetic field near all possible electromagnetic sources of the HVRFTF during the first experiment with RF power. The maximum test voltage foreseen for the study presented in the following is 30 kV peak, value presenting significant margin with respect to the planned experimental program of the HVRFTF (the target peak voltage is in fact 21.2 kV). The 30 kV value is also the maximum allowed for a classified source of ionizing radiation to be operated without permission from the authority [93]. Considering the space available for the laboratory and the Italian regulations (see section 10.2) for the general public as the reference limit on electric [94] and magnetic fields [95], the performance requested for the EM shielding are calculated.

It is specified that this is a qualitative analysis since the matching resonant circuit was not finalized when these calculations were done; a reference matching resonant circuit was chosen (similar to the one described Chapter 8) and the geometry of the inductor used is also the same as described in Chapter 8 except the point that only single layer inductor have been taken into account for the calculation. It is also underlined that the simulations consider only the inductor in free space (no walls, floor, etc. have been considered).

The aim of the work is to estimate the level of EM field generated by the HVRFTF on the basis of the available circuit data and simplified assumptions, in order to design and verify the effectiveness of suitable shielding, capable to assure the respect of the reference limits. The evaluation of the compliance with the limits is also done via proper in house measurements.

10.1 Description of the sources of EM field

There are two main sources of electromagnetic radiations during the experiment:

- The radio frequency matching resonant circuit, and in particular the inductor.
- The "RF load": the connections to the vacuum chamber, the vacuum chamber and the electrodes (see Figure 66 for reference).

10.1.1 Resonant circuit components

For this study the resonant circuit proposed in Chapter 8 for the first tests with HVRFTF have been considered. This is composed of a single layer solenoid with an inductance L = 80

μH and two capacitors C1 = 25 pF and C2 =250 pF. The geometry of the inductor is same as described in Table 8 but with one single layer.

10.1.2 RF Load

The main components that constitute the load for the resonant circuit are:

- The vacuum vessel and the feed-throughs
- The electrodes
- The cable connections

The layout of the cable connections was not defined when this analysis was done, but for the scope of the present analysis the evaluation of EM field produced by the electrodes and the vacuum vessel is sufficient.

10.1.2.1 *Vacuum vessel and the feedthroughs*

The vacuum chamber is equipped with two high voltage feedthroughs to mechanically sustain and polarize the electrodes under test. Details on the geometry and the material of the vacuum vessel and the feedthroughs can be found in paragraph 10.3.2.1

From the electrical point of view the vacuum chamber is a grounded structure isolated from the electrodes by the feedthroughs.

Each feedthrough introduces a capacitance to the vessel and these are taken into account in the equivalent RF circuit with C_f and C_{f1} as reported in Figure 66.

It is worth noting that the feedthroughs are equipped with an electric screen on the vacuum side, in order to control the electric fields near the connections to the electrodes. The presence of the electrostatic screens highly affect (increase) the values of C_f and C_{f1}. These capacitances have been calculated by means of simulations and also measured and they are in the order of 32 pF.

10.1.2.2 *Electrodes*

For the analyses, the same configuration of the electrodes is considered as defined in section 9.2.

10.1.3 Operational regime for the test

With the components aforementioned and the hypothesis of the operating conditions:

• Frequency f = 1 MHz;

• Peak voltage applied to the electrodes 30 kV (21.3 kV rms);

It is possible to calculate the current through the inductor and capacitors in the resonant circuit and on the electrodes in the vacuum vessel, using the following relations:

• For inductor: $V \approx X_L I_L$ and $X_L = \omega L$; $\omega = 2\pi f$ the peak current flowing through the inductor is 60 A

• For the parallel capacitor C_2 in the matching network: $V \approx X_C I_C$ where $X_C = 1/\omega C_2$. The peak current through the capacitor is 47 A.

The current through the electrode branch in the vacuum vessel is calculated to be 39 A, 14 A and 5 A for large, medium and small electrodes respectively assuming the value of capacitances reported in paragraph 9.2.

10.2 EM field limits

According to the Italian regulation the maximum value allowed for electric and magnetic fields are different for general public and workers in the laboratory. As can be found in references [94] and [95], these limits depend on the frequency of the EM radiation. Since the limits for the general public are lower than the ones for workers, the first will be used as reference. The operating frequency for the HVRFTF will be very close to 1 MHz; the Italian regulation for general public at this frequency suggests maximum exposition value of **87 V/m** for the electric field intensity and **0.73 A/m** for the magnetic field intensity.

10.3 EM field calculation

The work reported in the following sections aims at defining the ambient conditions for the personnel in the laboratory during operation. The level of the electric and magnetic field due to the EM source are calculated and the possible provisions to fulfil the requirements reported in paragraph 10.2 are then described.

10.3.1 Electric and magnetic field generated by the inductor of the resonant circuit

10.3.1.1 *FEM model*

The evaluation of the electric and magnetic field near the inductor was done by developing a dedicated FEM model built with COMSOL Multiphysics®. The case studied considers the inductor in free air where the effect due to the surrounding structures is disregarded. A simplified model is assumed, which considers the inductor in 2D axisymmetric and a large circular simulation domain with 10 m radius (see Figure 81). The latter assumption is done to apply reasonable far field boundary condition at the external frontier. The simulations are then performed by constructing suitable triangular mesh around the inductor, as can be seen in Figure 82.

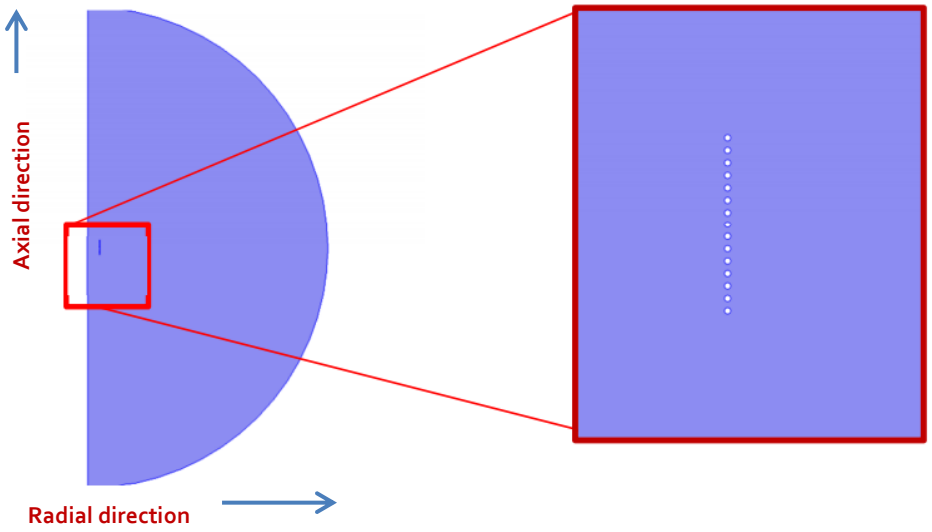

Figure 81: Geometrical model of the inductor used in COMSOL simulations. The inductor is placed around the axis of symmetry in both axial and radial direction.

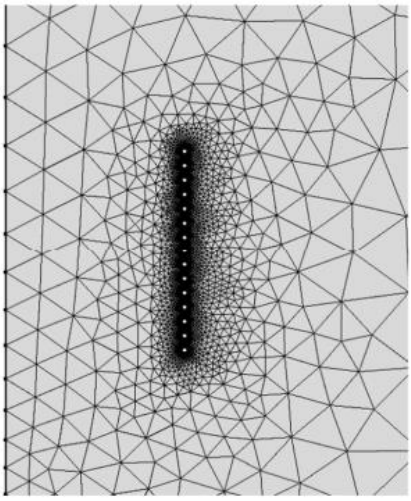

Figure 82: Details of the model mesh around the inductor.

10.3.1.2 *E field simulation for the inductor*

The simulations are run applying $0\ V$ at the external boundary of the domain as a far field approximation and distributing the inductor voltage, 30 kV, equally among each turn of the inductor with the lower side of the inductor grounded. No dependence on frequency was considered i.e. the simulations were performed in electrostatic conditions. The results can be seen in Figure 83 for the electric field magnitude. As expected the highest value of electric field was found near the inductor with value in the order of $8.6 \times 10^5\ V/m$. Figure 84 shows a

plot of the electric field in the radial and axial directions. The electric field is very high near the inductor but falls off considerably as the distance from the inductor increases. The results are tabulated in the Table 22.

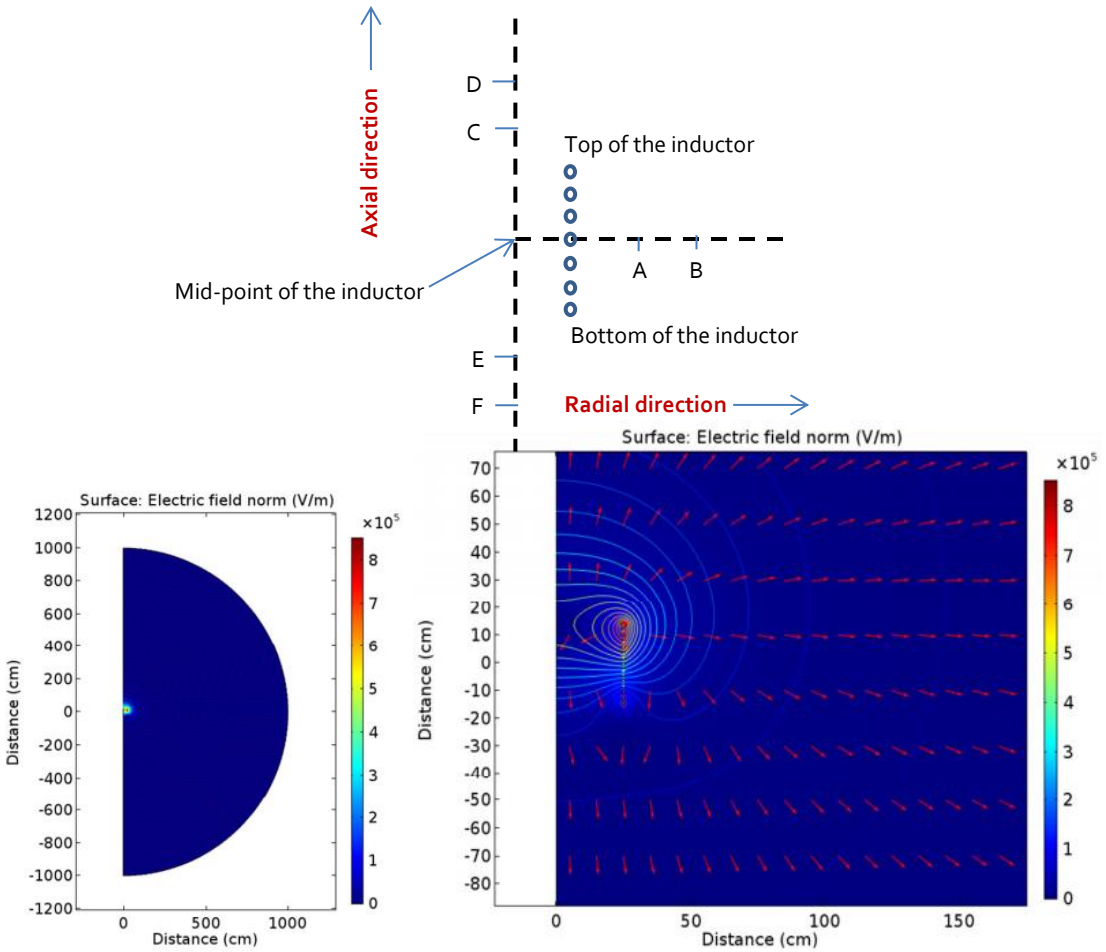

Figure 83: Electric field (V/m) calculation near the inductor.

Table 22: E field generated by the inductor

Distance(m)	Radial Electric Field(V/m)	Axial Electric field (V/m)	
		From the top of inductor (end with +30kV)	From the bottom of inductor (end with 0V)
2	1000 (A)	1000 (C)	700 (E)
5	150 (B)	160 (D)	130 (F)

An upper limit was set on the results visualization in accordance with that provided by Italian regulation (i.e. 87 V/m for electric field), and the plot is shown in Figure 85.

The results of the analyses show that a safe working distance for the personnel to be present during the experiment is beyond 7 m from the inductor.

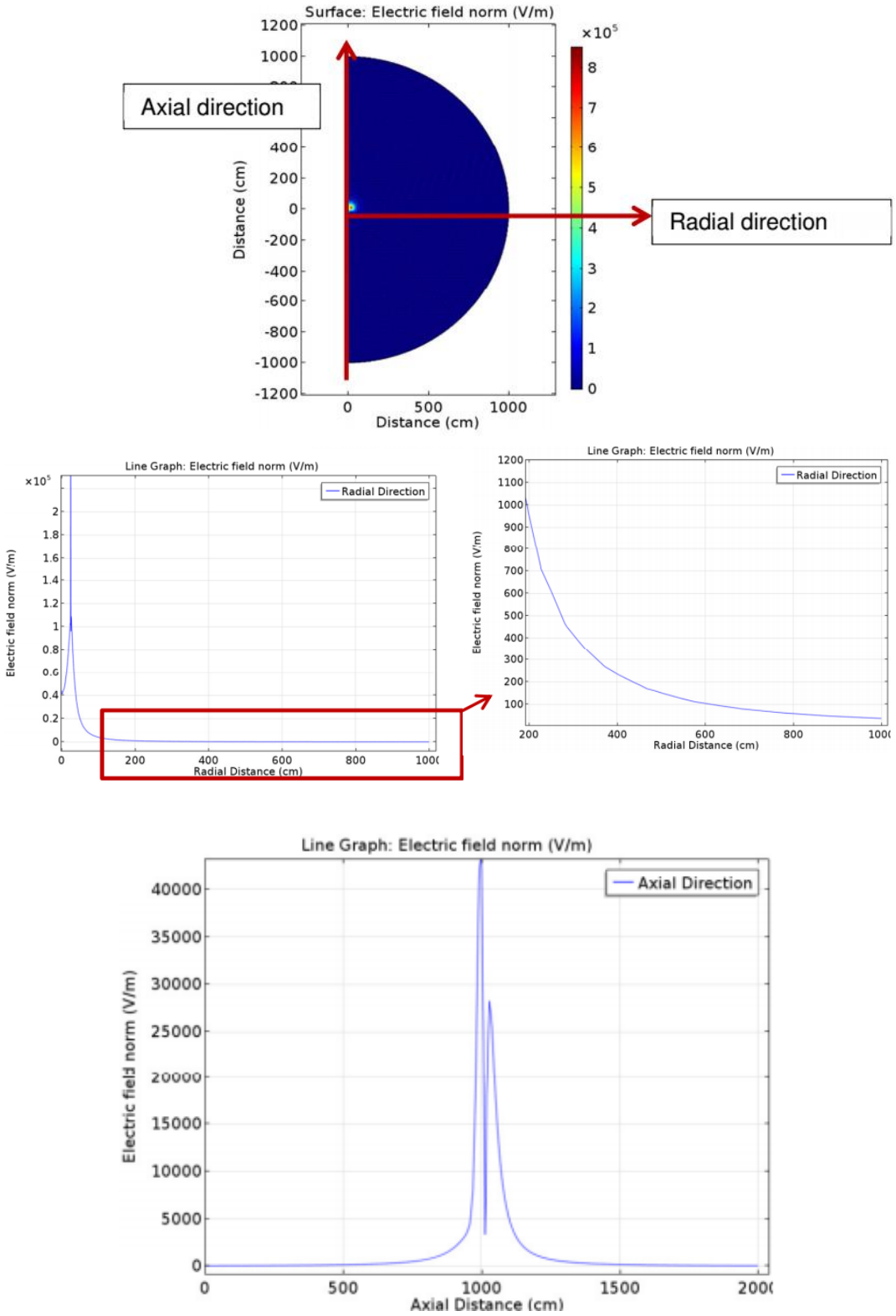

Figure 84: Radial and axial electric field calculation near the inductor.

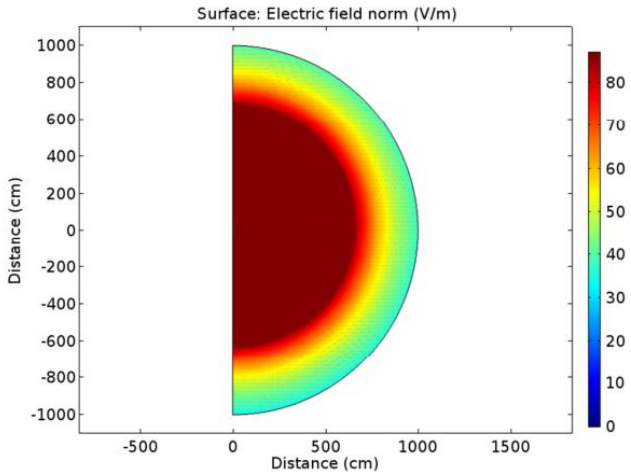

Figure 85: E field of inductor.

10.3.1.3 *H field simulation for the inductor*

The magnetic field generated by the inductor was evaluated. The inductor coil was loaded with a $60\ A$ current and the external boundary was set with a null potential vector condition. No dependence on frequency was considered i.e. the simulations were performed in magneto-static conditions, since the frequency does not play any role in the field intensity evaluation. The results can be seen in Figure 86 for the magnetic field magnitude. Here only the results in the radial direction are considered.

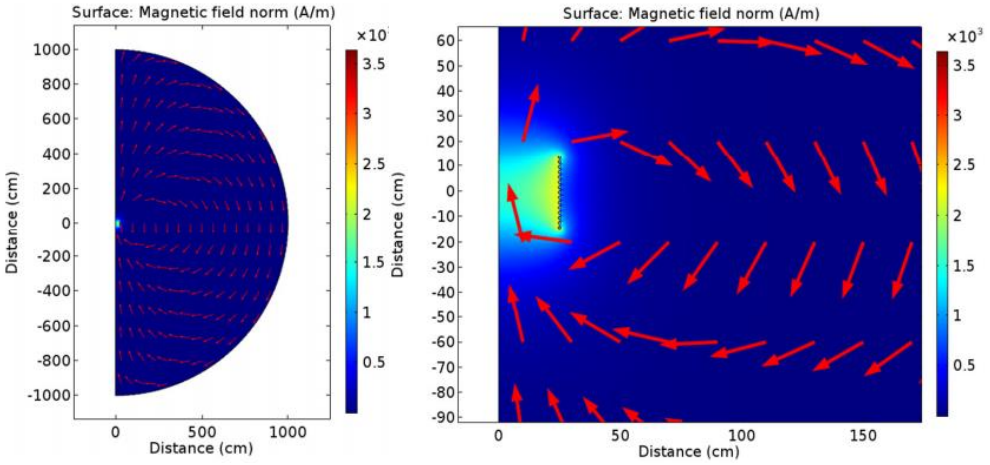

Figure 86: Magnetic field (A/m) calculation.

The highest magnetic field calculated is of the order of $3.7\ \times 10^3\ A/m$. Figure 87 shows a plot of the magnetic field in the radial directions. The magnetic field is very high near the inductor but falls off considerably as the distance from the inductor increases. The results are tabulated in the Table 23.

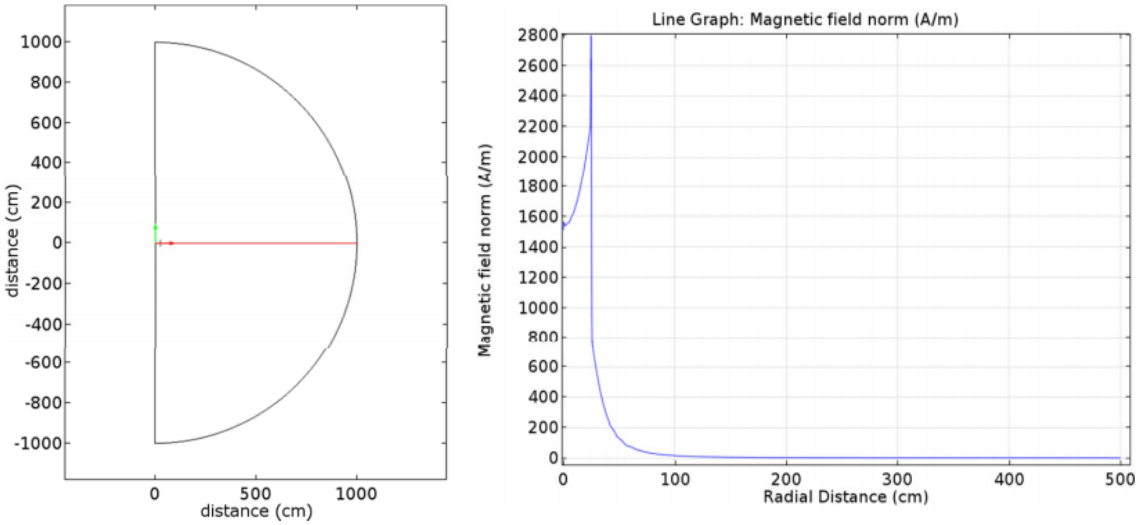

Figure 87: Magnetic field (A/m) calculation in radial direction for Inductor.

Table 23: H field generated by the inductor in the radial direction

Distance (m)	Magnetic field norm (A/m)
2 **(A)**	2.01
5 **(B)**	0.14

An upper limit was set on the surface plot in COMSOL simulation results, in accordance with that provided by Italian regulation (i.e. 0.73 A/m for magnetic field intensity vector).

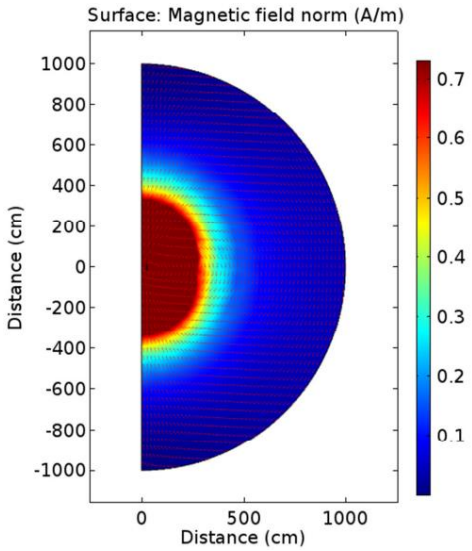

Figure 88: Magnetic field (A/m) calculations for inductor

The analyses of the magnetic field show that safe working distance for the persons to be present during the experiment is beyond 3 m from the inductor.

10.3.2 Electric and Magnetic field generated by the RF load

10.3.2.1 *FEM model*

In order to analyse the electric field generated near the vacuum vessel during operation, a FEM model that comprises the vacuum chamber, the metallic support, the feedthroughs and the electrodes (the smallest one) has been developed. The analysis has been done in a large domain (a cylinder of 10 m radius and 10 m height) where the load is in free air and the effect due to the surrounding structures is neglected, except for the ground floor. The simulations performed were in 2D axisymmetric and electrostatic regime with $0V$ potential applied to the domain boundary as well as to the metallic support of the vacuum vessel and the vacuum vessel itself. Two cases were considered:

- Case 1: The voltage of +30 kV is applied to the top feed-through and electrode inside the vacuum vessel, while the other feedthrough and electrode are kept at the zero potential;
- Case 2: The voltage of +30 kV is applied to the bottom feedthrough and electrode inside the vacuum vessel, while the other feedthrough and electrode are kept at the zero potential.

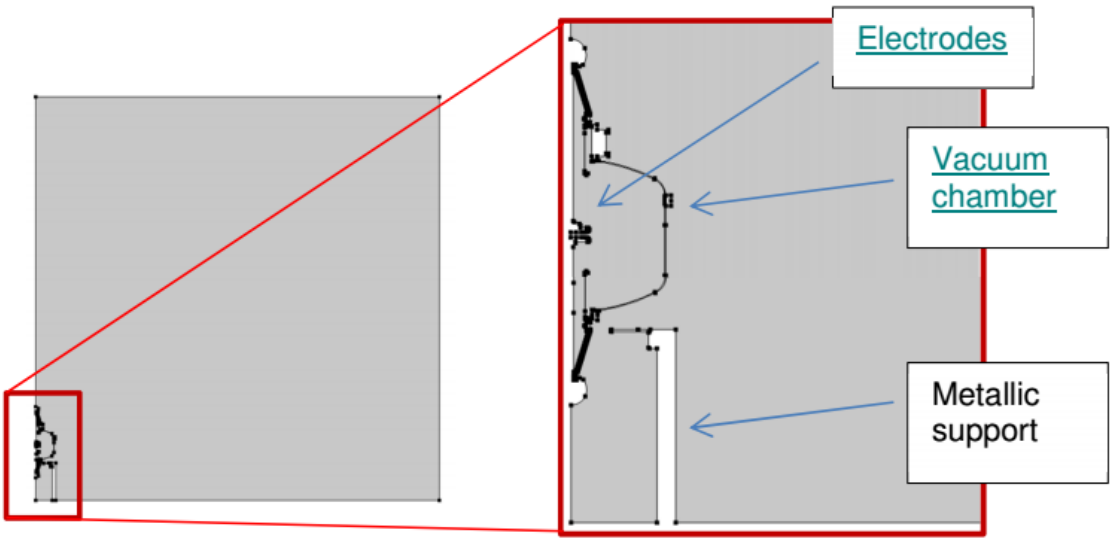

Figure 89: Geometrical model of vacuum vessel (along with a metal table) used in COMSOL.

The simulations were performed by constructing a free triangular mesh around the vacuum vessel as can be seen in the Figure 90.

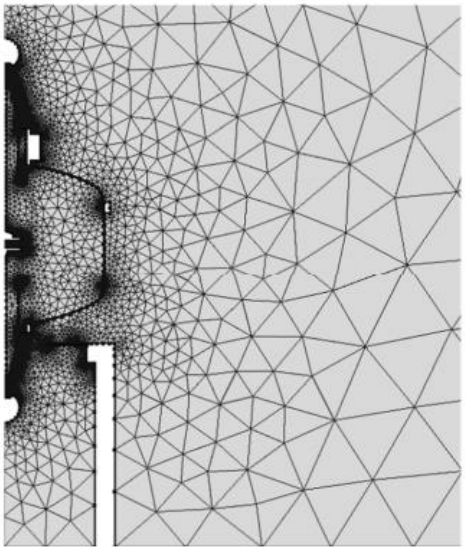

Figure 90: Mesh around vacuum vessel.

10.3.2.2 *E field simulation for the load*

Case 1: The voltage of +30 kV is applied to the top feedthrough and electrode inside the vacuum vessel, while the other feedthrough and electrode are kept at the zero potential

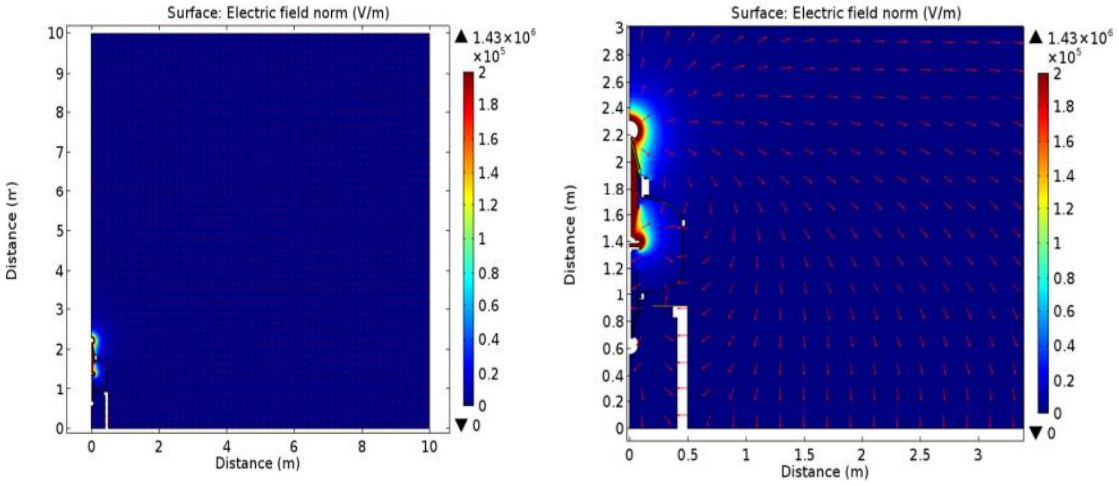

Figure 91: Case 1: Electric field (V/m) calculations for vacuum vessel.

As expected, the highest value of electric field was found near the electrode with the potential voltage of +30 kV. This value is $1.43 \times 10^6\ V/m$. The result plotted with a coloured scale with a maximum E-field limit in accordance with that provided by the Italian regulation (i.e. 87 V/m for electric field) is shown in Figure 92. The analyses show that the safe working

distance for the person to be present during the experiment is around 4 m from the vacuum vessel.

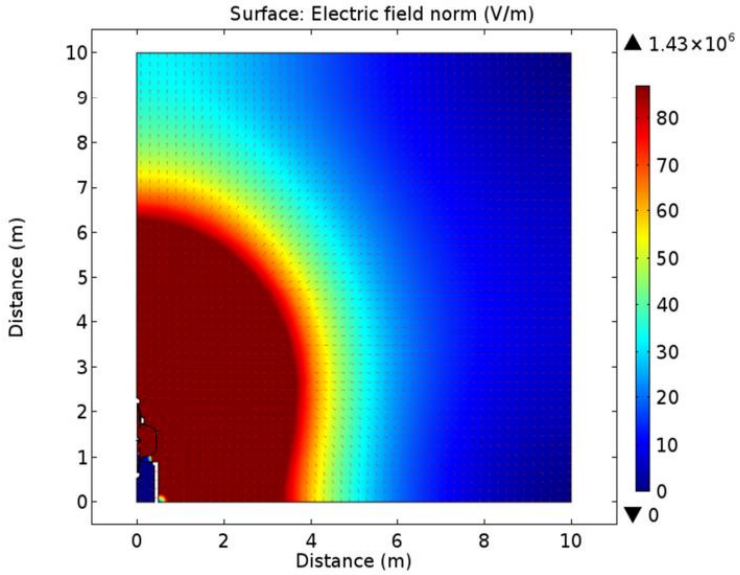

Figure 92: Case 1: Electric field (V/m) calculations for vacuum vessel.

Case 2: The voltage of +30 kV is applied to the bottom feedthrough and electrode inside the vacuum vessel, while the other feedthrough and electrode are kept at the zero potential

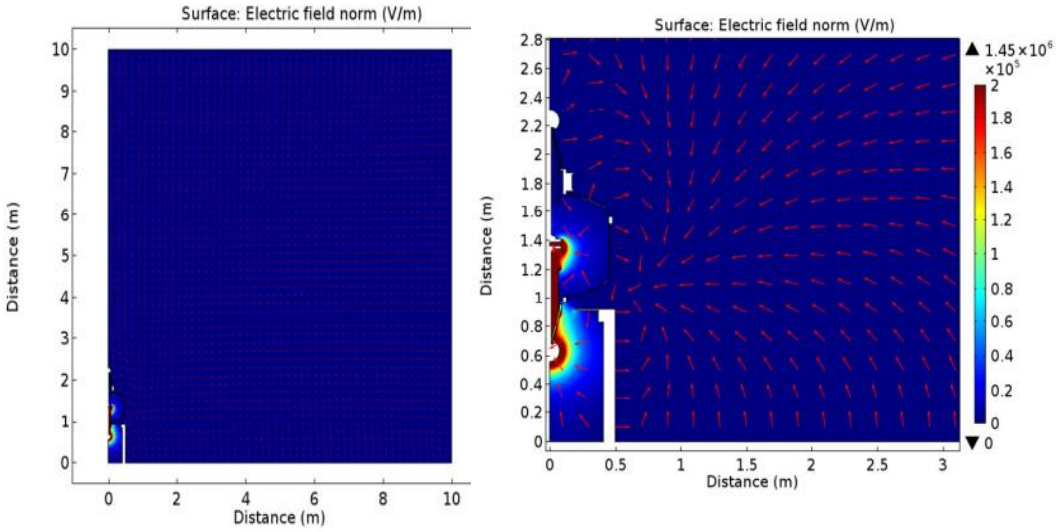

Figure 93: Case 2: Electric field (V/m) calculations for vacuum vessel.

As expected, the highest value of electric field was found near the electrode with the potential voltage of+30 kV. This value is $1.45 \times 10^6\ V/m$ .The results plotted with the upper

limit in accordance with that provided by the Italian regulation (i.e. 87 V/m for electric field) are shown in Figure 94:

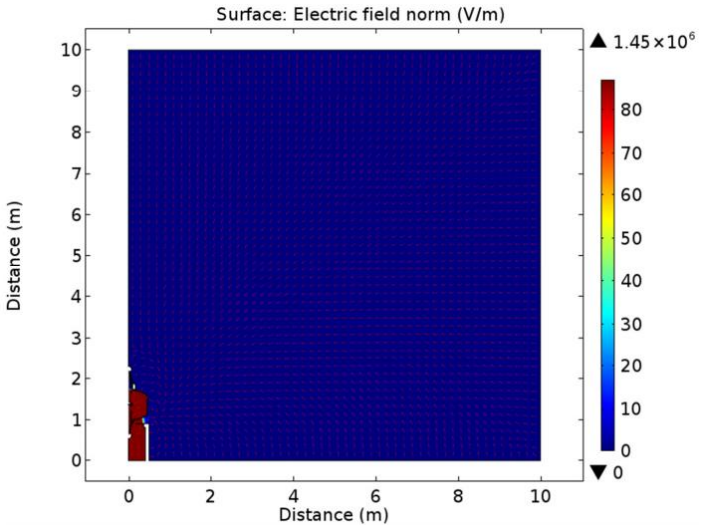

Figure 94: Case 2: Electric field (V/m) calculations for vacuum vessel.

The analyses in this case show that the safe working distance for the personnel to be present during the experiment is beyond 1 m from the vacuum vessel. The metallic vacuum vessel and the metallic structure around the electrodes act as shield to the electric field generated, since the 2D model considers the supporting structure as a closed cylindrical surface which is similar to provide local shield (see paragraph 10.4.1.1 and the comment in discussion 10.4.4).

10.3.2.3 *H field calculation for the load*

To calculate the magnetic field produced by the vacuum vessel, an analytical approach was followed. An equivalent current carrying wire was considered representing the current flowing through the electrodes placed inside a vacuum vessel. These calculations are very basic and do not take into account the effect of vacuum vessel and the supporting metallic structure. The magnetic field H (A/m) was calculated using the following formula:

$$H = \frac{I}{2\pi r} \qquad (114)$$

Where:

- I is the current flowing through the wire (see paragraph 10.1.3 for the calculated values for each electrode pair)
- r is the distance from the current carrying wire.

The variation of magnetic field (A/m) with distance for the three electrodes can be seen in the Figure 95. The summary of the results is shown in Table 24.

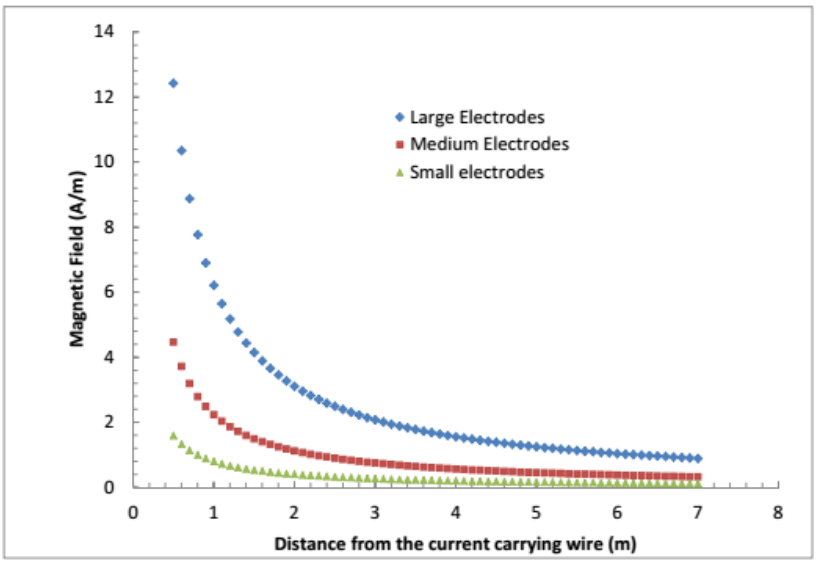

Figure 95: Variation of magnetic field (A/m) with respect to the distance (considering an equivalent.

Table 24: H field for load

Electrodes	H (A/m) @ 2m	H (A/m) @ 5m
Large	3.1	1.24
Medium	1.11	0.44
Small	0.39	0.16

The analyses in this case show that the safe working distance for the personnel to be present during the experiment is beyond 1 m from the electrodes when the smallest electrodes are considered.

10.4 EM shielding

The HVRFTF will be hosted in the RF laboratory, where the personnel will work at the distance of about 2 m from the EM sources, a reasonable distance considering the space available for the lab.

As seen in paragraph 10.3 the EM field at such distance is much higher than the allowed limits provided by the Italian regulation; therefore an EM shield is necessary for a safe working environment.

In order to design an EM shield it is necessary to define its target quality/performance by means of a parameter called "Shielding Effectiveness". It is the ratio of the magnitude of the electric (magnetic) field that is incident on the shield to the magnitude of the electric (magnetic) field that is transmitted through the shield [96][97]:

$$SE_E = 20\ \log_{10}\left|\frac{E_i}{E_t}\right| \quad (115)$$

$$SE_H = 20\ \log_{10}\left|\frac{H_i}{H_t}\right| \quad (116)$$

Where E_i and H_i are the incident electric and magnetic field intensity and E_t and H_t are the transmitted electric and magnetic field intensity. In this report the incident field (E_i and H_i) are considered not affected by the presence of the shield, i.e. the shield does not affect the EM sources behaviour.

In the Table 25, a summary of the information on the electric and magnetic fields calculated in the previous sections are reported, with the SE required to the shield considering the law limits.

Table 25: Summary of the requirements for the shield of the inductor

	E field	H field
Value of field @ 2 m from source	1000 [V/m]	2.01 [A/m]
Law limit @ 1 MHz	87 [V/m]	0.73 [A/m]
Shielding Effectiveness required to the shield	21.2 [dB]	8.8 [dB]

10.4.1 Evaluation of possible shielding strategies

In this section a brief description of the possible methods which can be used to shield the EM sources are presented. The effective shielding can be reached both with a global and a local shield, a mixture of the two or with a quasi-global shield, see Figure 96.

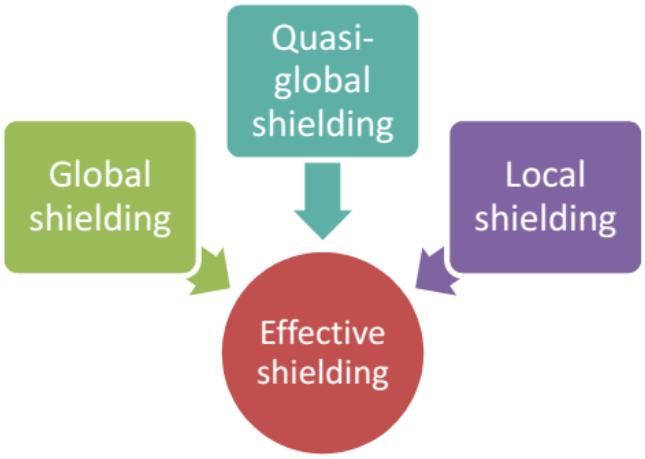

Figure 96: Possible ways to achieve effective shielding.

10.4.1.1 *Local shielding*

One solution is a local shielding of all the parts individually (resonant circuit, vacuum chamber). In particular the benefits are:

- Better control of the joints (i.e. connections between the parts) over small boxes;
- Possible in house construction;
- Less expensive (less material to be used);
- Reduction of the noise to the power supply system
- Reduced requirements for a global shield in case it still remains necessary.

The local shield solution has an operative benefit: it introduces a fixed boundary for the components which fixes the values of the stray capacitances to ground independently from the system layout (for instance the presence of a measuring instrument will not influence their values), thus resulting in the stabilization of the operating frequency of the circuit.
The local shield has a disadvantage: it is true that it fixes the stray capacitances to ground values, but it also increases their values with respect to the global shield which can prevent the achievement of the targeted high voltage.

10.4.1.2 *Global shielding*

With the global, shielding the whole dedicated area where the experiments are to be performed is shielded. The whole laboratory can be shielded with a metal plate or a wire mesh to improve ventilation. Providing a shield for the whole laboratory could be more expensive compared to the local shield, but from the operational point of view it gives more flexibility for the laboratory activities. In fact it is possible to change the geometry of the components or to use the same area for different tests.

10.4.1.3 *Quasi-global shielding*

A cheaper solution, compared to the global shielding, is to have only a metallic wall between the EM field sources and the people operating the facility. This is known as quasi-global shielding. The effectiveness of such shield is verified by means of simulations and the results described in the following. Dedicated measure is also carried out to confirm its suitability.

10.4.2 Materials survey for RF shielding purposes

The shielding effectiveness of a slab or mesh of a certain material of a given geometry is affected by the EM field frequency, the material's conductivity and magnetic permeability.

Shielding of RF field results from wave reflection on the surface of the material, the absorption of energy as it passes through it; and re-reflection at the second surface [97]. The

material absorption is affected by the skin depth δ. The smaller the skin depth, the thinner (in terms of thickness) can be the slab or mesh required to reach the EM field level.

In the design of a shielded enclosure it is crucial to minimize the quantity of seams and penetrations and to maximize their quality. In fact they are the critical points for the shielding performance. In Table 26 two possible materials which can be used for RF shielding are listed with a summary of their advantages and disadvantages.

Table 26: Materials for shielding enclosure

Materials	Advantages	Disadvantages
Copper (most versatile and widely used)	• It can be formed fabricated and soldered easily. • High conductivity (5.8×10^7 Ω/m) • Slow oxidation - Do not oxidise rapidly when exposed to normal atmospheric conditions. • Galvanic corrosion is minimized since copper is cathodic with respect to other metals. • Non-ferrous – ferrous properties are required for good low frequency and DC magnetic shielding.	• Expensive
Aluminium (second most commonly used material)	• Non ferrous • Ability to extrude custom shapes and design larger components for reduced weight.	• Oxidation – an oxide layer is formed within hours after been exposed to the air. This oxide will stop forming after it

10.4.3 Simulation of the effect of a quasi-global shielding

The aim of this paragraph is to understand if the quasi-global shielding can be an effective strategy for the HVRFTF. The EM field generated by the RF inductor in presence of a copper metallic plate/wall is simulated and then the shielding effectiveness is calculated.

10.4.3.1 *FEM model*

The system under investigation is composed of the RF inductor and a copper plate of 1 mm thickness and 4 m height placed at the distance of 2 m (reasonable distance from the EM source for the personnel to work in the HVRFTF) from the axis of symmetry. The model developed in COMSOL Multiphisics® is a 2D axisymmetric model, with a large circular simulation domain with 5 m radius. The geometrical model can be seen in the Figure 97.

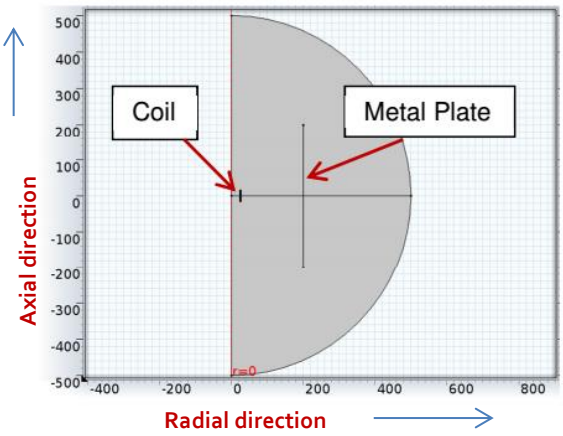

Figure 97: Geometrical model of the inductor with a metal cylinder of thickness 1 mm placed at a distance of 2 m. The shield is placed around the axis of symmetry only in axial direction.

For the case of H field a cylinder without the top and bottom lids is considered around the inductor, see Figure 98:

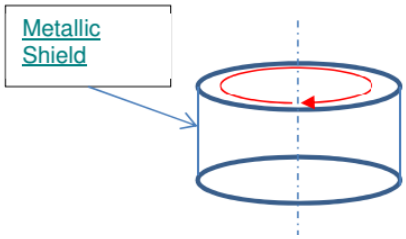

Figure 98: Cylinder and current path in red.

An extremely refined free triangular mesh around the coil and metal plate has been set, as can be seen in the Figure 99.

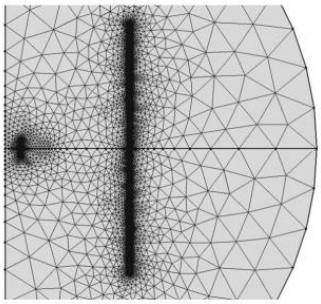

Figure 99: Mesh around the coil and metal plate in COMSOL.

10.4.3.2 *E field simulation for the quasi global shielding of the inductor*

A simulation in electrostatic regime with a 30 kV voltage equally distributed among the coil turns was run. The copper cylinder potential and the domain boundary have been set to $0\ V$. The electric field results are reported in Figure 100 where the law limit (87 V/m) is also

reported for comparison. The simulation shows a good shielding performance in the radial -direction (where just on the outer edge of the shield the E field is 5 V/m) but poor in the axial-direction. This finding reveals the necessity to extend the copper cylinder around the inductor to improve the shielding.

10.4.3.3 *H field simulation for the quasi global shielding of the inductor*

The analyses were performed for different frequencies (100 kHz, 400 kHz, 700 kHz and 1 MHz) in the magneto quasi-static regime considering a current of 60 A flowing through the inductor, Figure 98. The Dirichlet boundary conditions were used, with zero vector potential A. The effect of the shielding on the H field at 1 MHz is shown in Figure 101 in the complete domain: the upper limit was set on the surface plot, in accordance with that provided by Italian regulation (i.e. 0.73 A/m for magnetic field intensity vector).

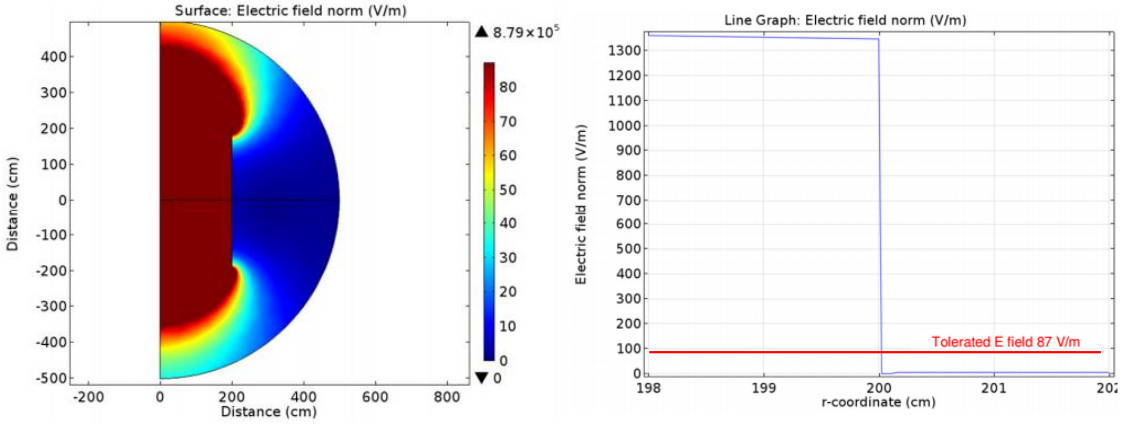

Figure 100: Electric field simulations with metallic wall at a distance of 2 m form the axis of symmetry: (left) electric field around in the simulation domain; (right) effect of the 1mm thick wall electric field.

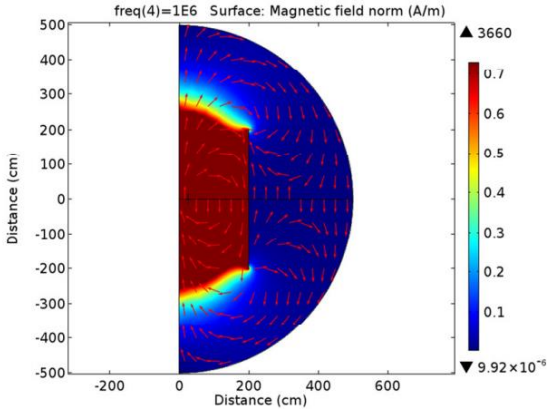

Figure 101: Magnetic field simulations with metallic cylindrical wall at a distance of 2 m form the axis of symmetry.

Figure 102 shows the H field in radial direction, around the shield, where the upper limit is also indicated. It is possible to note that:

- the field is more attenuated for higher frequency;
- the complete attenuation of the magnetic field is obtained (on the outer edge of the wall);
- the magnetic field at the inner edge of the wall is 6.4 A/m.

10.4.3.4 *Summary of the results for "the quasi global shielding"*

Table 27 summarizes the performances of the quasi global shield placed at 2 m from the inductor axis and composed of 1 mm thick copper slab. It allows reducing the maximum field values below the permissible law limits.

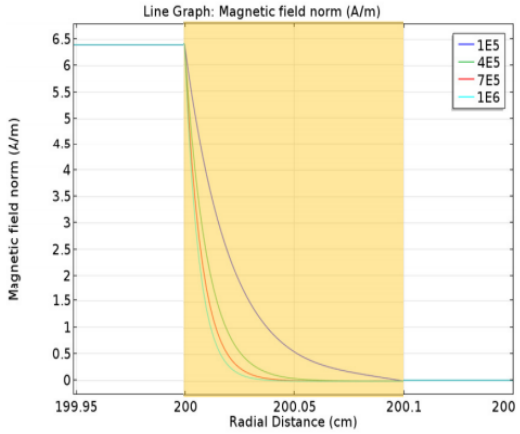

Figure 102: Magnetic field H (A/m) in the radial direction in the case with 1 mm thick copper cylinder at distance of 2mm from the axis of symmetry. In gold transparency is the copper wall section.

Table 27: Summary of the results for the "quasi global shielding"

	E field	**H field**
Law limit @ 1 MHz	87 [V/m]	0.73 [A/m]
Value of field @ 2m from the source without shield	1000 [V/m]	2.01 [A/m]
Value of field @ 2 m from source with the shield of thickness 1mm	5 [V/m]	0.5 [A/m]
Shielding Effectiveness of the quasi global shielding	46 [dB]	12 [dB]
Safety factor achieved	17.4	1.46

10.4.4 Shield choice and installation

To achieve the required S.E. it is possible to use as suitable electro-magnetic shield like an aluminium slab or a perforated sheet. The first choice assures a better S.E., the latter allows

the cooling and the view of the components placed inside. A mesh with a thickness of 2 mm and holes displaced as in the Figure 103 (a) is available commercially. To calculate the shielding effectiveness of this mesh an approximation is made as shown in Figure 103 (b) The S.E. of the perforated sheet can be evaluated conservatively and analytically (the method is present in [96], [97] and [98]), as that of a mesh having the dimensions reported in in Figure 103 (b).

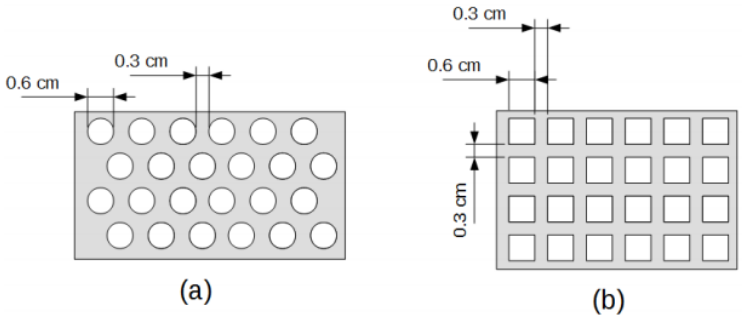

Figure 103: (a) Perforated aluminium sheet available commercially and (b) approximation for calculation of S.E.

The S.E. calculated for the slab and for the perforated sheet, placed at 0.5 m from the axis of the source, is reported in Table 28.

Table 28: Calculated S.E. of aluminium EM shield

	S.E. E field [dB]	S.E. H field [dB]
Shielding Effectiveness required to the shield	21.2	8.8
Aluminium slab	252	173
Perforated aluminium sheet (b)	178	99

It is possible to effectively screen the EM field with the perforated aluminium sheet and the setup is shown in Figure 104:

- RF circuit placed under the supporting structure of the vacuum vessel;
- High Voltage terminal of the RF circuit connected to the bottom feedthrough;
- Perforated aluminium sheet attached to the legs of the supporting structure of the vacuum vessel.

10.5 EM field measurements

Discussions about the generation of EM fields during experiments were carried out with external qualified expert for EM fields. The EM field levels next to the operators of HVRFTF have been measured by in house measurements with NARDA probe. The effectiveness of the EM shielding box (quasi-global) was proved with dedicated measures performed by the external qualified expert as reported in [99]. It was found that the H field at about 20 cm from the EM shielding box is 0.24 A/m (law limits are 0.73 A/m for general public and 1.59 A/m for

workers), while the E-field at 1 m from the EM shielding box is about 1 V/m (law limits 87 V/m for general public and 170 V/m for workers). These measurements prove the effectiveness of the EM shielding box in the reduction of the EM field below law limits. The highest E-field was measured in front of the RF amplifier (90 V/m at 30 cm from the amplifier).

Figure 104: EM shield installed in HVRFTF.

10.5.1 E-field probe verification

As reported in the paragraph above, the E-field produced by HVRFTF has been measured by a qualified expert using calibrated instrumentation and it was found well below the law limits. The idea is anyway to monitor the E-field produced by HVRFTF during experimental campaigns with an E-field measuring system (probe NARDA 8761D [100] and meter 8718 [101]) is available at the Consorzio RFX. This probe is not calibrated but it can be used to verify the order of magnitude of the E-field near the HVRFTF, once verified qualitatively for the reliability of its readings. For this purpose some tests were performed with the setup shown in Figure 105.

The output voltage of a waveform generator, measured with an oscilloscope, is applied to a metallic plate which is in between a couple of grounded plates at a known distance. This testing circuit provides a region with known electric field strength where E-probe is placed to take the measurements. The tests were carried out, the related analyses were done. Here just the summary of the conclusions is presented.

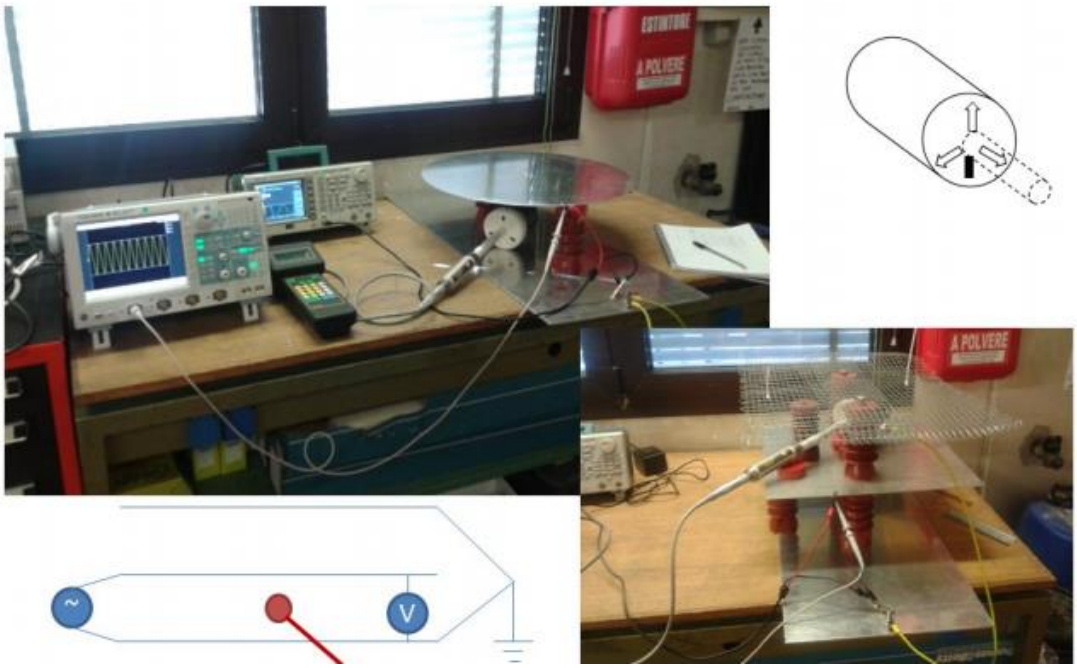

Figure 105: Photos of the setup for E-field probe verification.

The analyses indicate that the measured E-field is the one expected once applied the conversion coefficient tabulated in the Table 29 .

Table 29: NARDA probe accuracy and relative error

Frequency [MHz]	Conversion factor k	Relative error	
		< 10 V/m	> 10 V/m
0.5	$E_S = 1.026\ E_M$	± 0.51	± 0.24
1	$E_S = 1.002\ E_M$	± 1.62	± 0.16
3	$E_S = 1.011\ E_M$	± 0.13	± 0.09
10	$E_S = 0.921\ E_M$	± 1.21	± 0.14

With E_S is indicated the source electric field (V/m), while E_M is the measured average electric field (V/m).

10.6 Discussion

The analyses for the evaluation of the EM field level around RF components highlighted the need for a shield to cope with the limits imposed by the Italian regulation. As seen from the results in the diagrams of paragraph 0 and on the summary of Table 27, presence of 1 mm thick metal plate at the distance of 2 m from the inductor is sufficient to reduce the intensity of electromagnetic radiations below the limits provided by Italian regulations, with a safety factor of 1.46 for H field and 17.4 for E field.

Dedicated measurements were carried out in the final circuit configuration to verify the suitability of the identified shielding solution and finally the perforated aluminium sheet of 2mm thickness was selected to shield resonance circuit. The shield was then installed and the EM field measurements were taken by the experts. The expert verified the effectiveness of the shield as the values measured for the electric and magnetic fields were well below the value set by the Italian regulations.

All the analytical and experimental studies carried out in this research were very useful and led to the successful set-up of the HVRFTF for the first operation. A picture of the laboratory can be seen in Figure 106.

Figure 106: Photo of the final arrangement of the HVRFTF.

CONCLUSION

The work done in this thesis is within the framework to perform the studies and experimental activities to qualify the behaviour of RF power circuits for Negative Ion Sources of Neutral Beam Injectors (NBI) for ITER and fusion experiments. Two separate activities; on the High Voltage Radio Frequency Test Facility (HVRFTF) and on the power transfer efficiency of inductively coupled (IC) RF ion sources have led to some interesting findings.

With reference to my participation in the design, construction and set-up of the HVRFTF, the main results of my work can be synthesized as follows.

The experimental measurements of inductance and resistance of the inductor of the RF resonance circuit in different conditions contributed to the electrical characterization of the special design of this key component, composed of two copper solenoids mutually coupled and connected in parallel.

The thermal analyses which I performed on the rods supporting the electrodes of a device under test in the HVRFTF heated by the current flowing through them at the frequency of 1 MHz, allowed to identify the limits in the RF pulse duration, compatible with the use of steel as material of electrodes of different sizes.

As for the EM shielding, my studies, calculations and analysis highlighted that the electric and magnetic fields in the test facility during the operation could have been much higher than the allowed Italian law limits for general public. To solve the issue, I designed a shield of 2 mm thick perforated aluminium to be installed around the main source of EM fields. The effectiveness of the shield was then checked and certified by an expert and was found to be suitable for the test facility.

All these contributions concurred to the success in the set-up of the test facility which is now in operation.

The most significant part of my thesis work is related to the development of a novel methodology to estimate the power transfer efficiency of the IC RF ion sources. This methodology is based on the integration of an analytical and an electrical model for the power deposition in the plasma.

Regarding the analytical model for describing different mechanisms which lead to the power deposition in the plasma, one of the vital steps was the identification of the role of stochastic heating. The challenging part was to estimate the stochastic heating collision

frequency and to explain its significance. To tackle this problem, a detailed description of the model have been provided which not only leads to the calculation of the stochastic heating collision frequency but also gives an information regarding the onset of the stochastic heating within the driver. It was found that stochastic heating is dependent on features of the ion source like the geometry, operating frequency, gas pressure etc. For example, during the application of the model to the simplified driver of the ELISE and NIO1 ion source, it was found that stochastic heating is the dominant heating mechanism at low pressure ranges (below 1 Pa for both ELISE and NIO1 ion source), whereas ohmic heating is dominant at higher pressures.

The role of the geometric effects while calculating the skin depth is another important aspect of the modelling. This geometric effect is found to be dependent on the chamber radius of the driver in addition to its dependence on the applied and collision frequency and other plasma parameters (like electron density). I found that for small ion source like NIO1 the geometric effects play a crucial role whereas they are not so relevant for a relatively large source like ELISE.

The missing gap between the analytical model and the estimation of the power transfer efficiency in the methodology is filled with an electrical model which is responsible for the coupling of the power from the RF coil to the plasma. As a first approach, this electrical model is defined by a simple transformer model where the power is transferred from the RF coil only to the plasma. Then, a multi current filament model is developed, introduced and implemented in place of the transformer model which then turned out to be a remarkable improvement in the methodology. In this multi current filament model, a major limitation of the transformer model has been overcome and the power deposition in the surrounding metallic structure of the driver is also considered. Hence, it takes into account the more realistic experimental set up.

I applied the developed methodology with both the transformer and the multi-filament model to two ion sources currently in operation: ELISE and NIO1. For both the sources, the results showed that the plasma equivalent resistance is reduced by half for multi-filament model (that is 6.5 Ω for ELISE and 4.5 Ω for NIO1 respectively) in comparison with the transformer model (13 Ω for ELISE and 9 Ω for NIO1 respectively). Further insights showed that a reduction in the assumed plasma radius, to account in some way for the non-uniform plasma density versus the radius, leads to an evaluation of plasma equivalent resistance closer to the experimentally derived value in case of ELISE (1.8 Ω) and more close to analytically derived values from the other model in case of NIO1 (1.7 Ω). As a consequence, a more realistic reduction in power transfer efficiency is also observed.

The analyses of the results for both the ion sources reveal one significant finding of this research, it can be seen that the power transfer efficiency increases with the increase in operating frequency reaching maximum value of around 10 MHz. These results indicate that the preferable operating frequency seems one order of magnitude higher than the chosen frequency for ELISE (1 MHz) or NIO1 (2 MHz) ion source.

Despite the fact that there is a lack of experimental validation on ELISE or NIO1 ion source, the methodology on its path towards development have been validated at several steps in some way. The various parts of the model are either validated with the experimental results found in the similar ion sources or with the experimental set-up found in literature. For instance, the model for the estimation of the electron temperature has been validated with the experimental result with similar type of ion source. The transformer model has been validated with Argon gas with an experimental set-up found in literature. Furthermore, the qualitative behaviour of several parameters like; ohmic and stochastic heating collision frequency, skin depth, plasma equivalent resistance variation with electron density etc. are in line with several other research findings in the literature.

As a future work, the developed methodology could be made more self-consistent, in such a way that plasma parameters like electron density and temperature are not considered independently. Future calculations of the radial density profile could also be included. The external static magnetic field applied in ion source to confine plasma away from the wall chamber is expected to have an impact on the plasma conductivity. Therefore, it will be interesting to incorporate this effect into the methodology and hence obtain the results in view of more realistic experimental scenario.

REFERENCES

[1] H. I. Initiative, "January 2013," *Lancet Neurol.*, vol. 12, no. January, pp. 1–8, 2013.

[2] BP, "BP Statistical Review of World Energy 2017," *BP Stat. Rev. World Energy*, p. 52, 2017.

[3] M. Kikuchi and N. Inoue, "Role of fusion energy for the 21 century energy market and development strategy with international thermonuclear experimental reactor," 1951.

[4] M. Kikuchi, K. Lackner, and M. Quang, *Fusion Physics*. 2012.

[5] "Tritium." Health Physics Society, Specialists in Radiation Safety, pp. 1–5, 2011.

[6] J. Wesson and D. Campbell, *Tokamaks*, Fourth Edi. Oxford University Press.

[7] G. Brennan, "When will fusion power European grids? – the commercial reactor – Part 2," 2016. [Online]. Available: http://www.engineersjournal.ie/2016/02/09/when-will-fusion-power-european-grids-the-commercial-reactor-part-2/.

[8] R. Betti and O. A. Hurricane, "Inertial-Confinement fusion with lasers," *Nat. Phys.*, vol. 12, no. 5, pp. 445–448, 2016.

[9] M. Zuin, S. D. Bello, P. Martin, and M. E. Puiatti, "Overview of the RFX-mod contribution to the Overview of the RFX-mod contribution to," 2015.

[10] M. Wakatani and N. York, "Stellarator and Heliotron Devices," *Nucl. Fusion*, vol. 39 293, 1999.

[11] Bittencourt J.A., *Fundamentals of Plasma Physics*, Third Edit. Springer, 2004.

[12] "ITER official website." [Online]. Available: http://www.iter.org/.

[13] Jeffrey P. Freidberg, *Plasma Physics and Fusion Energy*. Cambridge University Press, 2007.

[14] C. Gormezano, "Radio Frequency heating and current drive - Status and prospects for the Next Step," *Fusion Eng. Des.*, vol. 14, pp. 99–109, 1991.

[15] J. A. Snipes, Y. Gribov, and A. Winter, "Physics requirements for the ITER plasma control system," *Fusion Eng. Des.*, vol. 85, no. 3–4, pp. 461–465, 2010.

[16] J. . Schuss, M. Porkolab, Y. Takase, and et al, "Lower hybrid heating in the Alcator A tokamak," *Nucl. Fusion*, vol. 21, no. 427, 1981.

[17] R. S. Hemsworth *et al.*, "Overview of the design of the ITER heating neutral beam injectors," *New J. Phys.*, vol. 19, no. 2, pp. 0–20, 2017.

[18] M. J. Singh *et al.*, "Heating Neutral Beams for ITER : Present Status," *IEEE 26th Symp. Fusion Eng.*, 2015.

[19] R. F. Post, "High-Temperature Plasma Research and Controlled Fusion," *Annu. Rev. Nucl. Sci.*, vol. 9, no. 5, pp. 367–436, 1959.

[20] ITER Physics Expert Group on Energetic Particles, "Chapter 6 Plasma auxiliary heating and current drive," *Nucl. Fusion*, vol. 39 2495, 1999.

[21] R. Hemsworth and T. Inoue, "Positive and negative ion sources for magnetic fusion," *IEEE Trans. Plasma Sci.*, vol. 33, no. 6, pp. 1799–1813, 2005.

[22] M. Kuriyama *et al.*, "Operation of the negative-ion based NBI for JT-60U," vol. 40, pp. 115–121, 1998.

[23] ITER, "ITER technical basis ITER EDA DOCUMENTATION SERIES no. 24," *IAEA*, 2002.

[24] R. Gutser, "Experiments and Simulations for the Dynamics of Cesium in Negative Hydrogen Ion Sources for ITER N-NBI," 2010.

[25] U. Fantz *et al.*, "Towards powerful negative ion beams at the test facility ELISE for the ITER and DEMO NBI systems," *Nucl. Fusion*, vol. 57, no. 11, 2017.

[26] R. S. Hemsworth *et al.*, "Neutral beams for ITER (invited)a)," *Rev. Sci. Instrum.*, vol. 67, no. 3, p. 1120, 1996.

[27] M. Hanada *et al.*, "Development of negative ion sources for the ITER neutral beam injector," *Fusion Eng. Des.*, vol. 56–57, pp. 505–509, 2001.

[28] A. Krylov *et al.*, "Caesium and tungsten behaviour in the filamented arc driven Kamaboko-III negative ion source," *Nucl. Fusion*, vol. 46, no. 6, 2006.

[29] U. Fantz, P. Franzen, and D. Wünderlich, "Development of negative hydrogen ion sources for fusion: Experiments and modelling," *Chem. Phys.*, vol. 398, no. 1, pp. 7–16, 2012.

[30] R. S. Hemsworth, A. Tanga, and V. Antoni, "Status of the ITER neutral beam injection system (invited)," *Rev. Sci. Instrum.*, vol. 79, no. 2, 2008.

[31] U. Fantz *et al.*, "Negative ion RF sources for ITER NBI: status of the development and recent achievements," *Plasma Phys. Control. Fusion*, vol. 49, no. 12B, pp. B563–B580, 2007.

[32] B. Heinemann *et al.*, "Design of the 'half-size' ITER neutral beam source for the test facility ELISE," *Fusion Eng. Des.*, vol. 84, no. 2–6, pp. 915–922, 2009.

[33] U. Fantz *et al.*, "Spectroscopy - A powerful diagnostic tool in source development," *Nucl. Fusion*, vol. 46, no. 6, 2006.

[34] N. Miyamoto *et al.*, "Experimental results on ITER-NBI concept source," *AIP Conf. Proc.*, vol. 380, pp. 300–308, 1996.

[35] A. Ando, A. Komuro, T. Matsuno, K. Tsumori, and Y. Takeiri, "Radio frequency ion source operated with field effect transistor based radio frequency system," *Rev. Sci. Instrum.*, vol. 81, no. 2, pp. 2–5, 2010.

[36] V. Toigo *et al.*, "Progress in the realization of the PRIMA neutral beam test facility," *Nucl. Fusion*, vol. 55, no. 8, p. 83025, 2015.

[37] V. Toigo *et al.*, "The PRIMA Test Facility: SPIDER and MITICA test-beds for ITER neutral beam injectors," *New J. Phys.*, vol. 19, no. 8, p. 85004, 2017.

[38] P. Mauro, "Studies, analyses, available materials and technologies for plasma facing components - applications and future improvements for negative ion sources of neutral beam injectors," 2011.

[39] D. Marcuzzi *et al.*, "Detail design of the beam source for the SPIDER experiment," *Fusion Eng. Des.*, vol. 85, no. 10–12, pp. 1792–1797, 2010.

[40] E. Sartori, G. Serianni, and S. Dal Bello, "Simulation of the gas density distribution in the large vacuum system of a fusion-relevant particle accelerator at different scales," *Vacuum*, vol. 122, pp. 275–285, 2015.

[41] A. Maistrello, P. Jain, M. Recchia, and E. Gaio, "Studies on the requirements and design of the High Voltage Radio Frequency Test Facility," *Fusion Eng. Des.*, vol. 131, no. April, pp. 96–104, 2018.

[42] A. Zamengo, M. Recchia, W. Kraus, M. Bigi, C. Martens, and V. Toigo, "Electrical and thermal analyses for the radio-frequency circuit of ITER NBI ion source," *Fusion Eng. Des.*, vol. 84, no. 7–11, pp. 2025–2030, 2009.

[43] M. Bigi *et al.*, "Design, manufacture and factory testing of the Ion Source and Extraction Power Supplies for the SPIDER experiment," *Fusion Eng. Des.*, vol. 96–97, pp. 405–410, 2015.

[44] E. Gaio, W. Kraus, C. Martens, R. Piovan, E. Speth, and V. Toigo, "Studies on the radio frequency power supply system for the ITER NB injector ion source," *Fusion Eng. Des.*, vol. 82, no. 5–14, pp. 912–919, 2007.

[45] W. Kraus *et al.*, "The development of the radio frequency driven negative ion source for neutral beam injectors (invited)," *Rev. Sci. Instrum.*, vol. 83, no. 2, 2012.

[46] D. Marcuzzi, M. D. Palma, M. Pavei, B. Heinemann, W. Kraus, and R. Riedl, "Detailed design of the RF source for the 1 MV neutral beam test facility," *Fusion Eng. Des.*, vol. 84, no. 7–11, pp. 1253–1258, 2009.

[47] M. D. Palma, N. Pomaro, M. Maniero, R. Pasqualotto, L. Trevisan, and P. Sonato, "Design and RandD of thermal sensors for ITER neutral beam injectors," *IEEE Trans. Plasma Sci.*, vol. 42, no. 3, pp. 610–615, 2014.

[48] S. Spagnolo *et al.*, "Preliminary design of electrostatic sensors for MITICA beam line components," *Rev. Sci. Instrum.*, vol. 87, no. 2, pp. 2–5, 2016.

[49] E. Sartori, A. Panasenkov, P. Veltri, G. Serianni, and R. Pasqualotto, "Study of a high power hydrogen beam diagnostic based on secondary electron emission," *Rev. Sci. Instrum.*, vol. 87, no. 11, pp. 10–14, 2016.

[50] M. Barbisan, B. Zaniol, and R. Pasqualotto, "Modeling and simulation of a beam emission spectroscopy diagnostic for the ITER prototype neutral beam injector," *Rev. Sci. Instrum.*, vol. 85, no. 11, 2014.

[51] M. Brombin *et al.*, "The tomographic diagnostic of ITER neutral beam injector," *Nucl. Fusion*, vol. 53, no. 5, 2013.

[52] J. Zacks, U. Fantz, T. Farley, I. Turner, R. McAdams, and D. Wünderlich, "Characterisation of the SNIF ion source," *AIP Conf. Proc.*, vol. 1869, 2017.

[53] B. Heinemann *et al.*, "Negative ion test facility ELISE—Status and first results," *Fusion Eng. Des.*, vol. 88, no. 6–8, pp. 512–516, 2013.

[54] M. Cavenago *et al.*, "Development of versatile multiaperture negative ion sources," *AIP Conf. Proc.*, vol. 1655, no. 2015, p. 40006, 2015.

[55] M. Cavenago *et al.*, "First experiments with the negative ion source NIO1," *Rev. Sci. Instrum.*, vol. 87, no. 2, pp. 1–5, 2016.

[56] M. A. Lieberman and A. J. Lichtenberg, *Principles of Plasma Discharges and Materials Processing*, Second Edi. A John wiley & sons, inc publication, 2005.

[57] R. B. Piejak, V. Godyak, and B. M. Alexandrovich, "A simple analysis of an inductive RF discharge," *Plasma Sources Sci. Technol.*, vol. 1, pp. 179–186, 1992.

[58] V. Godyak, "Electrical characteristics and electron heating mechanism of an inductively coupled argon discharge," *Plasma Sources Sci. Technol.*, vol. 3, pp. 169 – 176, 1994.

[59] V. Vahedi, M. A. Lieberman, G. Dipeso, T. D. Rognlien, and D. Hewett, "Analytic model of power deposition in inductively coupled plasma sources," *J. Appl. Phys.*, vol. 78, no. 3, pp. 1446–1458, 1995.

[60] V. A. Godyak, R. B. Piejak, and B. M. Alexandrovich, "Experimental setup and electrical characteristics of an inductively coupled plasma," *J. App. Phys.*, vol. 85, no. 2, pp. 703–712, 1999.

[61] K. Suzuki, K. Nakamura, H. Ohkubo, and H. Sugai, "Power transfer efficiency and mode jump in an inductive RF discharge," *Plasma Sources Sci. Technol.*, vol. 7, no. 1, pp. 13–20, 1998.

[62] M. Cavenago and S. Petrenko, "Models of radiofrequency coupling for negative ion sources Models of radiofrequency coupling for negative ion sources a)," *Cit. Rev. Sci.*

Instruments, vol. 83, pp. 2–503, 2012.

[63] L. D. Landau, "On the vibrations of the electronic plasma," *Journal of Physics*, vol. X, no. 1. pp. 25–34, 1946.

[64] M. M. Turner, "Collisionless Electron Heating in an Inductively Coupled Discharge," *Phys. Rev. Lett.*, vol. 71, no. 12, pp. 1844–1847, 1993.

[65] E. A. Kralkina *et al.*, "RF power absorption by plasma of a low-pressure inductive discharge," *Plasma Sources Sci. Technol.*, vol. 25, no. 1, p. 15016, 2016.

[66] P. Chabert and N. Braithwaite, *Physics of Radio-Frequency Plasmas*. 2011.

[67] M. Cazzador, "Analytical and numerical models and first operations on the negative ion source NIO1," Università degli studi di padova, 2014.

[68] J.-S. J. Yoon *et al.*, "Cross Sections for Electron Collisions with Hydrogen Molecules," *J. Phys. Chem. Ref. Data*, vol. 37, no. 2, pp. 913–931, 2008.

[69] R. K. Janev, W. D. Langer, D. E. Post, and K. Evans, *Elementary Processes in Hydrogen-Helium Plasmas : Cross Sections and Reaction Rate Coefficients*. Springer Berlin Heidelberg, 1987.

[70] A. U. Rehman and Y. K. Pu, "Effect of boundary conditions on the classical skin depth and nonlocal behavior in inductively coupled plasmas," *Phys. Plasmas*, vol. 12, no. 9, pp. 1–2, 2005.

[71] P. Jain *et al.*, "Evaluation of power transfer efficiency for a high power inductively coupled radio-frequency hydrogen ion source," *Plasma Phys. Control. Fusion*, vol. 60 045007, 2018.

[72] P. Jain, M. Recchia, P. Veltri, M. Cavenago, A. Maistrello, and E. Gaio, "Improved methodology to estimate the power transfer efficiency in an inductively coupled radio frequency ion source," *IEEE Access*, 2018.

[73] E. Turkoz and M. Celik, "2D Axisymmetric Fluid and Electromagnetic Models for Inductively Coupled Plasma (ICP) in RF Ion Thrusters," in *33rd International Electric Propulsion Conference*, 2013, pp. 1–9.

[74] S. I. Babic and C. Akyel, "New analytic-numerical solutions for the mutual inductance of two coaxial circular coils with rectangular cross section in air," *IEEE Trans. Magn.*, vol. 42, no. 6, pp. 1661–1669, 2006.

[75] G. Chitarin and M. Guarnieri, "An Integral Formulation for Eddy Current Analyses in Axisymmetric Configurations," *IEEE Trans. Magn.*, vol. 25, no. 5, pp. 4330–4342, 1989.

[76] P. McNeely, S. V Dudin, S. Christ-Koch, U. Fantz, and the NNBI Team, "A Langmuir probe system for high power RF-driven negative ion sources on high potential," *Plasma Sources Sci. Technol.*, vol. 18, no. 1, p. 14011, 2009.

[77] P. McNeely and D. Wünderlich, "Neutral depletion in an H – source operated at high RF power and low input gas flow," *Plasma Sources Sci. Technol.*, vol. 20, no. 4, p. 45005, 2011.

[78] J. P. Boeuf, G. J. Hagelaar, P. Sarrailh, G. Fubiani, and N. Kohen, "Model of an inductively coupled negative ion source: II. Application to an ITER type source," *Plasma Sources Sci. Technol*, vol. 20, 2011.

[79] U. Fantz, L. Schiesko, and D. Wünderlich, "A comparison of hydrogen and deuterium plasmas in the IPP prototype ion source for fusion," *AIP Conf. Proc.*, vol. 1515, no. 2013, pp. 187–196, 2013.

[80] M. A. Lieberman and V. A. Godyak, "From Fermi acceleration to collisionless discharge heating," *IEEE Trans. Plasma Sci.*, vol. 26, no. 3, pp. 955–986, 1998.

[81] G. P. Canal, H. Luna, and R. M. O. Galvão, "Characterization of the transition from collisional to stochastic heating in a RF discharge," *J. Phys. D. Appl. Phys.*, vol. 43, no. 2, p. 25209, 2010.

[82] P. Jain, M. Recchia, M. Cavenago, U. Fantz, E. Gaio, and W. Kraus, "Evaluation of power transfer ef fi ciency for a high power inductively coupled radio- frequency hydrogen ion source," *Plasma Phys. Control. Fusion*, vol. 60, no. 45007, 2018.

[83] W. Kraus, U. Fantz, B. Heinemann, and P. Franzen, "Solid state generator for powerful radio frequency ion sources in neutral beam injection systems," *Fusion Eng. Des.*, vol. 91, pp. 16–20, 2015.

[84] M. Tuszewski, "Particle and heat transport in a low-frequency inductively coupled plasma," *Cit. Phys. Plasmas*, vol. 5, 1998.

[85] M. Tuszewski, "Enhanced Radio Frequency Field Penetration in an Inductively Coupled Plasma.," *Phys. Rev. Lett.*, vol. 77, no. 7, pp. 1286–1289, 1996.

[86] M. Cavenago *et al.*, "Status of NIO1 construction," *AIP Conf. Proc.*, vol. 1390, no. 1, pp. 640–649, 2011.

[87] P. Veltri *et al.*, "Langmuir probe characterization of the NIO1 ion source plasma," in *submission to 17th International Conference on Ion sources - AIP proceedings*, 2017.

[88] M. Cavenago *et al.*, "Construction of a versatile negative ion source and related developments," *AIP Conf. Proc.*, vol. 1515, no. 1, pp. 157–166, 2013.

[89] B. Heinemann *et al.*, "Towards large and powerful radio frequency driven negative ion sources for fusion," *New J. Phys.*, vol. 19, no. 1, pp. 0–23, 2017.

[90] A. Maistrello, "Characterization of the dielectric strength in vacuum of RF drivers for fusion neutral beam injectors," 2018.

[91] C. Y. Ho and T. K. Chu, "Electrical resistivity and thermal conductivity of nine selected AISI stainless steels - Center for Information and Numerical Data Analysis and Synthesis," *Distribution*, p. 15, 1977.

[92] B. Ritter, "Temperature vs Resistivity Vernier Format 2." [Online]. Available: http://hypertextbook.com/facts/2004/BridgetRitter.txt.

[93] "Attuazione delle direttive 89/618/Euratom, 90/641/Euratom, 92/3/Euratom e 96/29/Euratom in materia di radiazioni ionizzanti.," *DLgs 17 marzo 1995 n° 230*.

[94] C. Recommendation, "COUNCIL RECOMMENDATION of 12 July 1999 on the limitation of exposure of the general public to electromagnetic fields (0 Hz to 300 GHz)," *Off. J. Eur. communities*, pp. 59–70, 1999.

[95] "DLgs 81/08 CAPO IV - PROTEZIONE DEI LAVORATORI DAI RISCHI DI ESPOSIZIONE A CAMPI ELETTROMAGNETICI," vol. N° 7 artic, pp. 208–210.

[96] C. Dharma Raj, M. V. S. L. Ramyasree, and V. Sravan Kumar, "Analysis of wire mesh screen for shielding effectiveness in different frequency ranges," *2011 Int. Conf. Comput. Commun. Electr. Technol. ICCCET 2011*, pp. 198–203, 2011.

[97] G. A. Jackson, *Introduction to Electromagnetic Compatibility*, vol. 38, no. 7–8. 1992.

[98] K. F. Casey, "Electromagnetic Shielding Behavior of Wire-Mesh Screens," *IEEE Trans. Electromagn. Compat.*, vol. 30, no. 3, pp. 298–306, 1988.

[99] D. Dainese, "CAMPI ELETTROMAGNETICI IMPIANTO HVRFTF - Internal report," 2016.

[100] N. Safety Test Solutions, "Electric and Magnetic Field Measurement NBM Series Probes." [Online]. Available: http://www.narda-sts.us/pdf_files/8700SeriesProbes.pdf.

[101] N. Safety Test Solutions, "Model 8718 RF Radiation Survey Meter." [Online]. Available: http://www.narda-sts.us/pdf_files/8718_RFRadSurvMeter.pdf.

APPENDIX

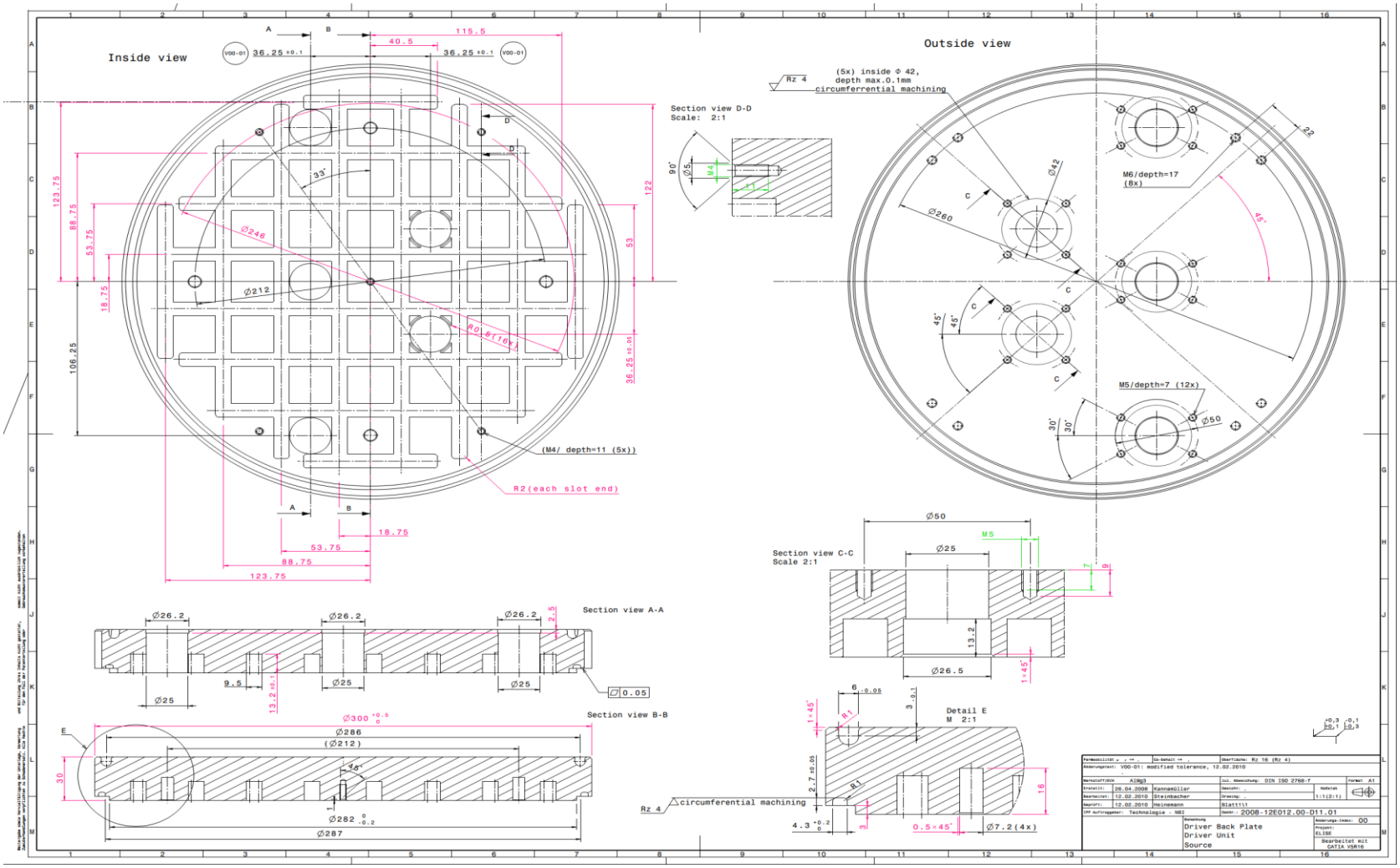
Inside view
Outside view
Section view D-D
Scale: 2:1
Section view C-C
Scale 2:1
Section view A-A
Section view B-B
Detail E
M 2:1
(5x) inside Φ 42,
depth max.0.1mm
circumferrential machining
Rz 4
M6/depth=17
(8x)
M5/depth=7 (12x)
(M4/ depth=11 (5x))
R2(each slot end)
Driver Back Plate
Driver Unit
Source
2008-12E012.00-D11.01

APPENDIX

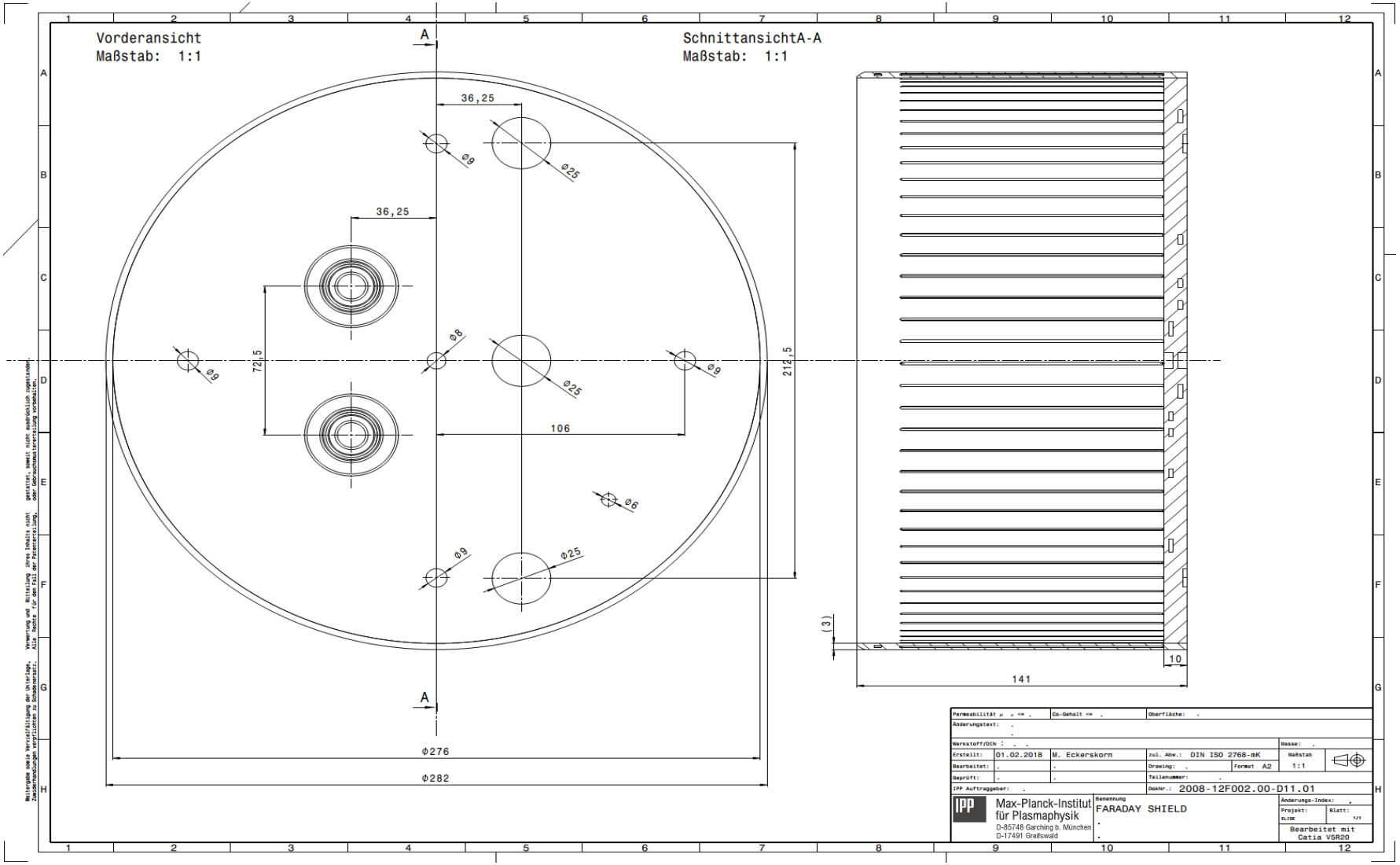
Vorderansicht
Maßstab: 1:1
SchnittansichtA-A
Maßstab: 1:1
36,25
36,25
Ø9
Ø25
Ø8
Ø6
72,5
212,5
106
(3)
10
141
Ø276
Ø282
Max-Planck-Institut für Plasmaphysik
D-85748 Garching b. München
D-17491 Greifswald
FARADAY SHIELD
2008-12F002.00-D11.01
Bearbeitet mit Catia V5R20

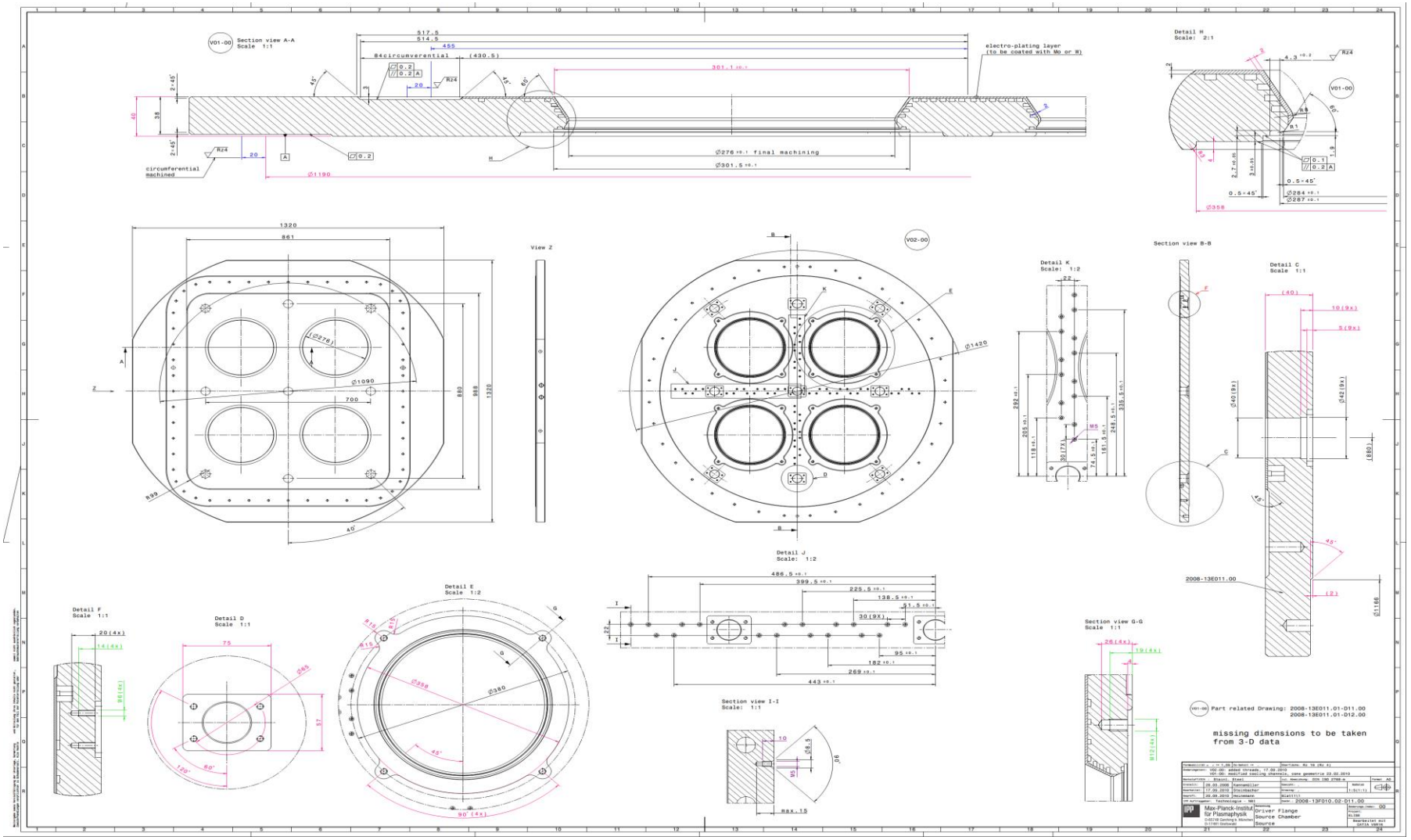
V01-00 Section view A-A
Scale 1:1
517.5
514.5
455
84circumverential (430.5)
electro-plating layer
(to be coated with Mo or W)
Ø276 +0.1 final machining
Ø301.5 +0.1
Ø1190
circumferential machined
Detail H
Scale: 2:1
Ø264 +0.1
Ø227 +0.1
Ø358
1320
861
View Z
Ø1090
700
V02-00
Ø1420
Detail K
Scale: 1:2
Section view B-B
Detail C
Scale 1:1
Detail J
Scale: 1:2
Detail F
Scale 1:1
Detail D
Scale 1:1
Detail E
Scale 1:2
Ø358
Ø380
Section view I-I
Scale: 1:1
Section view G-G
Scale 1:1
2008-13E011.00
V01-00 Part related Drawing: 2008-13E011.01-D11.00
2008-13E011.01-D12.00
missing dimensions to be taken
from 3-D data
Max-Planck-Institut
für Plasmaphysik
Driver Flange
Source Chamber
Source
2008-13F010.02-D11.00

APPENDIX

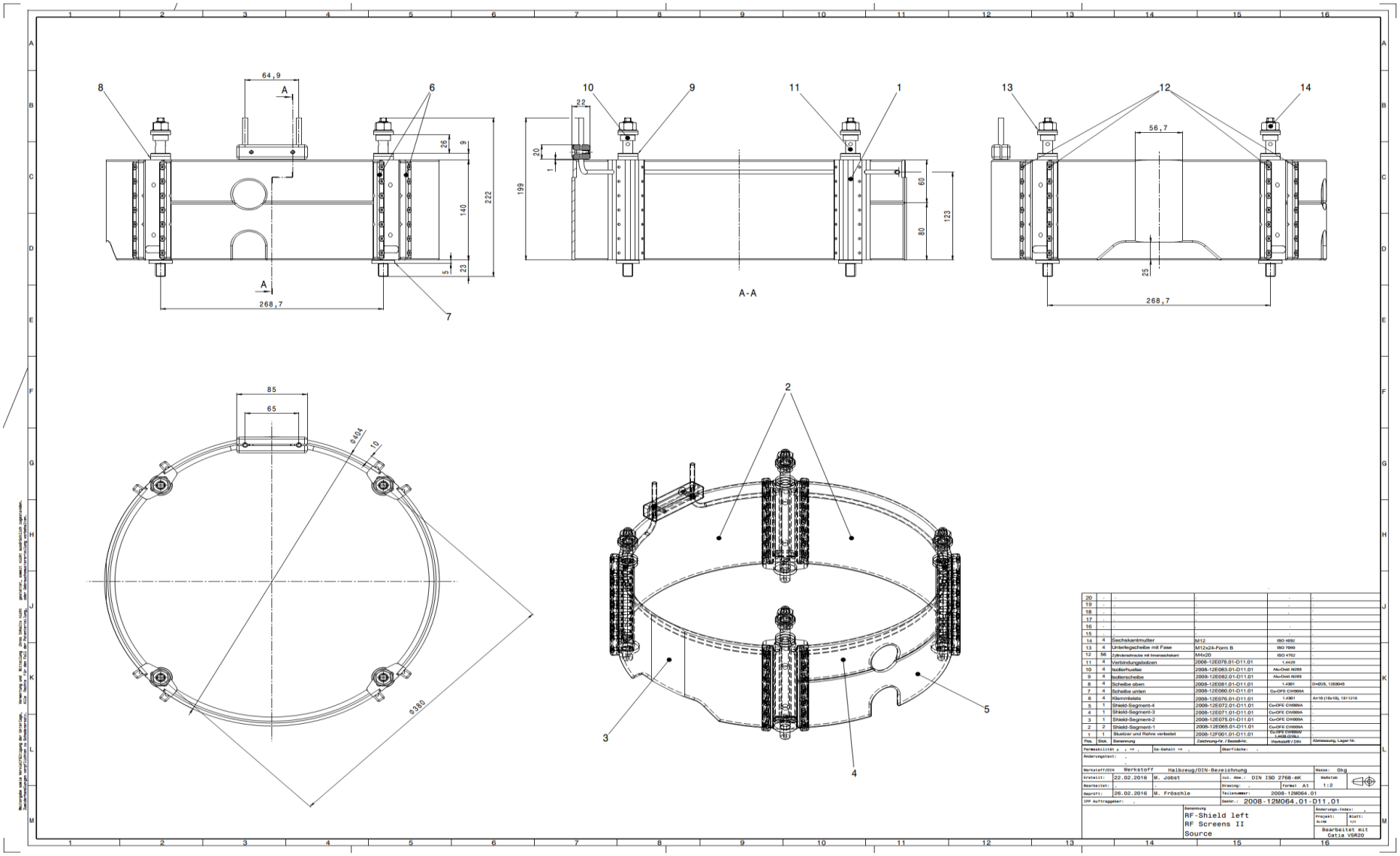

Pos.	Stck.	Benennung	Zeichnung-Nr. / Bestell-Nr.	Werkstoff / DIN	Abmessung, Lager Nr.
20					
19					
18					
17					
16					
15					
14	4	Sechskantmutter	M12	ISO 4032	
13	4	Unterlegscheibe mit Fase	M12x24-Form B	ISO 7090	
12	56	Zylinderschraube mit Innensechskant	M4x20	ISO 4762	
11	4	Verbindungsbolzen	2008-12E078.01-D11.01	1.4429	
10	4	Isolierhuelse	2008-12E083.01-D11.01	Alu-Oxid Al203	
9	4	Isolierscheibe	2008-12E082.01-D11.01	Alu-Oxid Al203	
8	4	Scheibe oben	2003-12E081.01-D11.01	1.4301	DHD25, 1203045
7	4	Scheibe unten	2008-12E080.01-D11.01	Cu-OFE CW009A	
6	4	Klemmkeilstz	2008-12E076.01-D11.01	1.4301	An10 (10x10), 1311216
5	1	Shield-Segment-4	2008-12E072.01-D11.01	Cu-OFE CW009A	
4	1	Shield-Segment-3	2008-12E071.01-D11.01	Cu-OFE CW009A	
3	1	Shield-Segment-2	2008-12E075.01-D11.01	Cu-OFE CW009A	
2	2	Shield-Segment-1	2008-12E065.01-D11.01	Cu-OFE CW009A	
1	1	Stutzer und Rohre verbeitet	2008-12F001.01-D11.01	Cu-OFE CW009A 1.4435 (316L)	

Formabzüge ø ... >= ... | Oa-Gehalt >= ... | Oberfläche: ...
Änderungstext: ...

Herkunft/DIN	Werkstoff	Halbzeug/DIN-Bezeichnung		Masse:	Okg
Erstellt:	22.02.2016	M. Jobst	zul. Abw.: DIN ISO 2768-mK	Maßstab	
Bearbeitet:			Drawing:	Format A1	1:2
Geprüft:	26.02.2016	M. Fröschle	Teilenummer:	2008-12M064.01	
IPP Auftraggeber:			Sachr.:	2008-12M064.01-D11.01	

Benennung
RF-Shield left
RF Screens II
Source

Änderungs-Index:
Projekt: ESS
Blatt: 1/1

Bearbeitet mit Catia V5R20